

ANALYSIS
OF A
THREE-DIMENSIONAL CORNER FLOW
WITH ONE ROUGH SURFACE

James Roche, Arnold Fontaine and Steve Deutsch

October 2000

Applied Research Laboratory
PO Box 30
State College, PA 16804

DTIC QUALITY INSPECTED 4

DTIC QUALITY INSPECTED 4

20001018 004

REPORT DOCUMENTATION PAGE			Form Approved OMB No. 0704-0188	
Public reporting burden for this collection of information is estimated to average 1 hour per response, including the time for reviewing instructions, searching existing data sources, gathering and maintaining the data needed, and completing and reviewing the collection of information. Send comments regarding this burden estimate or any other aspect of this collection of information, including suggestions for reducing this burden, to Washington Headquarters Services, Directorate for Information Operations and Reports, 1215 Jefferson Davis Highway, Suite 1204, Arlington, VA 22202-4302, and to the Office of Management and Budget, Paperwork Reduction Project (0704-0188), Washington, DC 20503.				
1. AGENCY USE ONLY (Leave Blank)	2. REPORT DATE October, 2000	3. REPORT TYPE AND DATES COVERED Final; 15 June 1996 through 31 December 1999		
4. TITLE AND SUBTITLE Modeling 3-D Flows Over Rough Surfaces		5. FUNDING NUMBERS G; N00014-96-1-1034		
6. AUTHORS Steven Deutsch				
7. PERFORMING ORGANIZATION NAME(S) AND ADDRESS(ES) Applied Research Laboratory The Pennsylvania State University PO Box 30 State College, PA 16804		8. PERFORMING ORGANIZATION REPORT NUMBER		
9. SPONSORING / MONITORING AGENCY NAME(S) AND ADDRESS(ES) Patrick Purtell, ONR 333 Office of Naval Research Ballston Centre Tower One, 800 North Quincy Street Arlington, VA 22217-5660		10. SPONSORING / MONITORING AGENCY REPORT NUMBER		
11. SUPPLEMENTARY NOTES				
12a. DISTRIBUTION / AVAILABILITY STATEMENT approved for public release		12b. DISTRIBUTION CODE		
13. ABSTRACT (Maximum 200 words) Two and three-dimensional coincident velocity measurements were obtained in a turbulent corner flow at zero axial pressure gradient. Ten thousand coincident velocity ensembles were collected at each measurement location using a three component LDV system in the side-scatter mode. Measurements were made for two corner configurations; two hydrodynamically smooth surfaces, and one smooth and one fully rough surface ($k^+=90$). For the smooth-smooth configuration, centerline results compare favorably with classical flat plate data. Secondary flow structures associated with flow along the corner produced modification to the measured Reynolds stresses and triple correlations for the smooth-smooth condition. For the corner flow with one rough surface, the plots of the secondary velocity vectors suggest that the presence of the roughness has disrupted the flow structure.				
14. SUBJECT TERMS three component LDV system coincident velocity measurements			15. NUMBER OF PAGES	
			16. PRICE CODE	
17. SECURITY CLASSIFICATION OF REPORT Unclassified	18. SECURITY CLASSIFICATION OF THIS PAGE Unclassified	19. SECURITY CLASSIFICATION OF ABSTRACT SAR	20. LIMITATION OF ABSTRACT SAR	

Abstract

Two and three-dimensional coincident velocity measurements were obtained in a turbulent corner flow with zero pressure gradient. Ten thousand coincident velocity ensembles were collected at each measurement location using a three component LDV system in the side-scatter mode. Centerline results for the smooth flat plate compared favorably with classical flat plate data. The flat plate was replaced with a rough surface, $k^+ \approx 90$. Secondary flow structures associated with flow along the corner produced modification to the measured Reynolds stresses and triple correlations for the smooth test surface. On the rough surface, the plots of the secondary velocity vectors suggest that the presence of the roughness has disrupted the flow structure.

Table of Contents

Abstract	1
Table of Contents	2
List of Tables	3
List of Figures	4
Nomenclature	9
Literature review	12
Experimental apparatus and instrumentation	43
Data reduction	74
Results	84
Conclusions	123
Bibliography	124

LIST OF TABLES

Table No.	Title	Page No.
2.1	Typical experimental conditions.	47
2.2	LDV optical specifications.	69
2.3	Boundary layer hot wire characteristics.	72
3.1	Comparison of the methods for calculating the friction velocity along the centerline of the smooth test surface.	77
3.2	Comparison of the displacement and momentum thicknesses and shape factors using measured data and flat plate theory for the smooth test surface.	83
3.3	Comparison of the displacement and momentum thicknesses and shape factors using measured data and flat plate theory for the rough test surface.	83
4.1	Experiment test matrix.	84
4.2	Maximum axial turbulence intensity and corresponding y^+ locations.	91

LIST OF TABLES

Table No.	Title	Page No.
2.1	Typical experimental conditions.	47
2.2	LDV optical specifications.	69
2.3	Boundary layer hot wire characteristics.	72
3.1	Comparison of the methods for calculating the friction velocity along the centerline of the smooth test surface.	77
3.2	Comparison of the displacement and momentum thicknesses and shape factors using measured data and flat plate theory for the smooth test surface.	83
3.3	Comparison of the displacement and momentum thicknesses and shape factors using measured data and flat plate theory for the rough test surface.	83
4.1	Experiment test matrix.	84
4.2	Maximum axial turbulence intensity and corresponding y^+ locations.	91

LIST OF FIGURES

Figure No.	Title	Page No.
1.1	The particle image visualization images from Doligalski, Smith and Walker (1994). A, b, c, and d illustrate the development of the horseshoe vortex in the junction region of a rectangular body. Flow is from left to right with the body just to the right of the field of view. The sequences are 0.25 seconds apart. HV is the horseshoe vortex and SV is the secondary vortex.	17
1.2	The primary velocity contour from Shabaka (1979). Distance downstream from the leading edge of the appendage is 187.1 mm.	18
1.3	The primary velocity contour from Shabaka (1979) further downstream at 644.3 mm.	19
1.4	The secondary flow pattern from Shabaka (1979).	21
1.5	The surface pressure and secondary flow field for a variable thickness appendage from Devenport and Simpson (1992). In a, the contours of the mean surface pressure coefficient on the wall surrounding the appendage are shown. The numbers 1, 3, 4, 5, 8 and 10 on the right side indicate LDV measurement locations. In b, the mean secondary flow field generated by the vortex is shown. From top to bottom are the LDV measurement planes represented by 1, 3, 4, 5, 8 and 10 in a.	22
1.6	Comparison of u_{rms}/U_{ref} contours at $X/C = 0.75$ from Fleming, Simpson, Cowling and Devenport (1993) for θ/t (a) 0.1014, (b) 0.1003, (c) 0.0548, respectively.	25
1.7	Comparison of U/U_{ref} contours and secondary velocity vectors at $X/C = 0.75$ from Fleming, Simpson, Cowling and Devenport (1993) for θ/t (a) 0.1014, (b) 0.1003, (c) 0.0548, respectively.	27
1.8	The primary flow velocity contours, U/U_s , for square ducts from Fujita, Yokosawa, and Hirota (1989): left side, smooth duct; right side, duct with one rough surface indicated by dashed line; U_s is the	29

	maximum primary flow velocity.	
1.9	Secondary flow pattern for square ducts from Fujita, Yokosawa, and Hirota (1989): left side, smooth duct; right side, duct with one rough surface indicated by dashed line; U_s is the maximum primary flow velocity.	30
1.10	Control volume for flow over a rough surface from Taylor, Coleman and Hodge (1985).	35
1.11	Mean velocity profiles from Bandyopadhyay and Watson (1988): the open circles represent smooth surface, the open triangles, d-type walls, and filled squares, k-type walls.	37
1.12	Ratio of Reynolds stress to turbulent kinetic energy from Bandyopadhyay and Watson (1988): the solid line, smooth surface at $Re_\theta = 8000$, others as in Figure 1.11.	39
1.13	Axial third moment and wall-normal third moment from Bandyopadhyay and Watson (1988): the solid line, smooth surface at $Re_\theta = 4750$, broken line, sand grain at $Re_\theta = 1.7 \times 10^5$.	40
2.1	Schematic of wind tunnel facility.	44
2.2	Illustration of the rough surface manufactured by 3M Corporation.	46
2.3	Dual beam mode of heterodyne detection in LDV from Adrian (1983).	49
2.4	Properties of a focused Gaussian beam from Adrian (1983).	51
2.5	Geometry of the nominal LDV measurement or probe volume from Adrian (1983).	53
2.6	Typical LDV signals produced by various partial trajectories decomposed into pedestal plus Doppler bursts from Adrian (1983).	58
2.7	Particle size distribution of a propylene glycol aerosol from TSI Inc.	60
2.8	Schematic of constant temperature anemometer system from Fingerson (1983).	63
2.9	A Model 1218 boundary layer probe by TSI Inc.	65
2.10	Three-component LDV system in dual beam mode with green and violet beam pairs in back scatter mode and blue beam pair in side	68

	scatter mode.	
2.11	Calibration curve of the mean velocity versus voltage for the boundary layer hot wire probe.	72
3.1	The axial turbulence intensity at $X = 1.02$ m comparing the measured data and velocity bias corrected data.	76
3.2	Virtual origin as a function of axial location $X^{6/7}$ for the smooth test surface.	81
3.3	Virtual origin as a function of axial location $X^{6/7}$ for the rough test surface.	82
4.1	Comparison of the axial turbulence intensity measured with the LDV and hot wire probes along the centerline of the smooth test surface at $X = 0.66$ m.	85
4.2	Mean axial velocity profiles in inner variables along the centerline of the smooth test surface.	87
4.3	A comparison of the mean axial velocity profiles along the centerline of the smooth test surface.	88
4.4	Comparison of the velocity defect along the centerline of the smooth test surface.	89
4.5	The axial turbulence intensity in inner variables along the centerline of the smooth test surface.	90
4.6	The axial turbulence intensity in outer variables along the centerline of the smooth test surface.	92
4.7	The $-\overline{uv}$ Reynolds shear stress in inner variables along the smooth test surface centerline.	93
4.8	The $-\overline{uv}$ Reynolds shear stress along the centerline of the test surface.	95
4.9	Mean axial velocity for the smooth test surface ranging into the corner at $X = 0.66$ m.	97
4.10	Mean axial velocity for the smooth test surface ranging into the corner at $X = 1.02$ m.	98
4.11	Axial turbulence intensity for the smooth test surface ranging into the	100

	corner at $X = 0.66$ m.	
4.12	Axial turbulence intensity for the smooth test surface ranging into the corner at $X = 1.02$ m.	101
4.13	The $-\overline{uv}$ Reynolds shear stress for the smooth test surface ranging into the corner at $X = 0.66$ m.	102
4.14	The $-\overline{uv}$ Reynolds shear stress for the smooth test surface ranging into the corner at $X = 1.02$ m.	103
4.15	Comparison of the mean axial velocity in inner variables for the smooth and rough test surfaces at $X = 1.02$ m and $Z = 102$ mm.	105
4.16	Mean axial velocity profiles for the smooth and rough test surfaces at $X = 1.02$ m and $Z = 102$ mm.	106
4.17	Mean axial velocity profiles plotted as a velocity defect for the smooth and rough test surfaces at $X = 1.02$ m and $Z = 102$ mm.	108
4.18	The axial turbulence intensity for the smooth and rough test surfaces at $X = 1.02$ m and $Z = 102$ mm.	109
4.19	The $-\overline{uv}$ Reynolds shear stress for the smooth and rough test surfaces at $X = 1.02$ m and $Z = 102$ mm.	110
4.20	The mean axial velocity for the rough test surface ranging into the corner at $X = 0.66$ m.	112
4.21	The mean axial velocity for the rough test surface ranging into the corner at $X = 1.02$ m.	113
4.22	The primary velocity contours for the rough test surface ranging into the corner at $X = 0.66$ m.	115
4.23	The secondary velocity vectors for the rough test surface ranging into the corner at $X = 0.66$ m.	116
4.24	The secondary velocity vectors for the rough test surface from $Z = 0.03$ m ranging into the corner at $X = 0.66$ m.	117
4.25	The axial turbulence intensity for the rough test surface ranging into the corner at $X = 0.66$ m.	118
4.26	The axial turbulence intensity for the rough test surface ranging into	119

the corner at $X = 1.02$ m.

4.27 The $-\overline{uv}$ Reynolds shear stress for the rough test surface ranging into the corner at $X = 0.66$ m. 121

4.28 The $-\overline{uv}$ Reynolds shear stress for the rough test surface ranging into the corner at $X = 1.02$ m. 122

NOMENCLATURE

a	The speed of sound.
a_1	The ratio of the Reynolds shear stress to the turbulent kinetic energy.
A_1	The influence of the laser and photodetector on the SNR.
A_2	The influence of the various optical properties on the SNR.
A_3	The influence of the properties of the particle.
b	Duct width.
c	The chord of the variable thickness test surface.
C	Roughness constant.
C_o	The logarithmic law velocity constant for a smooth wall.
C_1	Represents the wall shear stress and blockage factor.
C_2	Represents the form drag of a roughness element.
C_3	Represents the dynamic pressure on a roughness element.
C_f	Coefficient of friction.
d	Fluid dynamic height origin on associated with a rough surface.
d	The laser beam spacing.
D_a	The diameter of the light collecting aperture.
$d_{e^{-1}}$	The focal waist of the laser beam.
$D_{e^{-1}}$	The laser beam waist.
d_f	The fringe spacing.
d_m	The maximum diameter of a probe volume.
d_p	Seeding particle diameter.
E_1	A scattered light wave.
E_2	A scattered light wave.
E_{o1}	A light beam.
E_{o2}	A light beam.
f	The lens focal length.
f_c	The collecting lens focal length.
f_d	The measured Doppler frequency.
f	Frequency of a laser beam.
f^*	Doppler shifted frequency.
G	The integral parameter involving Clauser's defect thickness.
\overline{G}	The average light scatter gain.
h	Planck's constant.
H	The shape factor.
I	The total light intensity.
k	The average roughness element height.
k_s	Equivalent sand grain roughness height.
k^+	Dimensionless roughness based Reynolds number using k , the friction velocity and viscosity.
LOLS	Line of low shear.
l_m	The maximum length of a probe volume.
MDF	The momentum deficit factor.
N_{FR}	The number of fringes in a probe volume.

P_o	The power of either laser beam in a balanced dual beam LDV system.
R_r	The ratio of the apparent shear stress due to the form drag of the roughness elements and the total apparent wall shear stress.
Re	The Reynolds number based on axial location.
Re_t	The Reynolds number based on the test surface thickness.
Re_{x_0}	The Reynolds number based on the virtual origin.
Re_δ	The Reynolds number based on the boundary layer thickness.
Re_{δ^*}	The Reynolds number based on the displacement thickness.
Re_θ	The Reynolds number based on the momentum thickness.
SNR	The signal to noise ratio.
s_o	The distance between the lens and the location where the laser beam waist is measured.
s_1	The location of the focal length of a lens.
sku	Skewness of the u velocity component.
skv	Skewness of the v velocity component.
U_{fs}	The free stream axial velocity.
U_{max}	The maximum velocity.
U_s	The centerline velocity in a channel.
U_{ref}	The free stream axial velocity.
$U_{rms}, V_{rms}, W_{rms}$	The root mean square of the velocity.
U, V, W	The mean velocities associated with X, Y, Z, respectively.
u, v, w	The fluctuating velocity component associated with X, Y, Z, respectively.
u, v, w	The instantaneous velocities associated with X, Y, Z, respectively.
u_τ	The friction velocity.
u^+	The local velocity normalized by the free stream velocity.
\bar{V}	Doppler signal visibility.
W	Wake function associated with Cole's equation.
X, Y, Z	The orthogonal coordinate system.
X_{v_0}	The virtual origin.
y^+	The y location normalized by the friction velocity and viscosity.
β	The angle between the old axis and the orthogonal axis, used in coordinate transformation.
ε	The dissipation rate.
ε_o	The Coulomb force constant.
$\varepsilon_1, \varepsilon_2$	Plane light waves.
η_q	Quantum efficiency of the photomultiplier.
δ	The boundary layer thickness.
δ^*	The displacement thickness.
κ	Von Karmen constant.
λ	The wavelength of a laser beam.
ν	Viscosity.
ν_o	Frequency of laser light.
θ	The momentum thickness.
ζ	The displaced roughness height.

τ	The burst or residence transit time.
τ_r	The apparent shear stress due to the form drag of the roughness elements.
τ_T	The total apparent shear stress.
ω	The vorticity.
ω_1, ω_2	Frequency of a light wave.
ΔF	Post-photomultiplier bandwidth.
$\left[\frac{\Delta U}{u_\tau} \right]$	The roughness function.

Chapter 1

Literature Review

1.1. Introduction

At high speeds, transport aircraft or undersea vehicles, for example, have roughness Reynolds numbers on the order of 100. Modern computer codes use empirical correlations to correct for this roughness effect, but the correlations employed were gathered in two-dimensional or axisymmetric flow fields. For a transport aircraft in maneuvers then, one is forced to use two-dimensional correlations for a three-dimensional flow. One cannot even reliably assess the magnitude of the resulting problem without recourse to accurate measurements of a three-dimensional flow over a rough surface and a comparison of this data with existing codes. The geometrically simplest three-dimensional potential flow field and the one addressed in the current work is the flow in a corner with one rough wall.

1.2. Overview

Extensive reviews of three-dimensional flow in corners have been given by Bradshaw (1987), Doligalski, Smith, and Walker (1994) and Johnston and Flack (1996). The flow was first categorized by Prandtl in 1927. He postulated the existence of secondary vortices in such flows. The generation mechanism for the secondary motion was either skew or stress induced. A skew induced secondary flow occurs along the junction of a flat plate and an attached surface and is called the first kind of secondary flow. The second kind occurs in the corner of a channel. Nikuradse (1930) verified the

existence of the secondary vortices in the flow. These occurred in the form of **streamwise helical vortices** in the corner region.

An alternate but related classification of the secondary motion was given by Pierce (1968). They describe the three-dimensional boundary layer flows as either pressure-driven or shear-driven, according to the principal mechanism driving the secondary flow. Pressure-driven flows are typically characterized by free stream streamlines that curve with attendant transverse pressure gradients and correspond to Prandtl's first kind of secondary flow. Shear-driven flows occur when the shearing motion of adjacent fluid layers provide the principal driving force for the secondary boundary layer flow. An example is a flow along the end wall and a rotating turbine blade.

Looking at the vorticity equation for the three-dimensional flow provides a clearer understanding of the secondary motion. The mean and fluctuating velocity components in the X, Y and Z directions are U, V, W and u, v, and w, respectively. Assuming the flow is incompressible, the axial vorticity is,

$$\begin{aligned}
 \frac{D\omega_x}{Dt} = & \omega_x \frac{\partial U}{\partial x} + \omega_y \frac{\partial V}{\partial y} + \omega_z \frac{\partial W}{\partial z} & \text{Term 1} \\
 & + v \left[\frac{\partial^2 \omega_x}{\partial y^2} + \frac{\partial^2 \omega_x}{\partial z^2} \right] & \text{Term 2} \\
 & - \left[\frac{\partial^2}{\partial y^2} - \frac{\partial^2}{\partial z^2} \right] \overline{vw} & \text{Term 3} \\
 & - \frac{\partial^2}{\partial y \partial z} \left[\overline{w^2} - \overline{v^2} \right] & \text{Term 4} \\
 & + \frac{\partial^2}{\partial x \partial z} \left[\overline{uv} \right] - \frac{\partial^2}{\partial x \partial y} \left[\overline{uw} \right] & \text{Term 5}
 \end{aligned} \tag{1.1}$$

Term 1 on the right hand side produces vortex stretching, and describes the pressure-driven flow or Prandtl's first kind of secondary motion while term 2 represents viscous diffusion. Terms 3 and 4 involving \overline{vw} , $\overline{v^2}$ and $\overline{w^2}$ maintain Prandtl's second kind of secondary motion. Term 5 completes the Reynolds shear stress terms.

Adding one rough wall further complicates the corner flow field. Research summaries on surface roughness are given by White (1974), Schlichting (1987), Raupach, Antonia, and Rajagopalan (1991), and Krogstad, Antonia, and Browne (1992). Using the friction velocity, kinematic viscosity and roughness element height, Nikuradse (1933) classified flow as dynamically smooth, transitional and fully rough. White (1974) proposed that the three flow regimes for flow over rough plates and rough walled pipes be based on the uniformly distributed roughness results found in Clauser (1956). He defined k^+ as the dimensionless length scale using the average roughness element height, k , the friction velocity and kinematic viscosity. The smooth regime exists for $0 < k^+ < 4$, the transitional regime exists for $4 < k^+ < 60$ and the fully rough regime for $60 < k^+$.

For a flow over a rough surface, the modified logarithmic law emphasizes the departure of a rough wall flow from that over a smooth wall flow. The law from Raupach et al. is,

$$\frac{U(\zeta)}{u_\tau} = \frac{1}{\kappa} \ln \left(\frac{\zeta u_\tau}{\nu} \right) + C_o - \left[\frac{\Delta U}{u_\tau} \right] \quad (1.2)$$

where ζ is the displaced height, $\zeta = Y - d$, and d is the fluid dynamic height origin, Y^+ is the displaced height normalized by the viscous length scale, κ is the von Karmen

constant, C_o is the constant for a smooth wall and $\left[\frac{\Delta U}{u_\tau} \right]$ is a roughness function. In the

summary by Raupach, Antonia, and Rajagopalan (1991), the fluid dynamic height origin is approximated as $0.64k \sim 0.8k$. The roughness function depends on the dimensions and density of the roughness elements and increases with increasing wall roughness height.

1.3. Skew induced secondary flow

In Skew induced secondary flow, the turbulent boundary layer approaching the leading edge of the flat plate or test surface separates and a horseshoe vortex develops in the junction. The vortex wraps around the test surface and trails downstream. An adverse pressure gradient in the junction causes the streamlines to skew. The legs of the horseshoe vortex create the secondary flow. Typical test surface geometries studied have a constant thickness, t , or a variable thickness.

1.3.1. Constant thickness surface

With a constant thickness test surface, studies of the skew induced secondary flow concentrate on the effects of the leading edge geometry and junction flow conditions. Researchers examine the flow field in the junction and in the downstream Y-Z plane normal to the free stream velocity. The approaching boundary layer and the test surface leading edge geometry affect the horseshoe vortex strength and the downstream location of the vortex core that developed in the flat plate – test surface junction. No comparison based on the variation of test surface geometry or experimental conditions using existing published research can be made. Either the surface geometry and/or experimental conditions or both are varied and thus cannot be compared. In each paper, the horseshoe vortex forms in the junction and trails downstream with its center remaining closest to the

flat plate. The vortex is strongest in the junction and weakens as it trails downstream. For a skew induced secondary flow, term 1 on the right hand side in the axial vorticity equation, (eqn. 1.1), generates the secondary flow.

Based on the results of previous researchers, the secondary flow transports turbulence and modifies the mean flow in the corner boundary layer for the interval $400 < Re_\theta < 2400$, thus having a large effect on the distribution of turbulent stresses. The dominant structure is the streamwise vortex, which affects the velocity and Reynolds stress profiles in the outer region of the boundary layer. The vortex has a small effect on the local equilibrium of the inner layer except near the leading edge. There, the vortex is strong.

Within the junction of the flat plate and test surface, the approaching turbulent boundary layer in Kubendran (1983) separates and forms a horseshoe vortex. In Figure 1.1 from Doligalski, Smith and Walker (1994), a horseshoe vortex and secondary vortex are visible in the junction just upstream of a test surface, with a rectangular leading edge, for a momentum thickness based Reynolds number, $Re_\theta = 700$. In Figure 1.1a, a large horseshoe vortex forms and dominates the region. It induces the generation of secondary vortices that grow and are subsequently ejected from the surface. The ejection appears as a strong, narrow band eruption of surface fluid and the horseshoe vortex moves temporally due to the interaction with the secondary vortex. With time, the secondary vortex begins to be compressed, followed by a sudden, further compression and ejection from the surface. A weaker secondary vortex reappears away from the surface.

For an elliptical leading edge, primary velocity contours are shown in Figures 1.2 and 1.3 at distances of 187.1 mm and 644 mm downstream of the leading edge, with Re_θ

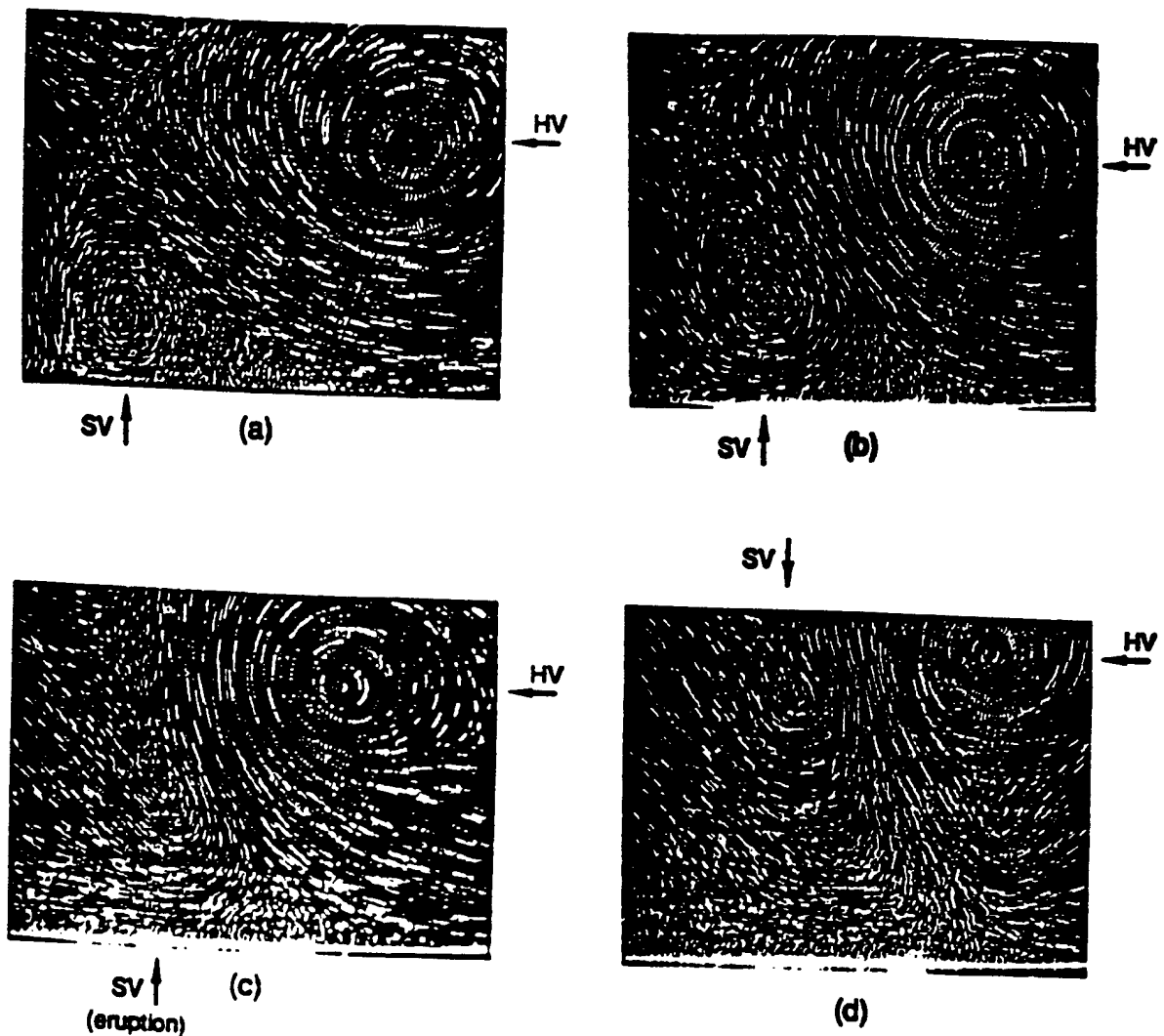


Figure 1.1 The particle image visualization images from Doligalski, Smith and Walker (1994). A, b, c, and d illustrate the development of the horseshoe vortex in the junction region of a rectangular body. Flow is from left to right with the body just to the right of the field of view. The sequences are 0.25 seconds apart. HV is the horseshoe vortex and SV is the secondary vortex.

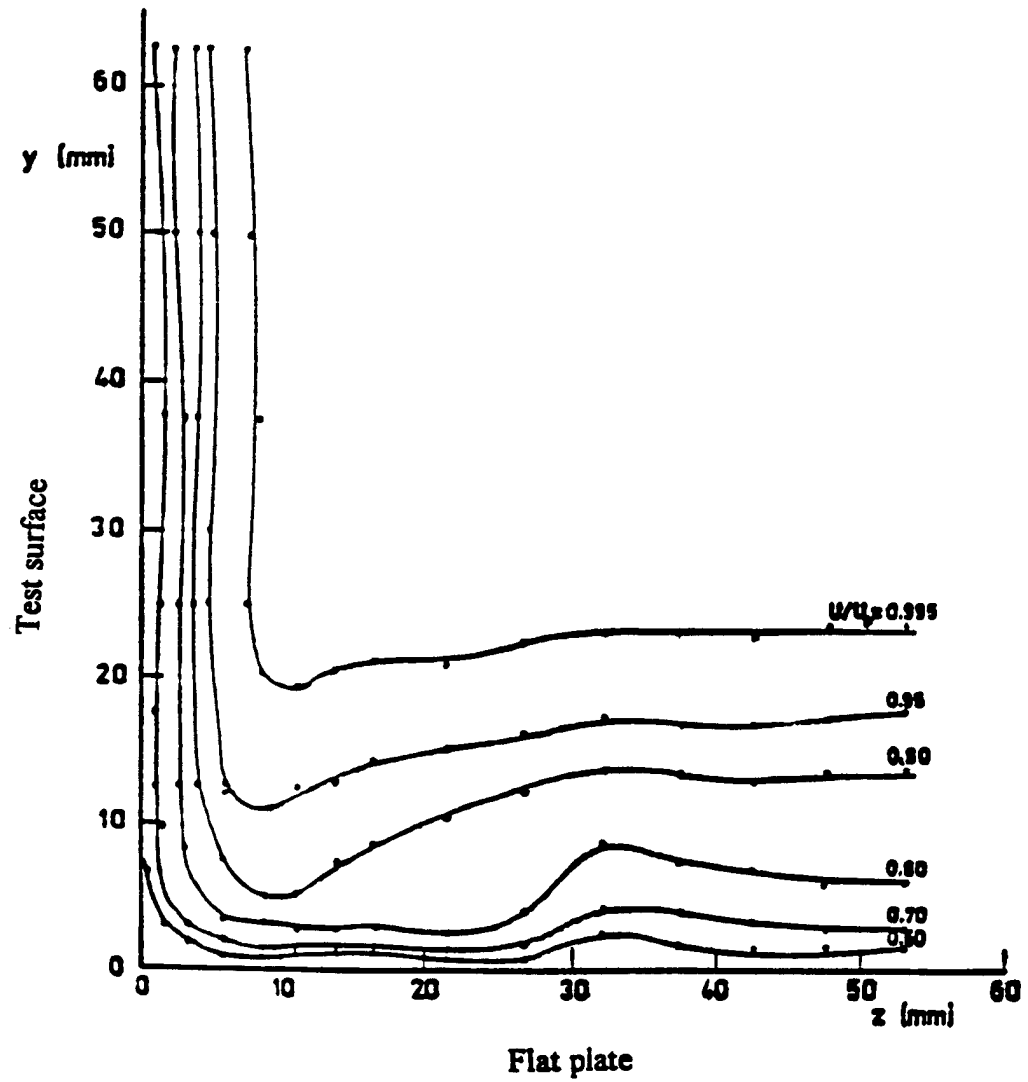


Figure 1.2 The primary velocity contour from Shabaka (1979). Distance downstream from the leading edge of the appendage is 187.1 mm.

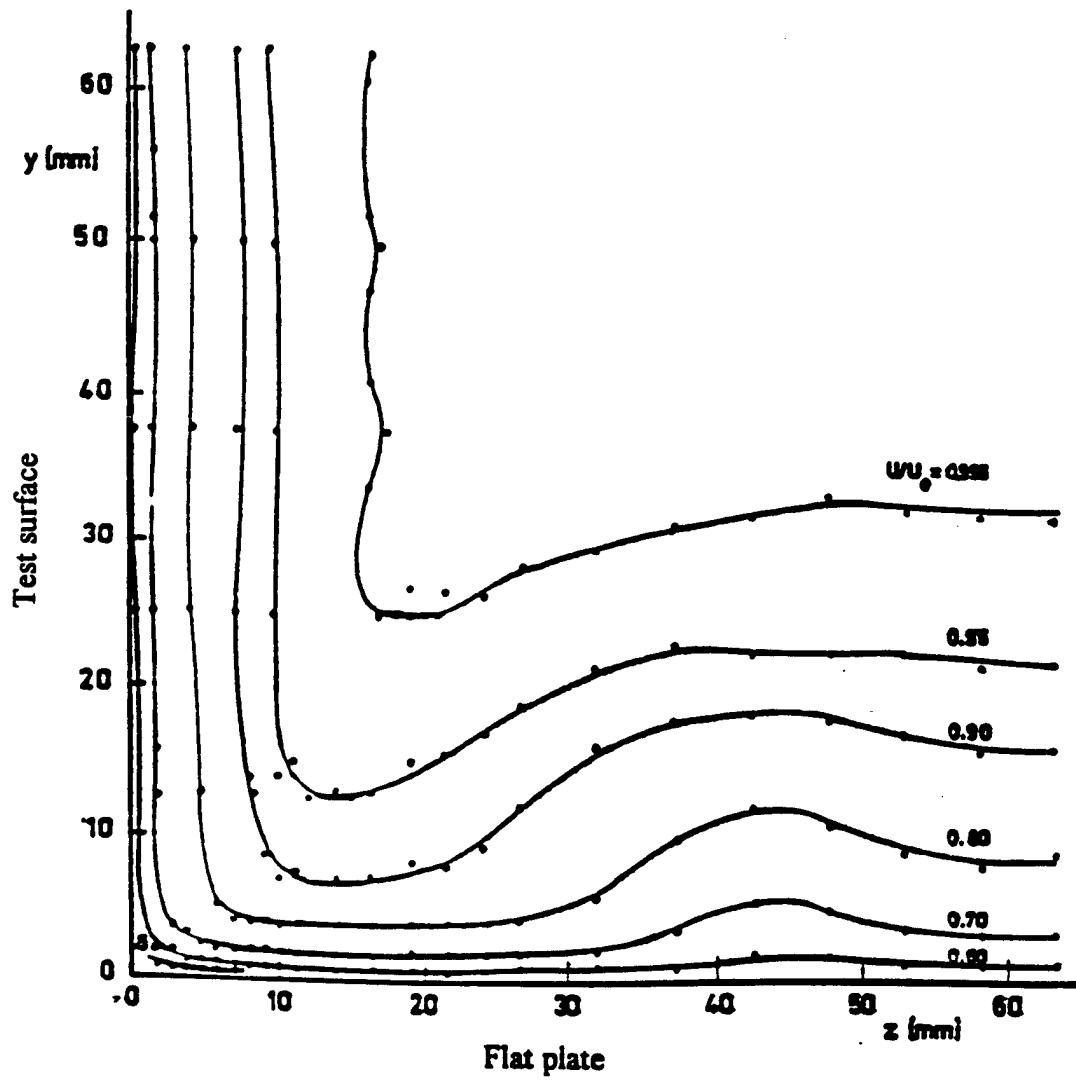


Figure 1.3 The primary velocity contour from Shabaka (1979) further downstream at 644.3 mm.

corresponding to 400 and 1320, respectively. The flow over the test surface is tripped turbulent. The contours along the test surface are constant relative to the Y direction while those along the flat plate are disrupted by the vortex. As the downstream distance from the leading edge increases, the vortex diffuses and its core moves away from the corner. Similar results are presented in contour plots by McMahon, Hubbart and Kubendran (1982) at a lower test surface thickness based Reynolds number, Re_t .

Figure 1.4 shows the typical secondary flow pattern from Shabaka (1979) in the Y-Z plane. At $X = 615$ mm downstream from the leading edge and $Re_0 = 1320$, a vortex has its center at approximately $Y = 17$ and $Z = 22$ mm. As the vortex weakens and moves downstream from the test surface leading edge, a second vortex may appear between the flat plate and the original vortex.

1.3.2. Variable thickness surface

Although not studied in this project, the more complex flow around a variable thickness test surface is better documented. The variable thickness allows the pressure gradients and vortex to develop over a greater streamwise length until the maximum thickness is passed.

Except where noted, the following discussion is based on the results of Devenport and Simpson (1992), Fleming, Simpson, Cowling and Devenport (1993), and Olcmen and Simpson (1994). Typical variable thickness test surfaces are semi-elliptical airfoils with thickness, t , to chord ratios of 0.235 or 0.426.

Figure 1.5 from Devenport and Simpson (1992) shows the surface pressure and secondary flow field for a variable thickness test surface. Again, separation occurs in the

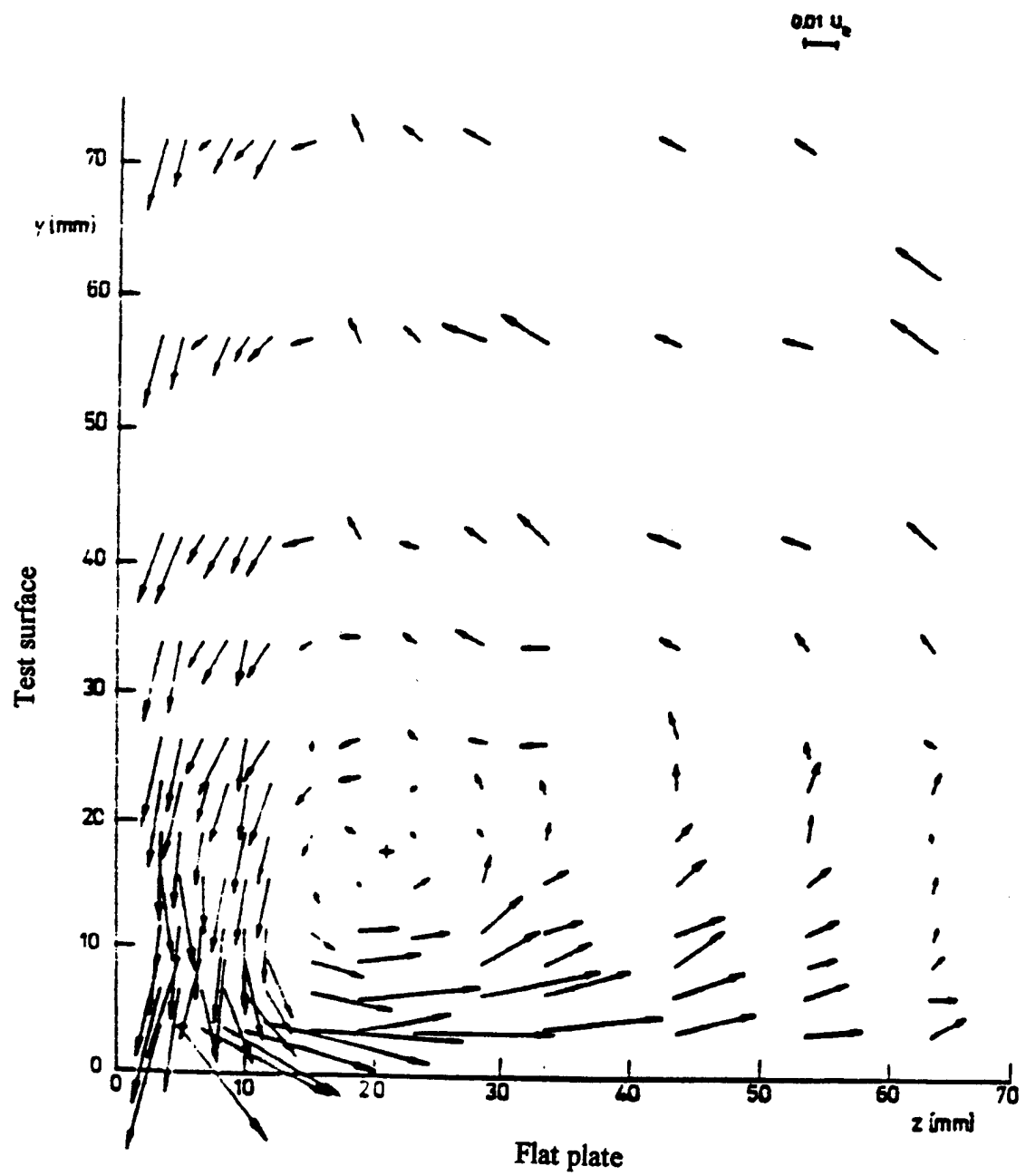


Figure 1.4 The secondary flow pattern from Shabaka (1979).

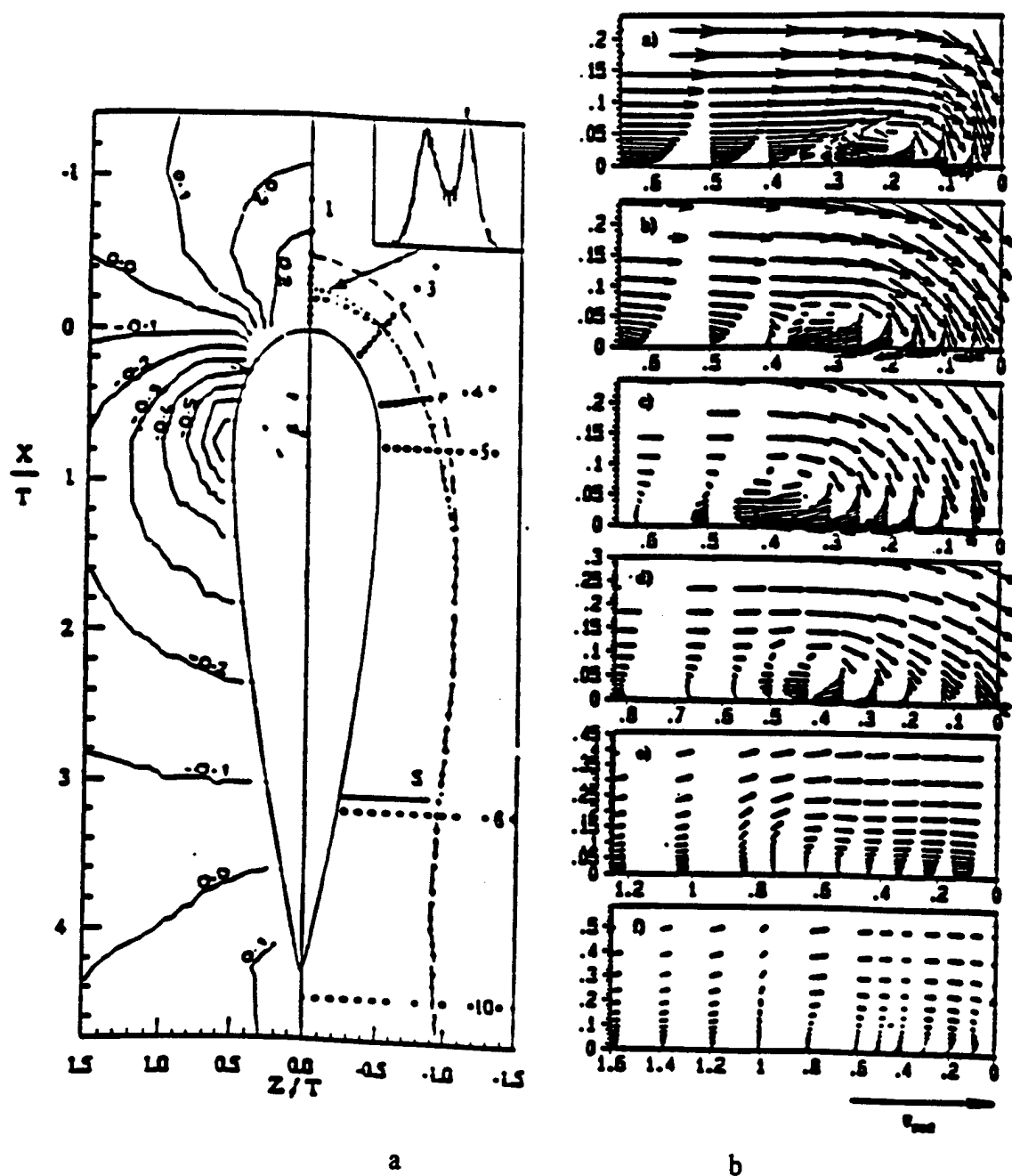


Figure 1.5 The surface pressure and secondary flow field for a variable thickness appendage from Devenport and Simpson (1992). In a, the contours of the mean surface pressure coefficient on the wall surrounding the appendage are shown. The numbers 1, 3, 4, 5, 8 and 10 on the right side indicate LDV measurement locations. In b, the mean secondary flow field generated by the vortex is shown. From top to bottom are the LDV measurement planes represented by 1, 3, 4, 5, 8 and 10 in a.

plane of symmetry of the flat plate-test surface junction because of the adverse pressure gradient imposed by the test surface. In Figure 1.5a, the open circles correspond to planes of laser Doppler velocimetry (LDV) measurements and are numbered 1, 3, 4, 5, 8, and 10. The position of the maximum wall normal velocities, corresponding directly to the line of low shear (LOLS) location, is intimately related to the major flow features associated with the horseshoe junction vortex. Figure 1.5b shows the mean secondary flow field at the LDV stations. In the time mean, the separating flow consists of two fairly distinct regions. Low mean back flow velocities characterize a thin region upstream of the junction. The intense circulation of the mean junction vortex dominates a relatively thick region downstream of the junction. The flow structure in the junction is difficult to model. In the upstream region, turbulent stresses develop in a manner qualitatively similar to those of a two-dimensional boundary layer separating in an adverse pressure gradient. Near the junction vortex, the turbulent stresses are much greater and reach values larger than those normally observed in turbulent boundary layers. The large stresses are associated with bimodal (double peaked) histograms of velocity fluctuations. These observations are consistent with large-scale low frequency unsteadiness of the instantaneous structure associated with the junction vortex. This unsteadiness seems to be produced by fluctuations in the momentum and vorticity of fluid from the outer part of the boundary layer that is circulated as it impinges on the leading edge of the test surface. The region of bimodal flow surrounding the time mean junction vortex is one of intense turbulence production.

Downstream of the leading edge, the leg of the horseshoe vortex generates a pressure gradient in the Y-Z plane. A local minimum surface pressure exists below the

center of the vortex (above the flat plate) with pressure increasing as the distance from the vortex center increases. As Z decreases from the vortex center in Figure 1.5b, the corner is approached and high wall shear stresses are suggested. As Z increases from the vortex center, the two-dimensional boundary layer condition is approached.

The primary horseshoe vortex flow structure is near the flat plate. Its shape appears elliptical, possibly due to vortex meandering and the unsteadiness in the nose bimodal flow region. The wall no slip condition creates a thin layer of high negative vorticity underneath the primary vortex, which thickens away from the test surface and the LOLS.

By adding a leading edge fillet between the flat plate and test surface, the leading edge separation is eliminated. The associated horseshoe vortex does not form and the stability of the flow near the junction is improved. Similarly, Philips, Cimbala and Treaster (1992) showed that eliminating the leading edge separation in the junction of a flat plate and constant thickness test surface eliminates the vortex in the downstream corner.

Many flow features scale on t in all directions for a given variable thickness test surface geometry. The quantities u_{rms} , v_{rms} and \overline{uw} appear to scale on t in the Y direction, while w_{rms} and \overline{uv} seem to scale more appropriately on approaching boundary layer thickness, δ .

Downstream of the maximum test section thickness, the effect of decreasing θ/t is seen as a thinning of the boundary layer between the test surface and the vortex legs as shown in Figure 1.6 from Fleming, Simpson, Cowling and Devenport (1993).

Normalizing with the free stream velocity, the u_{rms}/U_{ref} contours for $X/c = 0.75$ and θ/t of

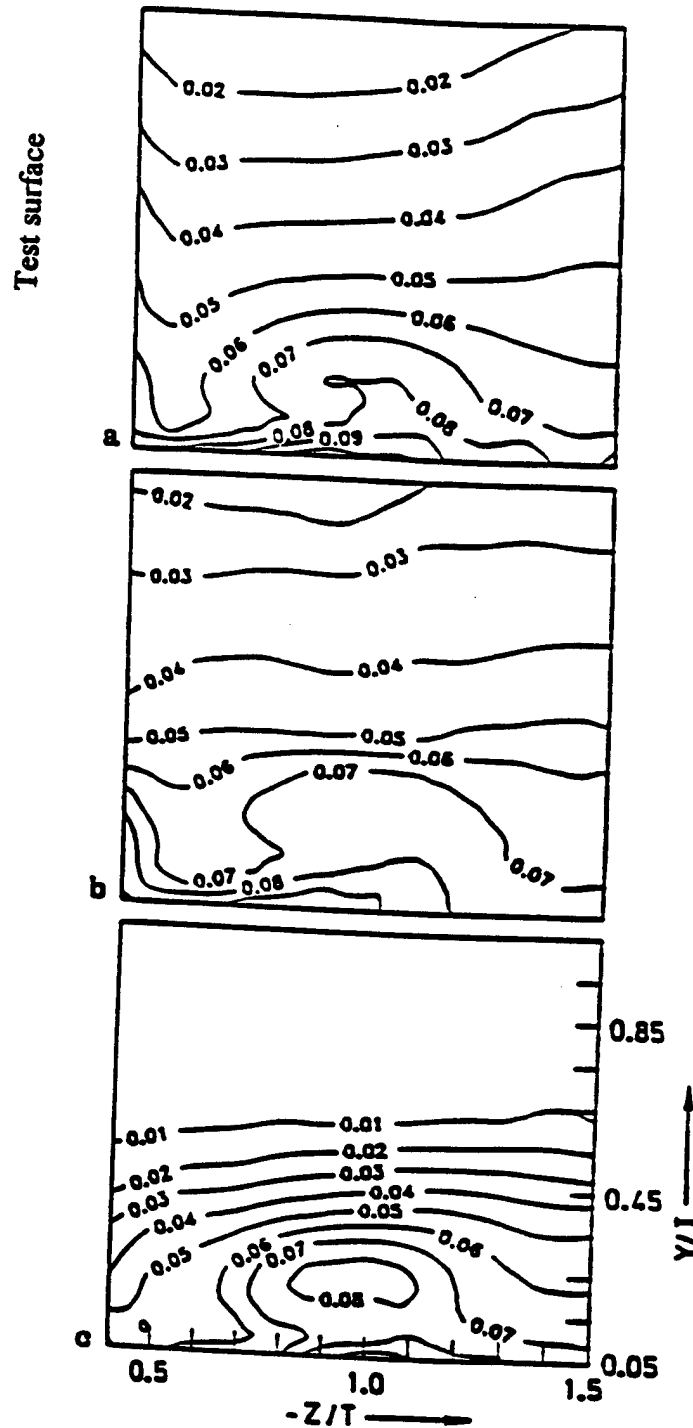


Figure 1.6 Comparison of u_{rms}/U_{ref} contours at $X/c = 0.75$ from Fleming, Simpson, Cowling, and Devenport (1993) for θ/t (a) 0.1014, (b) 0.1003, (c) 0.0548, respectively.

(a) 0.1014, (b) 0.1003, and (c) 0.0548, respectively, become more concentrated with decreasing θ/t . Here, the constant c is the chord of the test surface. Also, a distinct local maxima of u_{rms} can be seen.

Increasing Re_θ increases the local mean flow distortions and gradients near the wall in the nose region. A factor termed the momentum deficit factor (MDF), defined as $MDF = Re_t^2 \left(\frac{\theta}{t} \right)$, may directly affect the characteristics of the mean junction flow. MDF correctly predicts the variation in mean flow distortion magnitudes and horseshoe vortex characteristics between the data sets. Changes in MDF appear to modify the effective flow skewing around the test surface. Downstream of the maximum test section thickness, the results from Fleming, Simpson, Cowling and Devenport (1993) and reproduced in Figure 1.7 show the velocity contours and secondary velocity vectors for θ/t of (a) 0.1014, (b) 0.1003, and (c) 0.0548, respectively. In terms of MDF, Figures 1.6 and 1.7 are (a) 13.3×10^8 , (b) 4.61×10^8 , and (c) 7.24×10^8 . As MDF increases, the streamwise velocity distortions are not as large. The secondary flow patterns are more elliptic. Vorticity is increasingly concentrated in a near wall region. The vertical distance of the vortex core above the wall is decreased.

1.4. Stress induced secondary flow

Gessner and Jones (1961) and Bragg (1969) found that stress induced flow with symmetry of the secondary flow about a corner bisector is difficult to achieve in an experiment. This implies that this type of internal flow is unlikely except in controlled laboratory experiments. With both duct leading edges starting at the same point, the

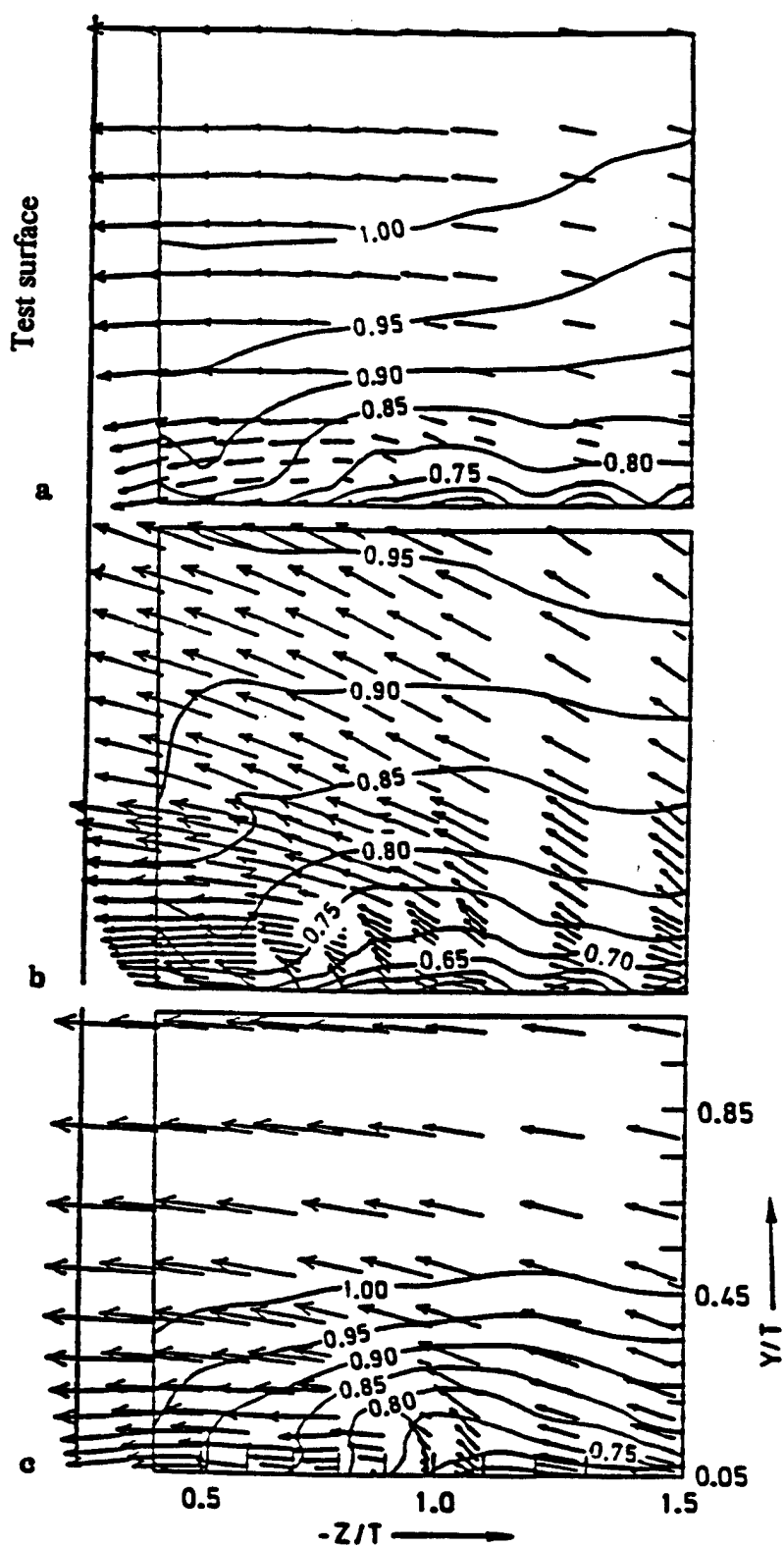


Figure 1.7 Comparison of U/U_{ref} contours and secondary velocity vectors at $X/c = 0.75$ from Fleming, Simpson, Cowling, and Devenport (1993) for θ/t (a) 0.1014, (b) 0.1003, (c) 0.0548, respectively.

boundary layers develop at an equal rate. The duct leading edge location for all four edges must be coincident.

Studies of this case concentrate on the effects of the geometry, the pressure gradient, and the Reynolds number. The mechanism creating the secondary flow is the Reynolds shear stress gradient in the corner while the normal Reynolds stresses do not have a dominant role. This mechanism is represented by terms 3 and 4 on the right hand side of the axial vorticity equation, equation (1.1). It also applies to developing turbulent boundary layer flow in a duct. The number and shape of the secondary flow cells are related to the distribution of the shear stresses.

To study the effect of geometry on corner flow in square and rectangular ducts, we examine the aspect ratio and the corner angle. The aspect ratio is the ratio of the width of the vertical wall to the width of the horizontal wall. The corner angle is the angle formed by the vertical and horizontal walls.

In Figure 1.8, the left side illustrates the primary flow contour in a square duct corner with smooth walls. The Y and Z dimensions are normalized with the duct width, b . Looking at the lower left quadrant, a line of symmetry can be drawn at a 45° angle from the corner. A line of symmetry in each quadrant also occurs in the secondary velocity pattern and is illustrated on the left side of Figure 1.9. The line of symmetry does not exist in rectangular ducts.

As the aspect ratio is increased, a greater portion of the secondary flow away from a corner is directed along the longer wall. Thus, the shape of the secondary flow cell changes.

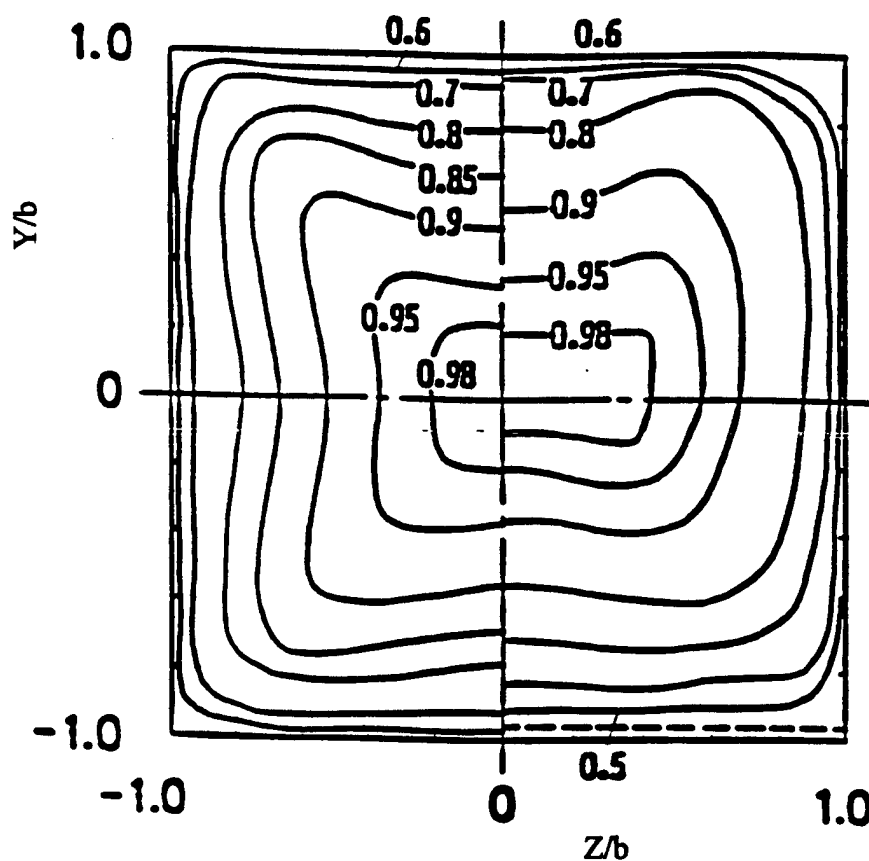


Figure 1.8 The primary flow velocity contours, U/U_* , for square ducts from Fujita, Yokosawa and Hirota (1989): left side, smooth duct; right side, duct with one rough surface indicated by dashed line; U_* is the maximum primary flow velocity.

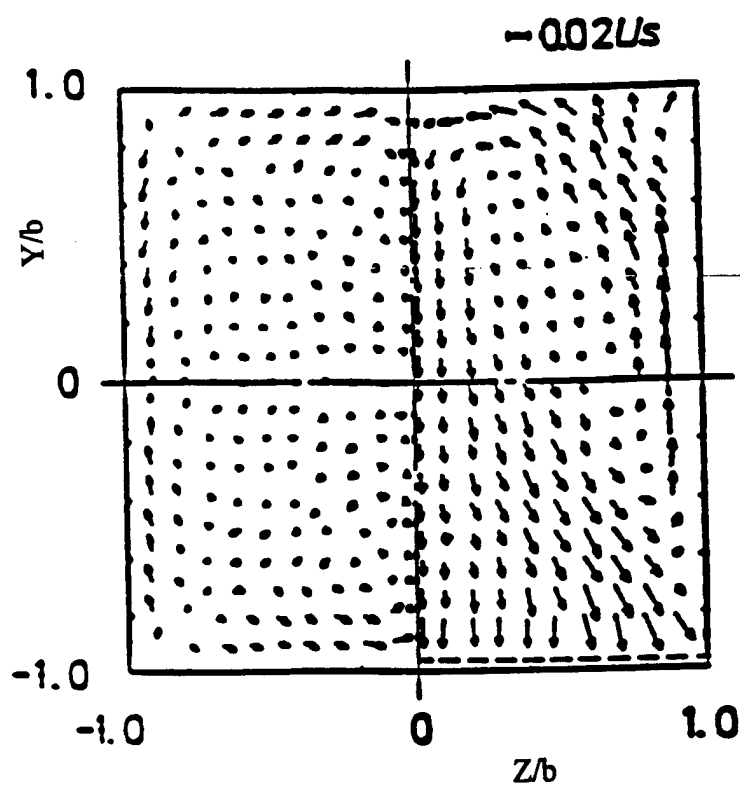


Figure 1.9 Secondary flow pattern for square ducts from Fujita, Yokosawa and Hirota (1989): left side, smooth duct; right side, duct with one rough surface indicated by dashed line; U_s is the maximum primary flow velocity.

Typical experiments use a duct with walls forming a 90° angle. Separation occurs at the junction of the vertical and horizontal walls as demonstrated by Perkins (1970). Replacing the 90° corner with a fillet can delay or prevent the separation.

The axial pressure gradient affects the secondary flow direction. With a zero pressure gradient or an adverse pressure gradient, the secondary flow proceeds into the corner along the line of symmetry and away from the corner along the walls. However, in a favorable pressure gradient, the secondary flow proceeds along the walls toward the corner and outward along the corner bisector. These results also apply to rectangular ducts with a zero pressure gradient. Mojola (1978) confirmed this through theoretical analysis. The secondary flow exhibits a Reynolds number dependence. A decrease in secondary flow velocity occurs with an increase in Reynolds number.

1.5. Flow above a rough surface

In the research presented above, all wall surfaces were smooth. Roughened surfaces can result from the machining of metal or from biofouling of surfaces in a marine environment. Schultz and Swain (1999) summarized the roughness effect from biofilms on turbulent boundary layers. The reader is referred to the extensive review of rough wall turbulent boundary layers by Raupach, Antonia, and Rajagopalan (1991). A general discussion of turbulent boundary layer flow above a rough surface follows.

Researchers have studied turbulent rough wall boundary layer flows using different sized two and three-dimensional roughness elements. Examples of the two-dimensional roughness elements are the d type and k type. For the d type surface, the ratio of the distance between roughness elements to an element height is less than one

while for the k type surface it is greater than one. Bandyopadhyay and Watson (1988) employ d and k type elements, uniform rectangular strips mounted cross-stream on a flat plate. Raupach (1981) uses cylindrical shaped elements arranged in either diamond or square patterns with varied densities. Krogstad, Antonia, and Browne (1992) use thick mesh screen to simulate three-dimensional roughness elements. These researchers examine the velocity profiles and higher order moments and attempt to determine the wall normal location where the axial velocity is zero. They also develop models to classify the flow and accurately describe the velocity profile, friction velocity and coefficient of friction.

Taylor, Coleman and Hodge (1985) propose three flow regimes comparable to those of White (1974). Based on R_τ , ($R_\tau = \frac{\tau_r}{\tau_T}$), the ratio of the apparent shear stress due to the form drag of the roughness elements, τ_r , to the total apparent wall shear stress, τ_T , the regimes are as follows,

Aerodynamically smooth regime: $0 < R_\tau < 0.05 - 0.10$,

Transitionally rough regime: $0.05 - 0.10 < R_\tau < 0.80-0.90$,

Fully rough regime: $R_\tau > 0.80-0.90$.

The wall shear stress is defined as the sum of the shear and form drag forces on the wall in the mean flow direction divided by the plan area of the wall.

While the origin on a smooth surface is at $Y = 0$, the origin on a rough surface is not well defined. Assuming that the roughness elements are attached above the smooth surface, the origin will exist between $0 < Y < k$ or k_s , where k is the average height of the roughness elements and k_s is the equivalent sand roughness. Hinze (1975) defines k_s as

the size of uniform sand grains that produce the same wall shear stress as the actual roughness under the same flow conditions.

The roughness elements may eliminate the viscous sublayer and displace the logarithmic or overlap layer away from the surface. If $k^+ > 60$, roughness elements disrupt the viscous sublayer and a completely rough wall condition exists. For this case, a roughness sublayer exists in the inner layer. The geometry and density of the roughness elements affect the location of the origin. For roughness of a uniform nature such as sand or spheres, the origin is located approximately $0.75 k$ above the location $Y = 0$. However, the origin approaches the top of the elements when the ratio of the roughness element's cross-stream span to the height of the gap between elements decreases, i.e. the density of roughness elements increases.

White (1974) assumes that the effect of roughness is the same on a flat plate as in a pipe. That is, the outer region in the boundary layer is unaffected by the roughness. Just as for a smooth flat plate, an overlap region must exist joining the inner and outer regions. Assuming a logarithmic profile, the equation is,

$$u^+ \approx \frac{1}{\kappa} \ln y^+ + 5.5 - \frac{1}{\kappa} \ln(1 + 0.3k^+) \quad (1.3)$$

where $\kappa = 0.41$. As k^+ becomes very large, the term $(1 + 0.3k^+) \approx 0.3k^+$.

In White (1974) the skin friction coefficient for the fully rough regime is related to Re_x and k/x as follows,

$$Re_x = 1.73125(1 + 0.3k^+) \exp \left(0.4 \sqrt{\frac{2}{C_f}} \right) x \left(\left(0.4 \sqrt{\frac{2}{C_f}} \right)^2 - 4 \left(0.4 \sqrt{\frac{2}{C_f}} \right) + 6 - \frac{0.3k^+}{1 + 0.3k^+} \left(0.4 \sqrt{\frac{2}{C_f}} - 1 \right) \right) \quad (1.4)$$

This formula is valid for $(x/k) > 100$. C_f increases on a rough surface relative to a smooth surface.

In addition to White's empirical equations, at least two methods have been proposed recently to describe the coefficient of friction and friction velocity over three-dimensional roughness elements. The first approach by Taylor, Coleman and Hodge (1985) models the boundary layer based on individual or discrete elements. The second approach by Waigh and Kind (1998) employs a modified law of the wall.

Taylor et al. (1985) and Taylor, Scaggs and Coleman (1988) modeled the roughness as discrete elements. The corresponding skin friction coefficient is based on a blockage factor and a drag coefficient for the control volume shown in Figure 1.10. The areas available for mass and momentum transport in the control volume decrease with the presence of the roughness elements. The areas that shear stresses and pressures act on also decrease.

The equation for the skin friction coefficient is,

$$C_f = \frac{C_1 + C_2}{C_3} \quad (1.5)$$

where C_1 is the wall shear stress and blockage factor, C_2 is the form drag, and C_3 is the dynamic pressure. The form drag term will be affected by an unknown contribution between the origin and the first measurement point. The effect of the sharp edges of the roughness elements is also unknown. Thus, the equation may not accurately represent the value of C_f .

An alternative approach suggested by Waigh and Kind (1998) involves three-dimensional roughness elements arranged in uniform patterns and their effect on the logarithmic law of the wall. For surfaces that are fully rough, the law of the wall is,

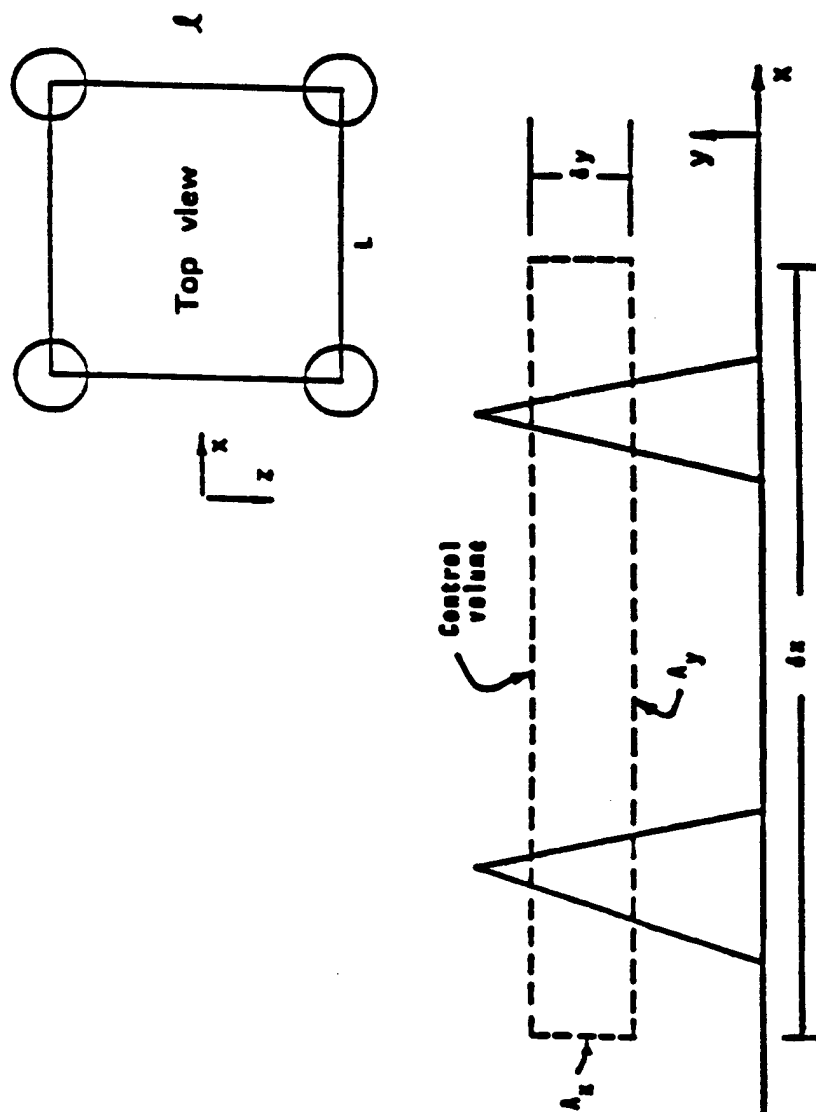


Figure 1.10 Control volume for flow over a rough surface from Taylor, Coleman, and Hodge (1985).

$$\frac{u}{u_\tau} = \frac{1}{\kappa} \ln(y/k) + C_o - C \quad (1.6)$$

Comparing equations (1.6) and (1.3), we see that the new equation is scaled on the roughness height and incorporates a roughness constant, C , that includes the effect of the element distribution. To describe C , they suggest using a complicated series of parameters to account for element spacing and aspect ratio.

The density of roughness elements on the surface correlates with the roughness constant, C . Two regimes exist – a sparse and dense regime. The regime depends on the ratio of the total volume over the surface (out to height k) to the effective volume of the roughness elements. For the two regimes, a correlation was developed for C that depends on the ratio of k to an element's cross-stream width, the ratio of an element's wetted area to its projected frontal area, and a spacing parameter. The spacing parameter, λ , relates the area of a rough surface to the projected frontal area of an element. For the interval $2 < \lambda < 10$, there is an overlap between the dense and sparse regimes and the C correlation depends on the volume ratio. In addition, the cell aspect ratio and the cross-stream separation do not appear to affect the roughness constant significantly. This suggests that the roughness constant is insensitive to the pattern of the roughness array.

Above roughness elements, the mean velocity profile in Figure 1.11 exhibits a logarithmic behavior with a lower intercept than for a smooth surface. The mean velocity distribution indicates that the strength of the rough wall outer region wake is larger than on a smooth wall.

Examining the Reynolds stresses above rough surfaces and normalizing on the wall shear stress, Krogstad, Antonia and Browne (1992) note that there is a significant increase in the normal turbulence intensity and a moderate increase in the Reynolds shear

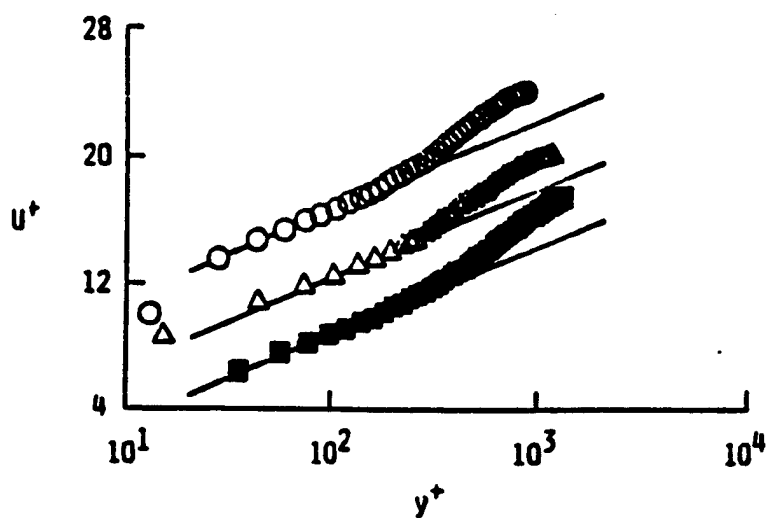


Figure 1.11 Mean velocity profiles from Bandyopadhyay and Watson (1988): the open circles represent smooth surface, the open triangles, d-type walls, and filled squares, k-type walls.

stress. The longitudinal turbulence intensity distribution is essentially the same for smooth and rough surfaces.

Figure 1.12 from Bandyopadhyay and Watson (1988) shows the ratio of Reynolds shear stress to turbulent kinetic energy, $a_1 = \frac{-\overline{uv}}{(u_{rms}^2 + v_{rms}^2 + w_{rms}^2)}$, above a rough surface.

The nearly constant value of a_1 for $0.1 < y/\delta < 0.8$ indicates that the shear stress and turbulent kinetic energy change in the same manner.

By applying quadrant analysis, Raupach (1981) demonstrated that sweeps account for most of the stress close to k type rough surfaces. In comparison, ejection motion above a rough surface dominates the Reynolds stress beyond $y^+ \approx 12$. The relative magnitude of the sweep component increases with surface roughness and with proximity to the surface. The sweep-dominated region delineates a roughness sublayer with a depth of up to several roughness element heights. In this region, the turbulence characteristics depend explicitly on the roughness. In the remainder of the inner region and in the outer layer, the flow obeys familiar similarity laws with respect to surface roughness.

As shown in Figure 1.13, the axial skewness component normalized by the friction velocity cubed is positive in the near wall region and negative in the outer wall region, similar to results for a smooth flat plate. The wall-normal skewness component similarly normalized is positive through the range of measurement, again similar to results for a smooth flat plate.

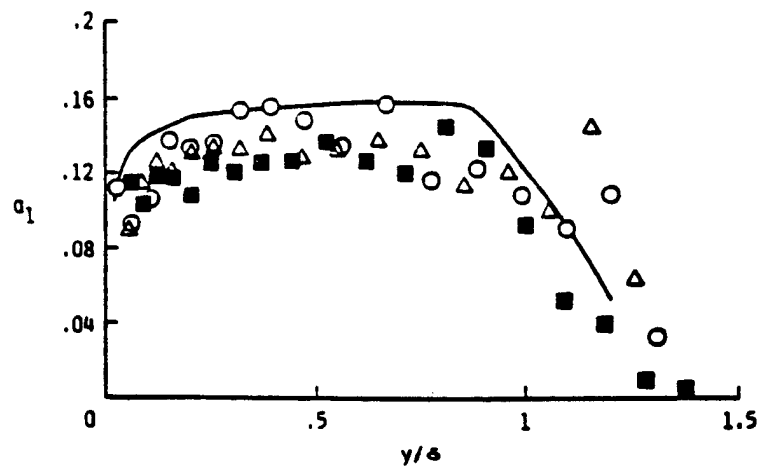
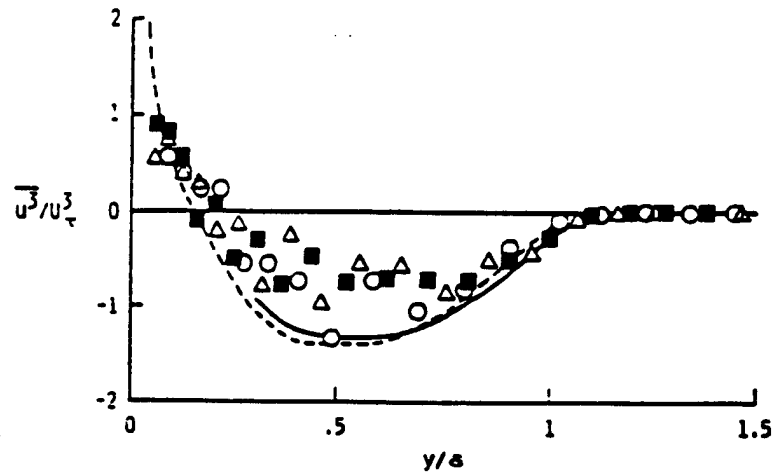
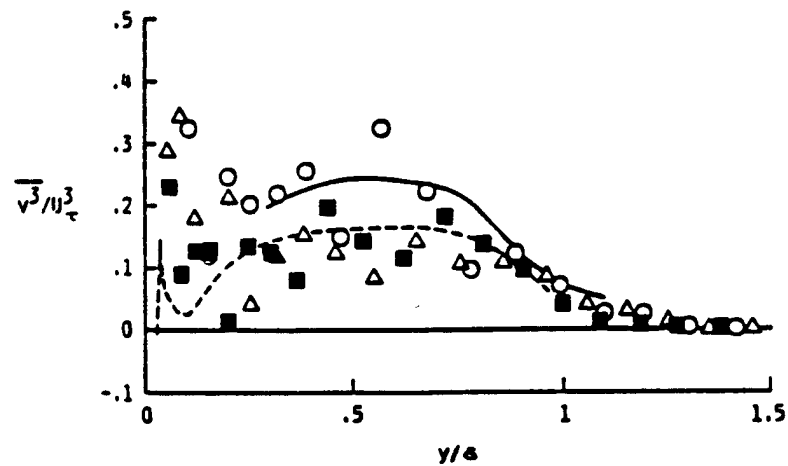


Figure 1.12 Ratio of Reynolds stress to turbulent kinetic energy from Bandyopadhyay and Watson (1988): the solid line, smooth surface at $Re_\theta = 8000$, others as in Figure 1.11.



a



b

Figure 1.13 Axial third moment (a) and wall-normal third moment (b) from Bandyopadhyay and Watson (1988): the solid line, smooth surface at $Re_\delta = 4750$, broken line, sand grain at $Re_\delta = 1.7 \times 10^5$.

1.6. Stress induced secondary flow with one rough wall

The rough wall stress induced case results from one wall in a channel or duct being rough. Fujita, Yokosawa, and Hirota, (1989) mount 1 mm square strips, ie. two-dimensional roughness elements, on one duct wall and space the strips 10 mm apart. Humphrey and Whitelaw (1979) also use square strips with 3.95 mm sides spaced 39.5 mm apart on one duct wall.

On the right side of Figure 1.8, the primary flow contours reproduced from Fujita et al. show a vortex occurring about a bisector through the rough surface centerline. Similarly, the right side of Figure 1.9 shows the secondary velocity vectors. The surface condition eliminates the two vortices that would occur in a quadrant for the smooth wall case. Instead, only one large longitudinal vortex appears in each half of the channel in the corners formed by the smooth walls. The secondary flow moves away from the rough surface along the smooth wall and returns along the centerline of the rough surface. The secondary flow proceeds downward from the top smooth wall to the bottom rough wall along the duct mid plane. From the corner, the flow then proceeds up the vertical smooth walls. Results from Fujita et al. and Humphrey and Whitelaw (1979) confirm that the typical cell pattern of pairs of contra rotating longitudinal vortices in each quadrant in a square duct with smooth walls does not occur.

Humphrey and Whitelaw (1979) found that the Reynolds stresses at the rough wall are four times larger compared to the stresses at the smooth walls. Humphrey and Whitelaw associate this with the strong generation of turbulent kinetic energy at the rough wall. The secondary flow velocity is greatly intensified by the existence of the roughness. Humphrey and Whitelaw find that the wall normal velocity near the corner,

over the rough wall, approached 25% of the bulk fluid velocity. The logarithmic law applied at the centerline of the test section. However, departure from the law becomes significant in the corner where the secondary velocity strongly affects the flow. Through a vorticity balance, Fujita, Yokosawa, and Hirota, (1989) find that the production of vorticity is very active in the corners formed by the rough and smooth surface.

1.7. Objective

The objective of this investigation is to develop a database for incompressible, three-dimensional, zero axial pressure gradient, turbulent flow along a corner with one rough wall. The database will allow computational models to be developed and evaluated relative to the three component coincident results.

This study will use a boundary layer hot wire probe to measure the two-dimensional boundary layer flow near the center of the flat plate test surface. This will allow for more rapid data collection. To detail the turbulent boundary layer in the corner, we will employ an LDV to collect three component coincident velocity data. The mean velocity, turbulence intensity, Reynolds shear stress and triple velocity correlations will be analyzed.

Chapter 2

Experimental apparatus and instrumentation

2.1. Experimental Facility

All measurements were conducted in a low speed, wind tunnel at The Pennsylvania State University Applied Research Laboratory. The wind tunnel is shown in Figure 2.1. A variable speed fan draws air through a filtered inlet and sends it into a circular to square transition, a diffuser and a plenum containing ten stainless steel mesh screens. Following the plenum chamber, an area change reduces the 1.22 m square section to a 0.41 m square section. We note, however, that the smooth wall data was collected in the test section with dimensions of 1.83 m (L) x 0.20 m (W) x 0.20 m (H). To improve optical access, the rough wall data was taken in the test section with dimensions of 1.83 m (L) x 0.41 m (W) x 0.20 m (H). The junction of the horizontal and vertical walls forms a 90° corner and the test surface is the horizontal surface.

The test section has two acrylic walls for optical access. The horizontal test surface is made of painted black wood with an elliptically shaped leading edge and has a constant thickness of 19 mm. Its leading edge has a slenderness ratio of 1.33:1. As measured with a surface roughness profilometer, the roughness of each surface is equal to or less than 1.016×10^{-6} m ($k^+ = 0.04$), i.e. a hydrodynamically smooth plate. The flow is tripped using an 89 mm length of 40 grit (0.8 mm) sandpaper attached 41 mm downstream of the leading edge of the horizontal surface. An adjacent section of equal

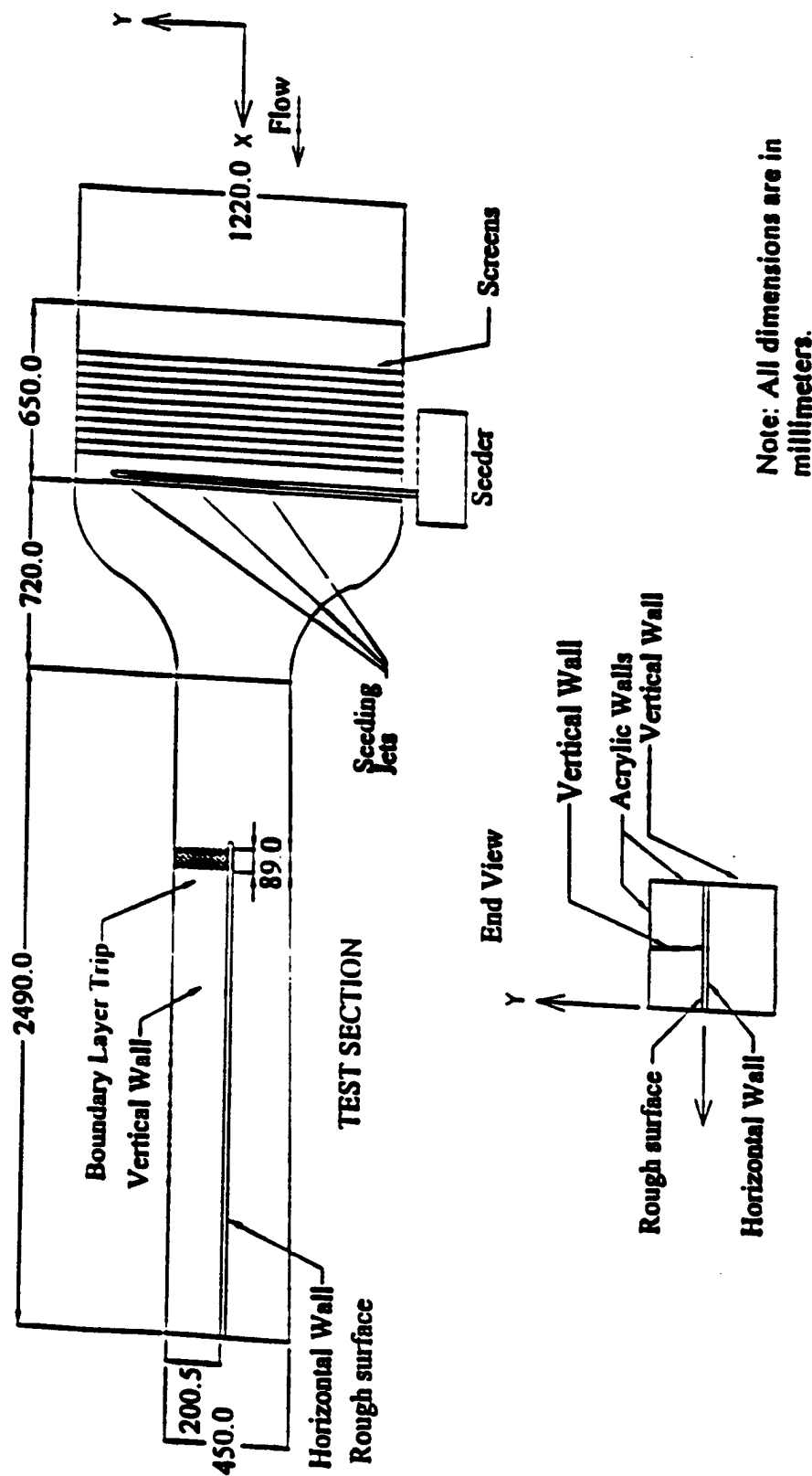


Figure 2.1 Wind tunnel schematic.

sized sandpaper is on the vertical surface. The boundary layer virtual origin for the smooth test surface is 175 mm upstream of the leading edge.

To study the roughness effect, sandpaper is attached to the smooth horizontal surface. The sandpaper turbulent boundary layer trip is replaced and the rough test surface extends from 25 mm downstream of the leading edge through the entire test section.

The 3M Corporation manufactures a sandpaper with an average roughness height of 1.73 ± 0.48 mm; that is a $k^+ = 65$. The roughness element height is based on an average of one hundred twenty surface measurements made at the corner flow laboratory at the Applied Research Laboratory and has a 95% confidence interval. Produced under the name Resinite, with the designation Floor Surfacing, Combination Type F, Open Coat, 16 - 4 Grade, the sandpaper is packaged in 0.2 m (W) x 45.7 m (L) rolls. As shown in Figure 2.2, the roughness elements are randomly placed on the surface and have individual shapes resembling rectangles that are randomly aligned. Using the approach from Krogstad and Antonia (1999), the roughness is characterized as k type. The average length is 2.62 ± 1.27 mm and the average width is 1.61 ± 0.68 mm. The smallest roughness element dimensions are eleven times larger than the probe volume diameters. The boundary layer virtual origin for the rough test surface is 1500 mm upstream of the leading edge. Typical experimental conditions are listed in Table 2.1.

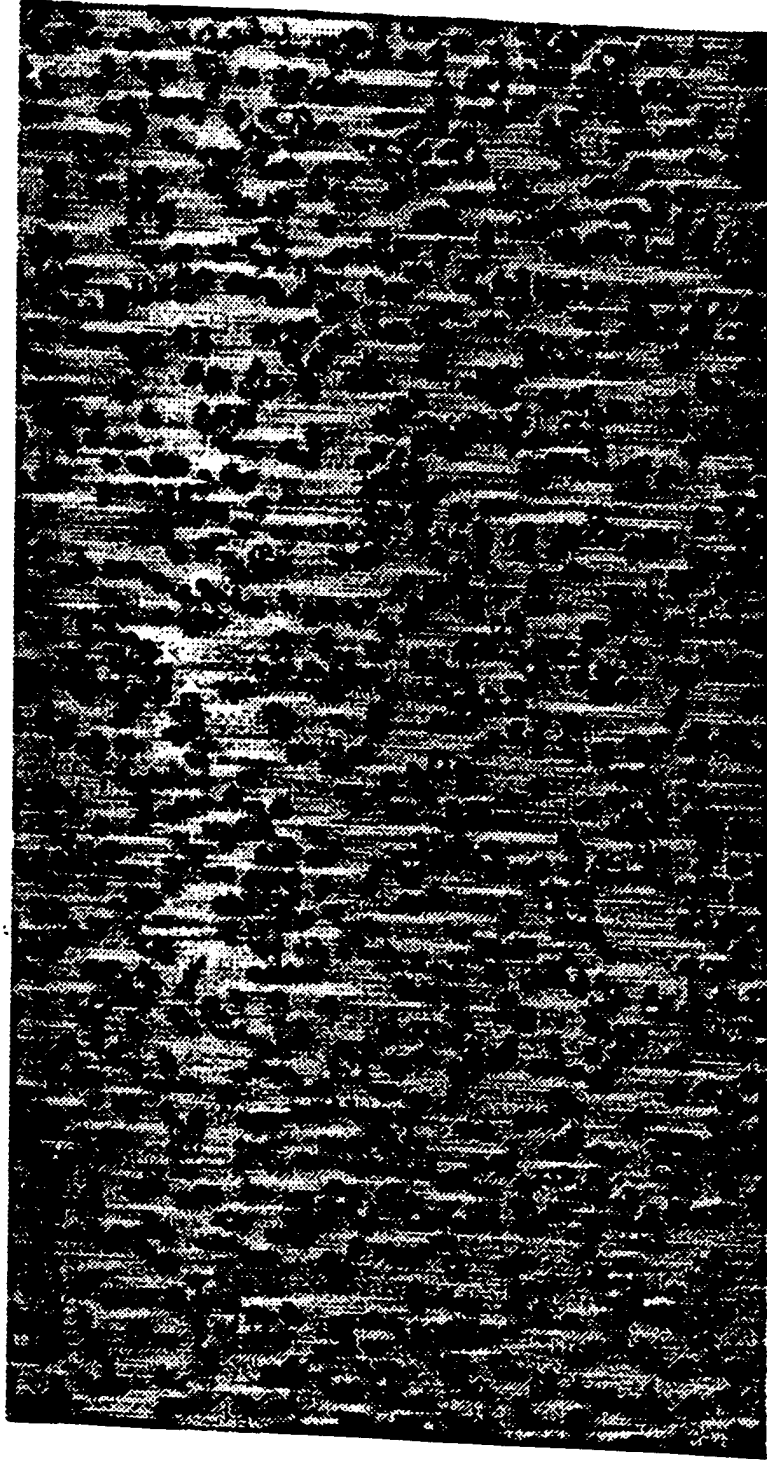


Figure 2.2 Illustration of the rough surface manufactured by 3M Corporation.

Table 2.1 Typical experimental conditions.

Air Density	1.2 kg/m ³
Free Stream Velocity	13.1 m/s
Kinematic Viscosity of Air	0.0000151 m ² /s
Pressure	97.7 kPa
Temperature	24 C

The two primary measurement tools are the LDV and the boundary layer hot wire probe. The LDV system allows two and three component velocity measurements through the corner layer without disturbing the corner flow. Away from the corner, the hot wire probe allows for a more rapid measurement of the two-dimensional boundary layer. The two specific systems employed are discussed below.

2.2. Laser Doppler Technique-General Considerations

The laser Doppler velocimetry (LDV) technique is based on the Doppler shift of laser light that is scattered from particles traveling in a fluid. This is a general discussion of LDV and the information pertaining to the current experiment is in section 2.4. Except where noted, the following discussion is based on Durst, Melling and Whitelaw (1981), Adrian (1983) and Drain (1988).

2.2.1. Differential Doppler Technique

Milonni and Eberly (1988) discuss the Doppler shift technique. By directing a laser beam of frequency f' at a particle moving in a fluid, the scattered radiation has a Doppler

shifted frequency, f^* such that $f^* \approx \left(1 - \frac{\tilde{u}}{c}\right) f'$ where c is the speed of light in a vacuum and \tilde{u} is the particle velocity. The Doppler shift, $\tilde{u}f' / c$, is detected by optical heterodyning.

The principle of heterodyning or beating of two frequencies is applied to measure very small Doppler shifts. Heterodyning is a technique in which two signals, the laser light at two frequencies, are added and passed through a non-linear circuit, the photodetector. The mixed output then contains the sum and difference frequencies and harmonics. If the original frequencies are close, a filter can separate the difference frequency.

In Figure 2.3, this is extended to the dual beam mode of heterodyne detection. The two beams, E_{o1} and E_{o2} , are focused to form a control volume. The angle between the two light waves is 2κ . As particles pass through the volume, the light waves are scattered and light waves E_1 and E_2 are collected at a receiver with a photodetector.

Assuming that the two light waves are represented as two signals, $\epsilon_1 \cos \omega_1 t$ and $\epsilon_2 \cos \omega_2 t$, they are combined at the square law photodetector. The photodetector is sensitive to total light intensity and the signals produce an intensity,

$$I = \epsilon_0 c (\epsilon_1 \cos \omega_1 t + \epsilon_2 \cos \omega_2 t)^2 \quad (2.1)$$

where ϵ_0 is the Coulomb force constant. Expanding (2.2), the intensity equation becomes,

$$I = \epsilon_0 c \left[\frac{1}{2} \epsilon_1^2 (1 + \cos 2\omega_1 t) + \frac{1}{2} \epsilon_2^2 (1 + \cos 2\omega_2 t) + \epsilon_1 \epsilon_2 \cos(\omega_1 + \omega_2)t \right. \\ \left. + \epsilon_1 \epsilon_2 \cos(\omega_1 - \omega_2)t \right] \quad (2.2)$$

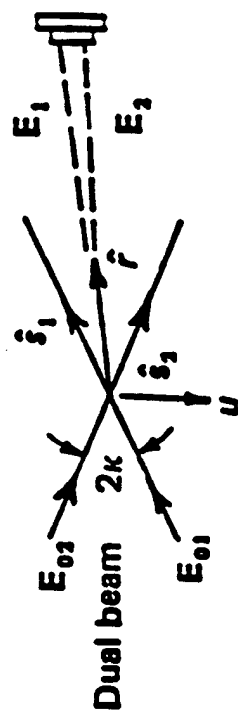


Figure 2.3 Dual beam mode of heterodyne detection in laser Doppler velocimetry from Adrian (1983).

The oscillations at frequencies $2\omega_1$, $2\omega_2$, and $(\omega_1 + \omega_2)$ are too rapid to be followed by available detectors. The frequency, $(\omega_1 - \omega_2)$, is typically the order of megahertz for laboratory velocity applications and is within the range of detectors.

2.2.2. Interference Fringes

The spatial resolution of a dual beam system is affected by the distribution of the light intensity at the intersection of the two focused beams, referred to as the probe or measurement volume. The laser is in the TEM₀₀ mode, which means that the laser cavity sustains a purely longitudinal standing wave oscillation along its axis with no transverse modes. The laser output has an axisymmetric intensity profile. It is approximately a Gaussian function of radial distance from the axis. In the far field, the beam divergence is small enough to appear as a spherical wave from a point source located at the front of the lens.

The behavior of the Gaussian beams is shown in Figure 2.4. Assuming zero aberration, the lens converts the beam, a spherical wave, into a converging spherical wave. The radius of this wave decreases until the distance s_1 is reached. At s_1 , the beam has a nearly constant diameter and has nearly planar behavior. The location s_1 is the focal length of the lens and the laser beam is focused to its minimum diameter or beam waist. The intensity distribution in the beam waist of a focused Gaussian beam is Gaussian. The beam waist, $D_{e^{-2}}$, is the diameter of the laser beam between the points where the intensity is $1/e^2$ of the peak intensity. The focal waist, $d_{e^{-2}}$, is defined by,

$$d_{e^{-2}} = \frac{4\lambda f}{\pi D_{e^{-2}}} \quad (2.3)$$

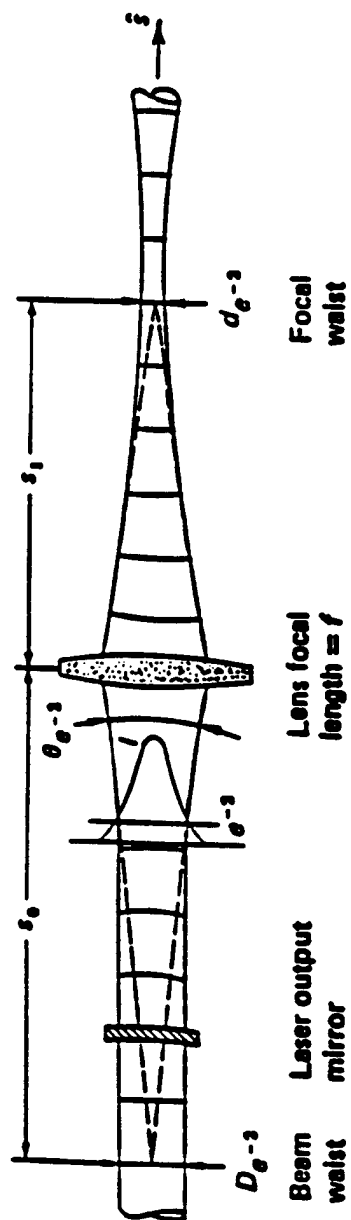


Figure 2.4 Properties of a focused Gaussian beam from Adrian (1983).

where λ is the wavelength of the laser beam and f is the lens focal length.

The two laser beams create alternating fields at the point of crossing. Assuming that each beam has a well defined frequency and a consistent phase relationship, light and dark bands known as interference fringes are observed. The lines of equal fringe amplitude are centered on the cross over point and are spaced as,

$$d_f = \frac{\lambda}{2 \sin(\kappa)} \quad (2.4)$$

where d_f is the fringe spacing and κ is the half angle between the beams.

For the axial velocity component, the fringes are formed in the y-z plane to measure particles moving in the x direction. The number of fringes, N_{FR} , in the volume is,

$$N_{FR} = \frac{1.27d}{D_e^{-1}} \quad (2.5)$$

where d is the beam spacing.

For the dual beam mode, a coherent signal can occur if one particle resides in the measurement volume. For a valid signal, the light waves must appear to originate at a small, coherently illuminated region. Assuming that light waves from two separated sources are collected and focused at the surface, mixing occurs at the detector surface. If the light waves appear as spherical waves originating from a point source such as a micron sized particle, diffraction at the surface produces an image of the source. The image has a diameter on the order of $\lambda f/D_s$, where λ is the wavelength of the laser beam,

f_c is the collecting lens focal length and D_a is the diameter of the light collecting aperture. Heterodyne mixing occurs if the images are separated by less than the diffraction limited spot size.

The geometry of the nominal LDV measurement volume in Figure 2.5 is generated by a single pair of laser beams. Its ellipsoidal shape has an e^{-2} contour. The major axis dimension, l_m , and minor axis dimension, d_m , are functions of the beam half angle, κ , and the focal waist diameter, $d_{e^{-2}}$. The equations for l_m and d_m are as follows,

$$l_m = \frac{d_{e^{-2}}}{\sin \kappa} \quad (2.6)$$

$$d_m = \frac{d_{e^{-2}}}{\cos \kappa} \quad (2.7)$$

These dimensions are significant because the viscous wall unit should be larger than l_m while the particle diameter should be smaller than d_m .

2.2.3. Frequency Shifting

To determine the direction of a particle moving through the probe volume, one of the laser beams in a pair is frequency shifted. This causes the fringes in the probe volume to move at a constant speed in the positive or negative direction depending on the shift direction. A Bragg cell produces the frequency shift. In a Bragg cell, one laser beam from a pair passes through a transparent medium in which acoustic waves are travelling. Typically, the acoustic waves are generated using a piezoelectric transducer. If the angle between the laser beam and the acoustic waves satisfies the Bragg condition, reflections from successive acoustic wave fronts reinforce the laser beam. The beam frequency is

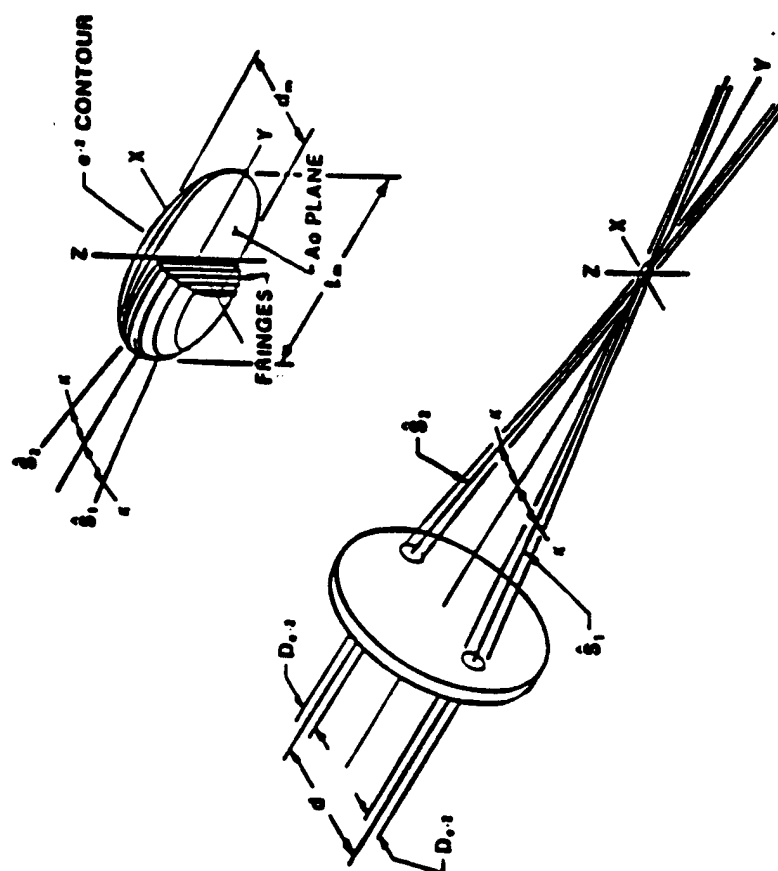


Figure 2.5 Geometry of the nominal LDV measurement or probe volume from Adrian (1983).

increased and after exiting the cell is reoriented using a prism to return the beam to its original direction.

Frequency shifting can eliminate angle or fringe bias. This bias occurs when the measurement system cannot measure all flow angles that are likely to be encountered in the flow with equal probability. Edwards (1987) recommends that the frequency shift be twice the highest expected Doppler frequency. The highest Doppler frequency can be estimated as follows,

$$f_d = \frac{U_{\max}}{d_f} \quad (2.8)$$

where f_d is the measured Doppler frequency, U_{\max} is the maximum velocity and d_f is the fringe spacing.

2.2.4. Multiple Velocity Components

Two or three components of velocity can be measured using two or three beam pairs focused at the same point in a flow. Each beam pair measures a velocity component from the same particle. This is referred to as the coincident mode. When multiple velocity components are collected, the measurement volume is reduced in principle to the volume created by the overlap of the individual measurement volumes. The maximum coincident data rate is limited by the laser beam pair with the lowest data rate, the coincident window setting, the alignment of the probe volumes, and seeding density. In the present experiment, the three-component coincident data rate is typically a sixth of the lowest of the individual beam pair data rates.

2.2.5. Signal processing

The laser system, the optics of the test section, and the particle characteristics in the flow affect the signal quality. Using the Mie Scattering Theory, Menon and Lai (1991) present a signal to noise ratio equation, SNR, to evaluate the LDV signal quality as follows,

$$\text{SNR} = A_1 * A_2 * \frac{A_3}{\Delta F} \quad (2.9)$$

where

$$A_1 = \frac{\pi^2 \eta_q P_o}{256 h \nu_o} \quad (2.10)$$

$$A_2 = \left[\frac{D_s D_{e-1}}{f_c f} \right]^2 \quad (2.11)$$

$$A_3 = d_p^2 \overline{GV}^2 \quad (2.12)$$

and the variables in equations (2.9) – (2.12) are as follows,

- SNR = signal to noise ratio (power)
- η_q = quantum efficiency of photomultiplier
- P_o = power of either laser beam in a balanced dual beam LDV, W
- ΔF = post-photomultiplier bandwidth, MHz
- λ = wavelength of laser light
- d_p = particle diameter, μm
- h = Planck's constant, 6.6×10^{-34} J-s
- ν_o = frequency of laser light
- D_s = diameter of light collecting aperture

D_{e-1}	= beam waist
f	= transmitting optics focal length
f_c	= collecting optics focal length
\overline{G}	= average light scatter gain
\overline{V}	= Doppler signal visibility

Term A_1 represents the influence of the laser and photodetector. Term A_2 represents the influence of various optical properties. Term A_3 represents the influence of the properties of the particle. The SNR equation does not account for reflections from windows or background surfaces. It does provide an understanding of the numerous parameters involved. For example, the properties of the particle affect the SNR through the square of the particle diameter. Its diameter affects the quantities \overline{G} and \overline{V} . The quantity \overline{G} is defined as the ratio of the actual flux of scattered light seen by the collecting aperture to the flux of isotropically scattered light seen by the collecting aperture. The quantity \overline{V} is defined as the ratio of the Doppler signal amplitude to the pedestal amplitude. Optimum SNR values will fluctuate depending on the given equipment settings, conditions and particle sizes and trajectories.

Particles moving at different velocities generate different Doppler bursts with differing frequencies. Figure 2.6 shows the typical LDV signals produced by various full and partial trajectories through the measurement volume and decomposed into pedestals plus Doppler bursts. The pedestal is a low frequency signal that can be removed from the total signal. In trajectory a, the total signal from a particle passing through the

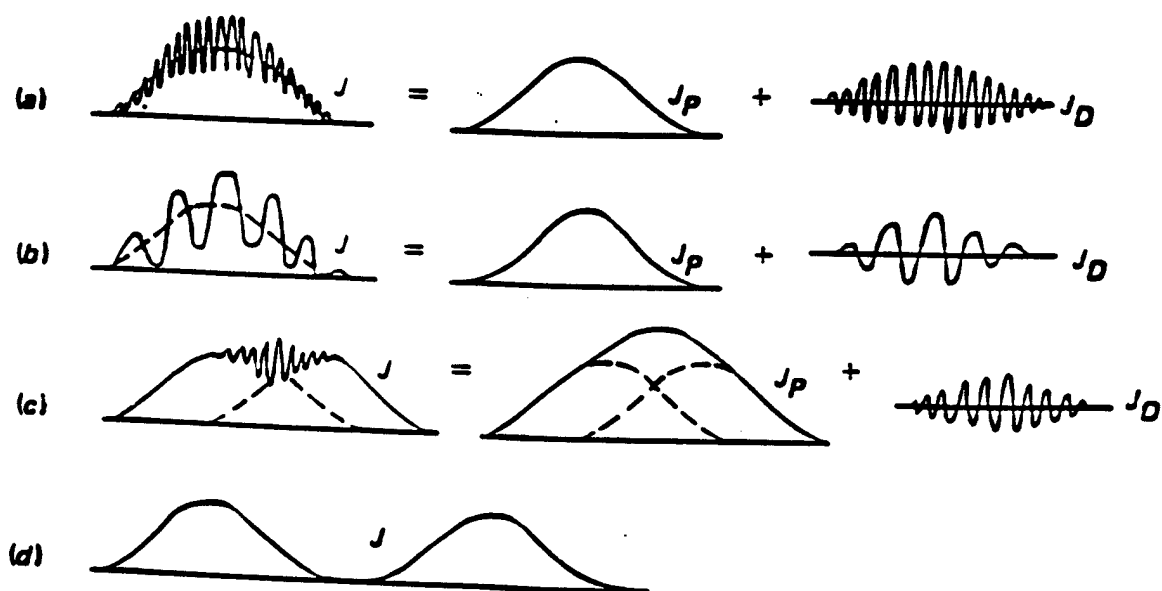
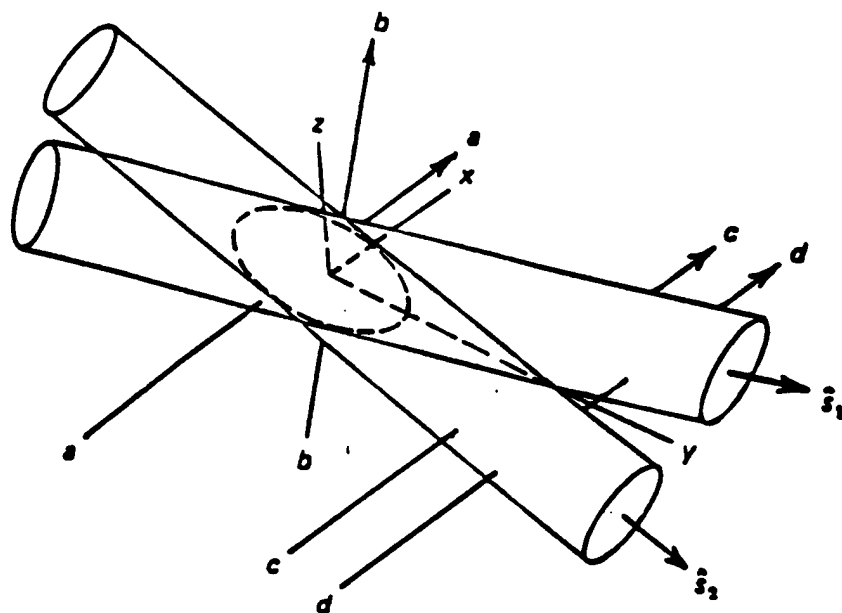


Figure 2.6 Typical LDV signals produced by various partial trajectories decomposed into pedestals plus Doppler bursts from Adrian (1983).

measurement volume near its center is split into its pedestal and Doppler signal.

Multiple fringes are passed and the signal is strong. Trajectory b passes through the measurement volume at an angle approximately bisecting the x-z plane. Few fringes are crossed and the signal is weaker. Particle c does not pass through the measurement volume and reflects light as it passes through the beam pair. Finally, trajectory d does not pass through the beam pair near the measurement volume. Its signal does not contain any Doppler burst.

2.2.6. Seeding

To seed the flow, a TSI model 9306 six-jet atomizer created propylene glycol particles of roughly 0.6 to 2.0 μm in diameter. The propylene glycol particle size distribution in Figure 2.7 shows that the largest population of particle sizes is between 0.6 and 0.7 μm . The seed was introduced to the flow immediately before the contraction leading to the test section. Two 11.1 mm copper tubes spanned the plenum in the Z direction. The seed passed through 4.8 mm holes spaced 50.8 mm apart along the tube length. At 0.61 m from the acrylic wall side, the holes were spaced 101.6 mm apart. The tubes were spaced 194 mm apart in the Y direction. The seed density at the measurement locations varied in the y direction with regions of lowest density corresponding to the midpoint of the tube spacing. For the rough surface, the tubes were removed and seed passed through the wall.

2.2.7. Sources of statistical bias

Possible sources of statistical bias in an LDV system are the velocity bias, the fringe bias, and the gradient bias.

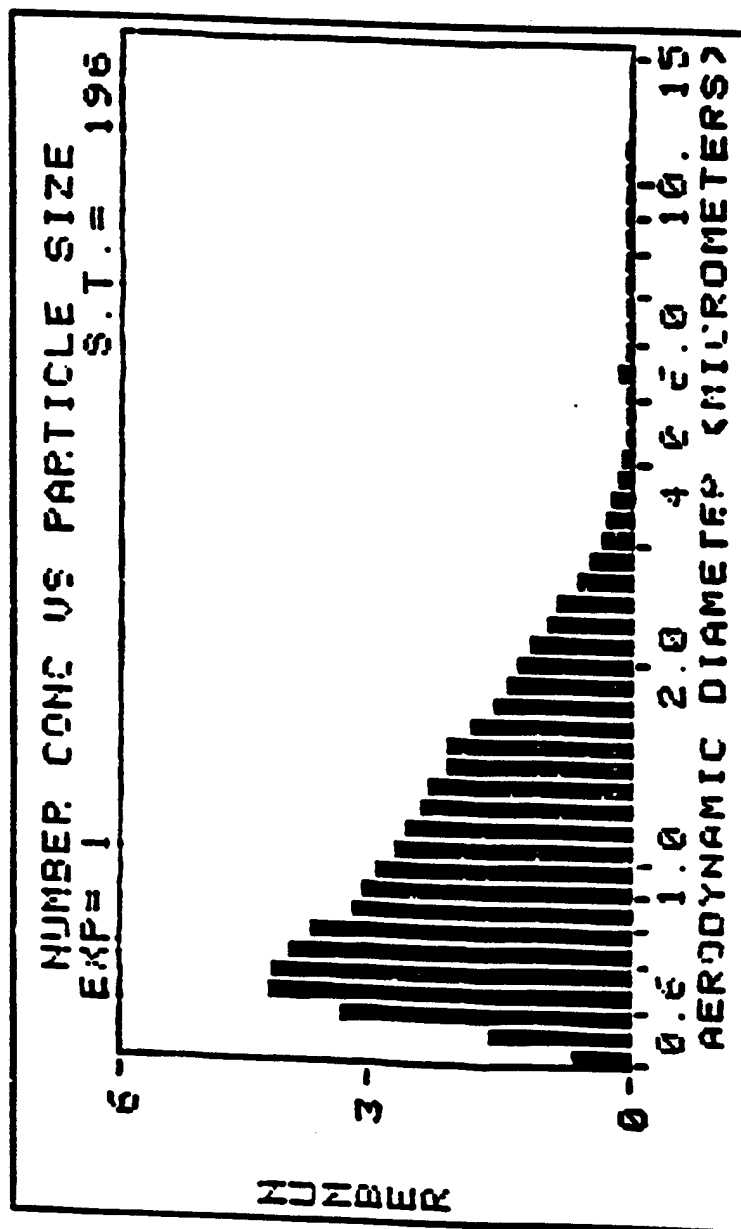


Figure 2.7 Particle size distribution of a propylene glycol aerosol from TSI Inc.

The velocity bias results from the flow dependent signals generated by single particles passing through the measurement volume. These measurements often cannot be averaged arithmetically for statistical measures of the particle velocity in the measurement volume, because the arrival rate of the particles is not statistically independent of the flow velocity. Thus, the flow statistics are not uniformly sampled and simple averaging of the measurements can be biased. McLaughlin and Tiedermann (1973) and Edwards (1987) state that this bias is on the order of the square of the turbulence intensity.

Processing methods that decrease the effect of velocity bias are the McLaughlin and Tiedermann correction, the residence time weighting correction and the rate measurement correction. In multi-dimension analysis, the first can increase the error over that obtained with no correction. The mean particle velocity is weighted by the particle transit or residence time.

As discussed earlier, fringe bias or angle bias is an error that is eliminated by the frequency shift. The biasing occurs when the signal processor requires a minimum number of cycles to calculate a velocity and some particles fail to provide this number. When the particle velocity is parallel to the fringes so that no particles cross a fringe, the effect is maximized. The effect also occurs when particles passing through the measurement volume center cross enough fringes but those passing through the edges do not. The data rate is greatest when the particle velocity is perpendicular to the fringes and the data rate decreases as the angle between the velocity and fringes approach zero. The resulting velocity is biased toward samples from the perpendicular velocities. By

applying a frequency shift, moving fringes with respect to the fluid are added to the Doppler burst. With a fringe velocity greater than the flow velocity, particles moving parallel to the fringes pass the minimum number of fringes for a measurement.

The gradient bias results from a mean gradient in the probe volume. Since the size of the probe volume is finite, several velocities can be present at any time. This bias depends on the fluid flow and the measurement volume dimensions. It is not caused by individual particle velocity fluctuations in the probe volume. The gradient bias only effects the mean velocity and odd order moments such as skewness.

2.3. Hot wire anemometer technique

The hot wire anemometer technique is based on the principle of convective heat transfer from a sensor in a fluid flow. A change in the flow velocity affecting the sensor temperature is detected almost instantaneously. The following discussion is based on Hinze (1975) and Bruun (1995).

As shown in Figure 2.8, the constant temperature anemometer is a bridge and amplifier circuit that controls a single wire probe at constant temperature. As air flows over the heated wire, the amplifier senses that the bridge is off-balance and adjusts the voltage to the top of the bridge, maintaining the bridge in balance. The voltage is then related to the velocity of the flow through a calibration equation. A built in thermocouple circuit measures the fluid temperature. Since the bridge voltage is sensitive to the fluid temperature as well as the velocity, data reduction software uses the temperature reading to minimize the effect of temperature on the results.

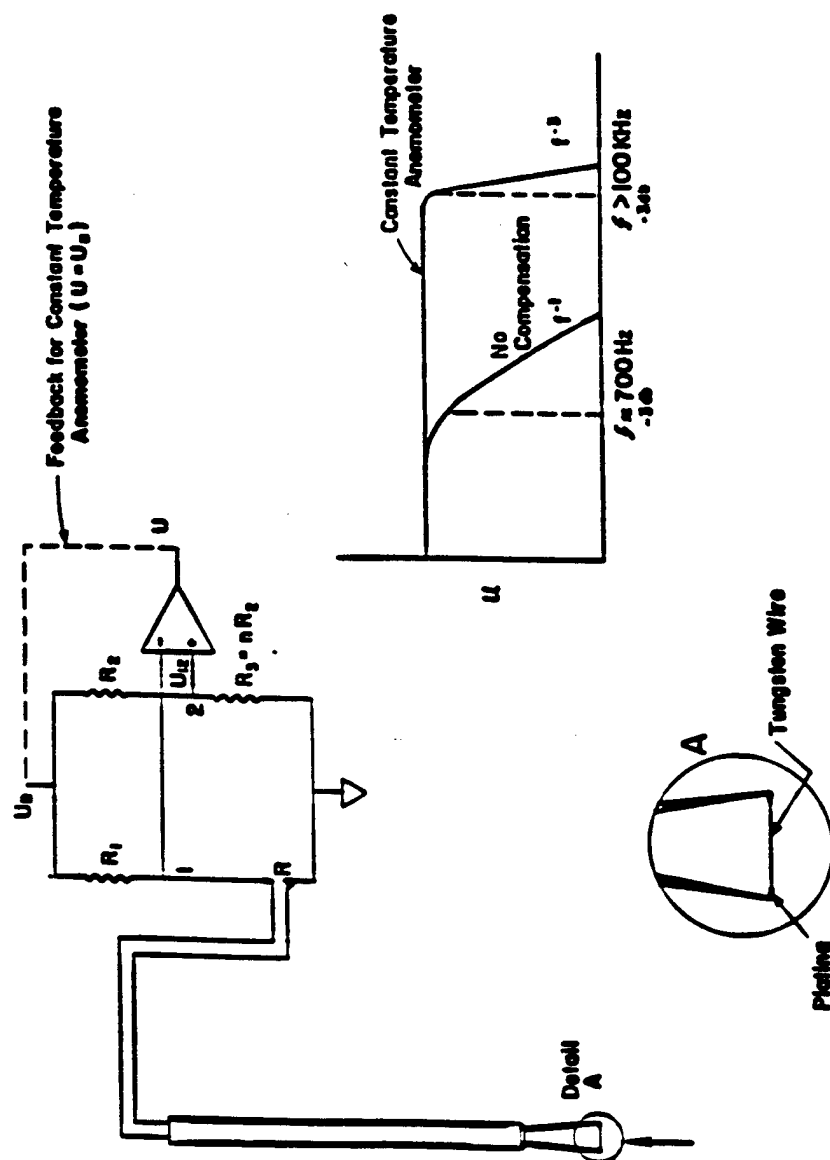


Figure 2.8 Schematic of constant temperature anemometer system from Fingerson (1983).

The boundary layer probe shown in Figure 2.9 was used to measure the velocity in the boundary layer. Table 2.3 lists the boundary layer hot wire characteristics. The wire sensor is made of tungsten with a platinum coating. Minimizing flow disturbances by the larger diameter probe support, the curved support is placed in the flow and oriented upstream.

2.4. Instrumentation

A pitot probe was positioned at the centerline of the test section at 1.5 m from the horizontal surface leading edge. It monitored the free stream velocity during each experiment. The probe was attached to a Validyne model DP103, diaphragm type, pressure transducer and digital display with a maximum pressure range of 0-137 Pa.

2.4.1. LDV

Two and three-component coincident velocity measurements were obtained using a TSI three-component LDV system. The system consists of a Coherent Innova 70, five Watt argon-ion laser, a TSI Colorburst Model 9021 Multicolor Beam Separator, a single-component and two component fiber optic probe, a TSI Colorlink Plus Multicolor Receiver, a TSI IFA 655 Digital Burst Correlator Signal Processor and TSI Find for Windows software.

The argon-ion laser is the coherent light source providing a continuous wave beam for the three wavelengths of light. The laser has a long term power stability in the continuous current regulation mode of $\pm 3\%$ and was typically powered at 3 W. The

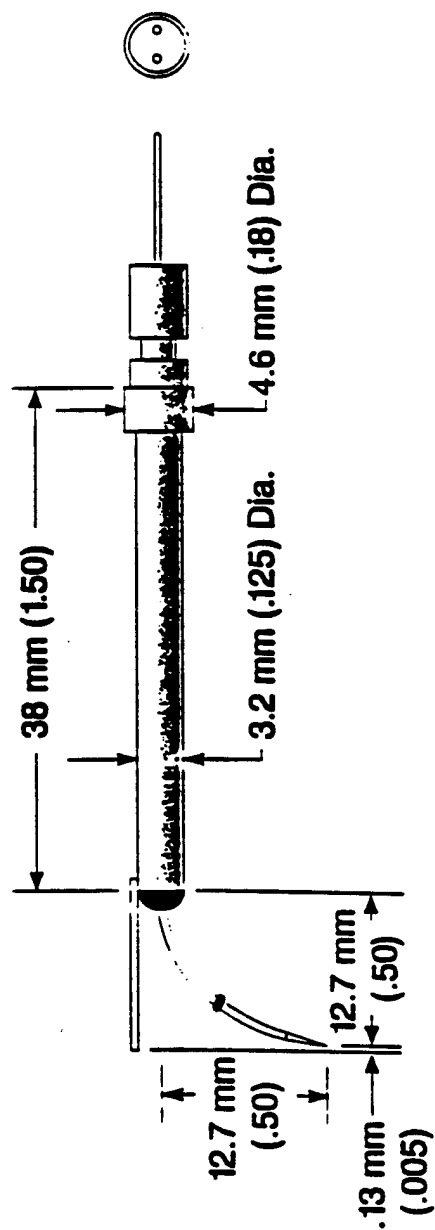


Figure 2.9 A Model 1218 boundary layer probe by TSI Inc.

optical noise level in this mode is 0.5 % RMS. The laser aperture, which controls the laser's transverse mode structure and beam quality, was set at 3 or 4.

From the laser, the multi-colored light passes to the TSI Colorburst Model 9021 Multicolor Beam Separator, which splits the laser beam into wavelengths of 476.5 nm (violet), 488 nm (blue) and 514.5 nm (green). The Colorlink Plus Multicolor Receiver provides the 40 MHz signal to drive the acousto-optic cell in the Colorburst Multicolor Beam Separator.

The acousto-optic cell, or Bragg cell, acts as the beam splitter and adds the 40 MHz frequency shift to one beam in each color pair. The frequency shift for the green and blue beam pairs was set at 5 MHz and at 2 MHz for the violet beam pair.

The shifted and unshifted beams are coupled to fiber optic cables with a typical efficiency of 55 %. The efficiency is a function of the alignment of the beam with the fiber optic inlet. According to Hecht (1990), intermodal dispersion is the effect of light rays arriving at the exit at different times due to varying paths within the fiber. It will occur if the fiber optic cable entrance is too wide and the fiber refractive index is not graduated to force the rays to remain together. To decrease intermodal dispersion, the fiber optic inlet is less than 10 μm and limits the rays to travel along the central axis of the probe.

The two fiber optic probes focus the light from each pair of beams to form a measurement volume or probe volume. A receiving fiber in the two-component probe collects the light scattered by the particles in the probe volume.

This scattered light is sent to the Colorlink Plus Multicolor Receiver. The standard Color Separator was replaced with one prism bar that allowed all light to be collected through one receiving fiber and separated by wavelength. Wavelength separation is accomplished through coated prisms and filters. Here, the light is separated by colors. It is converted into an electrical signal by passing the light through photomultiplier tubes, PMTs. The PMT is a vacuum tube in which electrons are released by light falling on a special photoemissive surface. The current output can be amplified using a chain of intermediate electrodes providing a high frequency response. From the Colorlink, an analog output is sent to the signal processor.

The Doppler signal is processed using a TSI IFA 655 Digital Burst Correlator Signal Processor and TSI Find for Windows software. The signal processor extracts the Doppler frequency information from the input signals and sends it in digital format to the software. It also measures the transit times of the individual bursts.

Two probe configurations were used to collect data. The first configuration as shown in Figure 2.10 was used to measure velocity profiles in the y direction while the second configuration was used to measure velocity profiles in the z direction. To accomplish this, the probe mounting locations in configurations 1 and 2 were exchanged.

In both configurations, the orientation of the two fiber optic probes was such that the violet beam pair measured the axial velocity while the green and blue beam pairs measured the secondary velocities. Light from the green and violet beam pairs was collected in back scatter and light from the blue beam pair in side scatter.

The TSI optical specifications for configurations 1 and 2 are listed in Table 2.2. For the green, blue and violet beam pairs, both configurations produced measurement volumes of $65.3 \mu\text{m} \times 0.68 \text{ mm}$, $85.8 \mu\text{m} \times 0.65 \text{ mm}$, and $60.5 \mu\text{m} \times 0.63 \text{ mm}$, respectively. In wall units, the measurement volumes are 2.5×26 , 2.3×25 , and 2.3×24 , respectively.

Table 2.2 LDV optical specifications.

Beam Color	Green	Blue	Violet
Wavelength (nm)	514.5	488	476
Probe Beam Diameter (mm)	2.82	2.82	2.82
Probe Beam Spacing (mm)	50.0	50.0	50.0
Lens Focal Distance (mm)	250.0	349.7	250.0
Lens Focal Length (mm)	261.3	362.6	261.3
Lens Diameter (mm)	61.5	61.5	61.5
Beam Half Angle (K)	2.76	3.95	5.52
Meas. Vol. Diam. (mic)	65.3	85.8	60.5
Meas. Vol. Length (mm)	0.68	1.24	0.63
Fringe Spacing (mic)	2.69	3.54	2.49
Number of Fringes	12.2	24.2	24.3

Depending on the number of components collected, the coincident mode of operation enforces temporal coincidence between the two or three velocity channels. The Doppler bursts from the channels must fall within a prescribed time window. The window size is a ratio of the probe volume diameter and the mean velocity as follows:

$$\text{Coincidence window size} = \frac{\text{Probe Volume Diameter}}{\text{Magnitude of Local Mean Velocity}} \quad (2.13)$$

The magnitude of the mean velocity is used to ensure that a particle has ample time to pass through the probe volume. Coincident data was collected using coincident windows ranging from 30 μs near the wall to 5 μs in the free stream. The theoretical coincidence windows ranged from 300 μs near the wall to 5 μs in the free stream.

To filter the data, the signal to noise ratio, SNR, in both configurations was set at high. The high setting is defined as the SNR value that a counter type processor can process without producing any erroneous measurement points. Changing the setting from high to medium allows more noise into the measurement.

To allow access into the corner, the vertical LDV probe beam pair was tilted and the horizontal beam pair was tilted to allow measurement closer to the surface. Following the methods as outlined in Kreyszig (1983), the coordinate transformation for the velocity from the violet beam pair is,

$$\tilde{u}_{\text{new}} = \tilde{u} \times \cos \beta \quad (2.14)$$

where β is the angle between the probe axis and the orthogonal axis. The single probe measured the cross-stream velocity and was tilted by 4° to allow access into the corner. Its effect on the mean velocity and turbulence intensity is to reduce the calculated results by 0.2%. For the other beam pairs, the offset angle between the orthogonal coordinates and the probe central axis was 1° .

As shown in Figure 2.10, the probe volume location in the wall normal direction was controlled using a personal computer and a Velmex NF-90 stepper

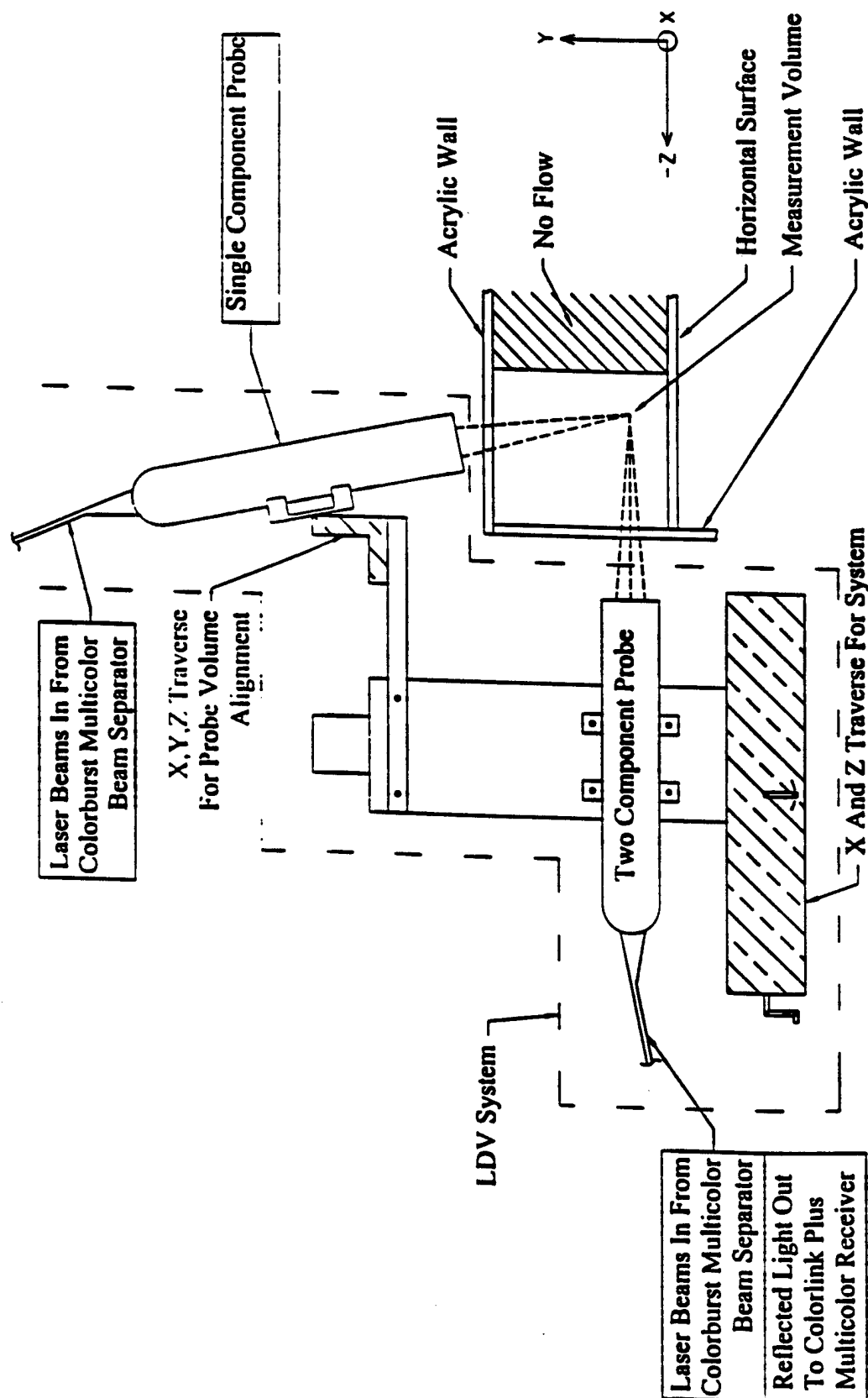


Figure 2.10 Three-component LDV system in dual beam mode with green and violet beam pairs in back scatter mode and blue beam pair in side scatter mode.

motor controller with a resolution of $1.6\text{ }\mu\text{m}$. The manual cross-stream traverse unit had a resolution of $25.4\text{ }\mu\text{m}$.

For experiments with the smooth test surface, three tubes spanned the upstream section of the wind tunnel. The tubes allowed seed for LDV measurements to enter the flow just downstream of the multiple screens and just upstream of the contraction. To evaluate the effect on the flow, the tubes were removed and a boundary layer hot wire probe was used to measure the test section centerline velocity profile at $X = 0.66\text{ m}$. The mean velocity profiles in outer variables show that the tubes have a negligible effect on the flow. The turbulence intensity for profiles with and without tubes shows a slight elevation in the outer region of the boundary layer.

2.4.2. Hot wire

The constant temperature anemometer system manufactured by TSI was used with a single wire boundary layer probe. The probe was placed perpendicular to the flow measuring the axial component of velocity and its fluctuations. A thermocouple was placed downstream of the probe in the flow to measure the temperature. The calibration curve is shown in Figure 2.11. There was a less than 1% difference between the pitot probe-pressure transducer reading and hot wire system. For signal analysis, the TSI IFA-300 with temperature compensation was used.

The boundary layer probe is a TSI Model 1218-T1.5 hot wire sensor. The sensor is made of tungsten with a platinum coating. The probe characteristics are listed in Table 2.3.

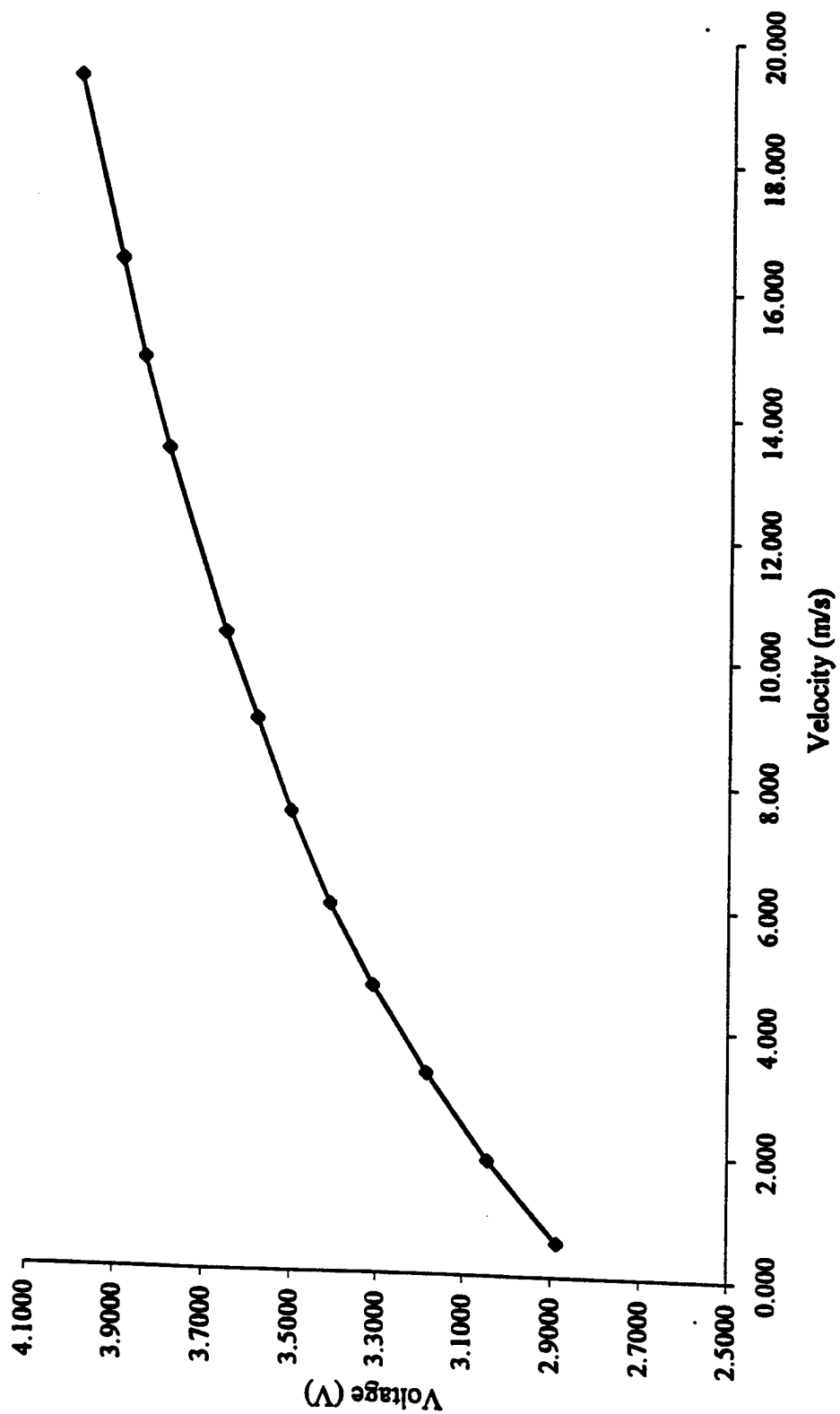


Figure 2.11 Calibration curve of the mean velocity versus voltage for the boundary layer hot wire probe.

Table 2.3 Boundary layer hot wire characteristics.

Diameter of sensing area width	3.8 μm (0.14 wall units)
Length of sensing area	1.27 mm (48 wall units)
Distance between supports	1.52 mm (57 wall units)
Maximum ambient temperature	150 C
Maximum sensing operating temperature	300 C
Temperature coefficient of resistance	0.0042 /C

Chapter 3

Data reduction

3.1. Velocity statistics

Data reduction routines for the time averaged velocity statistics were developed for this investigation. To determine the minimum sample size for statistical convergence, fifty thousand LDV ensembles were collected for statistical analysis of two-dimensional velocity measurements at $y^+ = 9$ and three-dimensional velocity measurements at $y^+ = 50$. The large data set was analyzed to determine any bias resulting from the data set size. The minimum data set size for statistical convergence of the third moment was ten thousand ensembles.

The instantaneous velocities in the x, y, and z directions are \tilde{u} , \tilde{v} , and \tilde{w} , respectively, and are separated into mean components, U, V, and W, and fluctuating components, u, v, and w, as indicated in equation 3.1 below,

$$\tilde{u} = U + u \quad (3.1)$$

To compute the mean velocity, u_{rms} , and Reynolds shear stress, the following relations were used:

$$\text{Mean velocity } U = \frac{\sum \tilde{u} \tau}{\sum \tau} \quad (3.2)$$

$$u_{rms} = \sqrt{\left(\frac{\sum \tilde{u}^2 \tau}{\sum \tau} - \bar{\tilde{u}}^2 \right)} \quad (3.3)$$

$$\text{Reynolds shear stress } \overline{u_i u_j} = \frac{\sum_{i=1}^N u_i u_j}{N} \quad (3.4)$$

where τ is the burst or residence transit time. Edwards (1987) and Drain (1988) recommend correcting for velocity bias using the burst transit time or residence time of a particle through the measurement volume. By setting the residence transit time to one, equations 3.2 - 3.4 revert to the standard equations for mean velocity and u_{rms} .

The sources of statistical bias considered are the gradient bias, angle bias and velocity bias as discussed in Edwards (1987) and Drain (1988). Setting the effective fringe velocity to twice the maximum Doppler shift provides a uniform angular response minimizing angle bias. The mean velocity bias is on the order of the square of the turbulence intensity. The axial turbulence intensity in a boundary layer is shown in Figure 3.1. In Chapter 4, the mean velocity and rms profiles use velocity bias corrected data.

For the smooth test surface, the friction velocity, u_* , is estimated using the measured data in the velocity profiles. As listed in Table 3.1, the friction velocity along the centerline of the smooth test surface was estimated using Coles equation for the interval $30 < y^+ < 300$, the logarithmic law over the same interval and the viscous sublayer for $3 < y^+ < 7$. The sublayer equation is,

$$u^+ = y^+ \quad (3.5)$$

Coles equation from White (1974) is,

$$u^+ = \frac{1}{\kappa} \ln(y^+) + C_o + \frac{\Pi}{\kappa} W(y/\delta) \quad (3.6)$$

where κ and C_o are Spalding's values, Π is a wake parameter and W is a wake function.

For the wake parameter in a zero pressure gradient turbulent boundary layer, Coles suggests the value of 0.55. The wake function is:

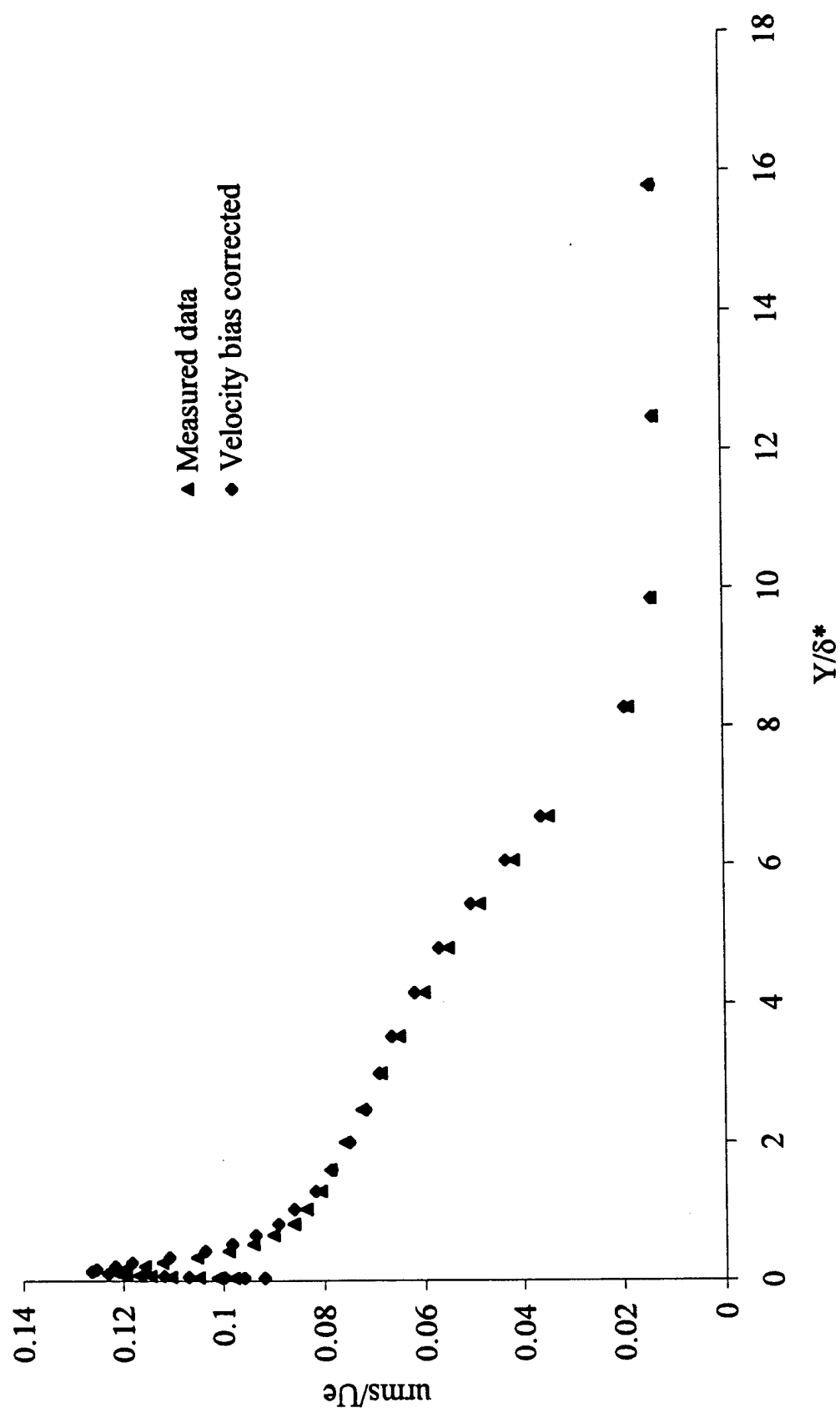


Figure 3.1 The axial turbulence intensity at $X = 1.02$ m comparing the measured data and velocity bias corrected data.

$$W(y/\delta) = 2 \sin^2 \left(\frac{\pi y}{2\delta} \right) \quad (3.7)$$

where the boundary layer thickness, δ , is estimated using equation (3.11). In the logarithmic law, the constants are $\kappa = 0.41$ and $C_o = 5$. For the viscous sublayer calculation, the near wall data was corrected for velocity bias. The average friction velocity from the viscous sublayer and the logarithmic law calculations agree within 5% of the result from Coles equation. The number of data points for an average ranged from five to fifteen, with the exception of the sublayer calculation at $X = 1.02$ m, which had one point. In Chapter 4, the friction velocity from the logarithmic law is used.

Table 3.1 Comparison of methods for calculating the friction velocity along the centerline of the smooth test surface.

X (m)	Offset		Friction Velocity		
	(m)	Wall units	Log Law	Viscous sublayer	Coles
0.41	0.00004	1.6	0.60	0.55	0.57
0.66	0.00007	2.5	0.58	0.58	0.57
1.02	0.00008	3.0	0.57	0.48	0.54
1.37	0.00005	1.7	0.54	0.47	0.51

For the rough test surface, the friction velocity was estimated using the skin friction coefficient equation in Chapter 1 (eqn 1.4, repeated below.) In White (1974) the skin friction coefficient for the fully rough regime is related to Re_x and k/x as follows,

$$\text{Re}_x = 1.73125(1 + 0.3k^+) \exp\left(0.4 \sqrt{\frac{2}{C_f}}\right) x$$

$$\left(\left(0.4 \sqrt{\frac{2}{C_f}}\right)^2 - 4 \left(0.4 \sqrt{\frac{2}{C_f}}\right) + 6 - \frac{0.3k^+}{1 + 0.3k^+} \left(0.4 \sqrt{\frac{2}{C_f}} - 1\right) \right) \quad (3.8)$$

This formula is valid for $(x/k) > 100$. C_f increases on a rough surface relative to a smooth surface.

The ratio of x/k is over 1200 where the axial location includes the virtual origin. Since $k^+ = 65$ using the smooth test surface average friction velocity, it is assumed that the flow regime is fully rough and equation 1.4 is valid. Using the relationship between the friction velocity and the coefficient of friction, this results in a $k^+ \approx 90$, a k^+ in the fully rough regime. For the three-dimensional roughness of Krogstad and Antonia (1999) with an estimated $k^+ = 109$, the coefficient of friction ratio of smooth to rough surface was 0.43. The coefficient of friction ratio for the present research is 0.46.

The friction velocity calculation using the logarithmic layer and the viscous sublayer included a correction for LDV probe volume offset relative to the smooth test surface. The measurement probe volume offsets are listed in Table 3.1. The location correction was the difference between the y^+ based on Spalding's composite law from White (1974) and the y^+ based on the friction velocity calculated from Coles equation around $y^+ \approx 5$. This is less than the probe volume dimension in the wall normal direction. The turbulent boundary layer profile of Spalding's composite law from White (1974) is,

$$y^+ = u^+ + \exp(-\kappa C_o) \left[\exp(\kappa u^+) - 1 - \kappa u^+ - \frac{(\kappa u^+)^2}{2} - \frac{(\kappa u^+)^3}{6} \right] \quad (3.10)$$

where Spalding's preferred values of $\kappa = 0.4$ and $C_0 = 5.5$ were used. In Chapter 4, all data is corrected for the measurement offset.

3.2. Length scales

The length scales examined in this investigation are the boundary layer thickness, displacement thickness, momentum thickness and virtual origin.

The boundary layer thickness, δ , at the centerline of the test section was based on measurements. The integral thicknesses were estimated using numerical integration of the profile data applying the trapezoidal rule. The boundary layer thickness, δ , is defined as the wall normal location where the mean axial velocity is $0.99U_e$. Along with δ , the displacement thickness, δ^* , and momentum thickness, θ , are compared to the results from the empirical formula from White (1974) which follows,

$$\delta, \delta^*, \theta = \frac{C\nu Re_{x_0}^{6/7}}{U_b} \quad (3.11)$$

where x_0 is measured from the virtual origin of the flow and the constant C is 0.14, 0.018, and 0.014 for the boundary layer, displacement and momentum thicknesses, respectively.

We assumed that the coefficients apply for a rough surface, providing an order of magnitude comparison.

The shape factor, H , is the ratio of the displacement thickness to the momentum thickness. An empirical equation for the shape factor is,

$$H = \left[1 - \frac{G}{\left(\frac{2}{C_f} \right)^{1/2}} \right]^{-1} \quad (3.12)$$

where C_f is the coefficient of friction and G is an integral parameter involving Clauser's defect thickness as discussed in White (1974). For a zero pressure gradient, an approximate value for G is 6.51. The relationship for the coefficient of friction and velocity ratio is,

$$\left(\frac{2}{C_f}\right)^{1/2} = \left(\frac{U_e}{u_\tau}\right) \quad (3.13)$$

Substituting equation 3.13 and the value for G into equation 3.12, the new equation for the shape factor is,

$$H = \left[1 - 6.51 \frac{u_\tau}{U_e}\right]^{-1} \quad (3.14)$$

Using the empirical relation of equation 3.14 based on flat plate theory, the shape factor for the smooth test surface was estimated as 1.3 ~ 1.4 and is listed in Table 3.2. For the rough test surface, the shape factor using the measured data at $X = 0.66$ and 1.02 m is 1.45. The length scales for the rough surface are listed in Table 3.3.

Boundary layer virtual origins for the smooth and rough test surfaces were estimated using the evaluated displacement and momentum thicknesses. For a two-dimensional turbulent boundary layer, both integral thicknesses are proportional to the distance from the virtual origin to the $6/7$ power. According to White (1974), the virtual origin can be linearly extrapolated from a plot of the integral thicknesses raised to the $7/6$ power versus streamwise distance from the leading edge. The virtual origin for the smooth surface is 175 mm and for the rough surface is 1500 mm. Figure 3.2 and 3.3 show the plot of the displacement and momentum thicknesses for the smooth and rough test surfaces. For the two-dimensional boundary layer, very good agreement was obtained between the

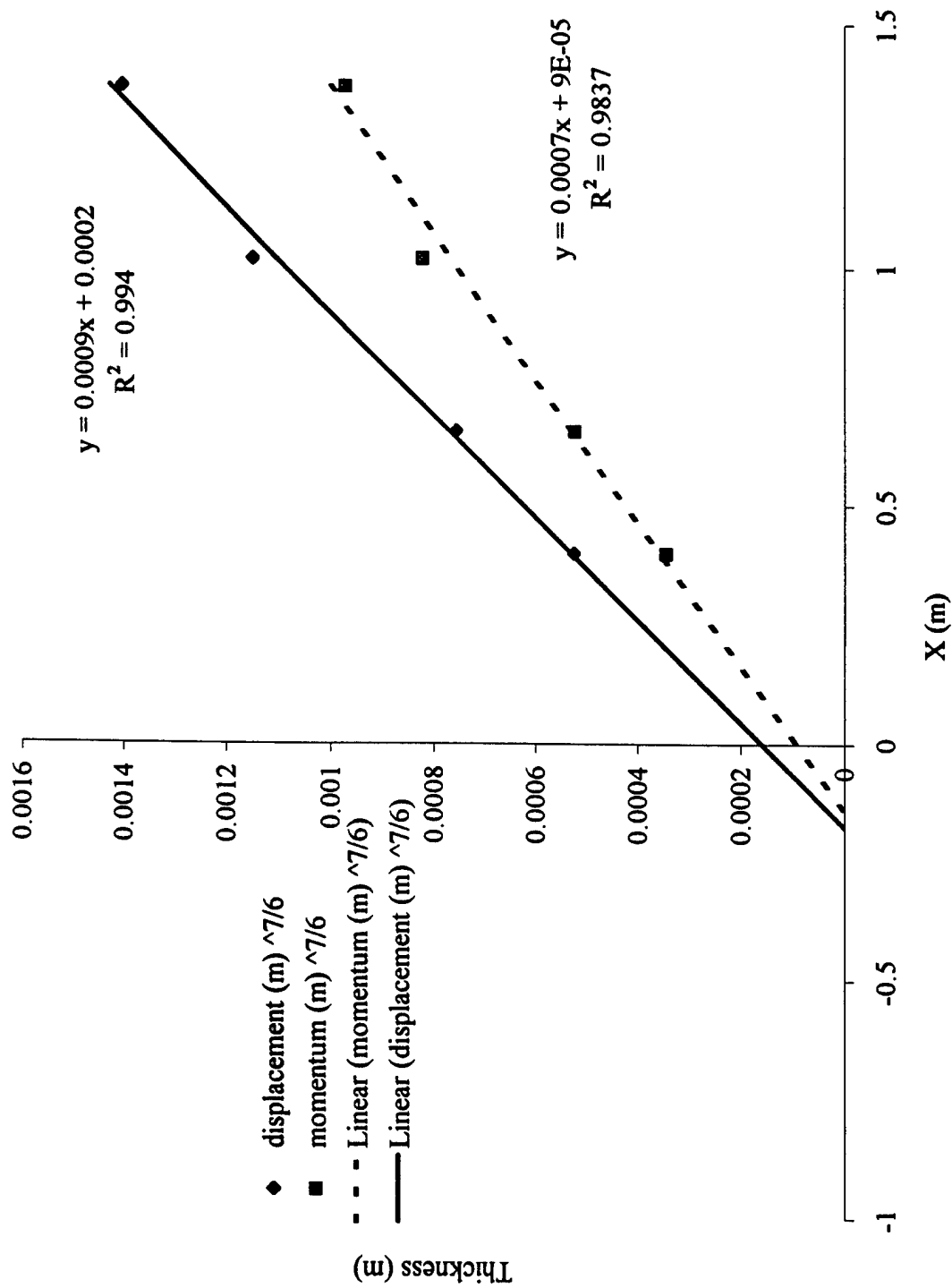


Figure 3.2 Virtual origin as a function of axial location $X^{6/7}$ for the smooth test surface.

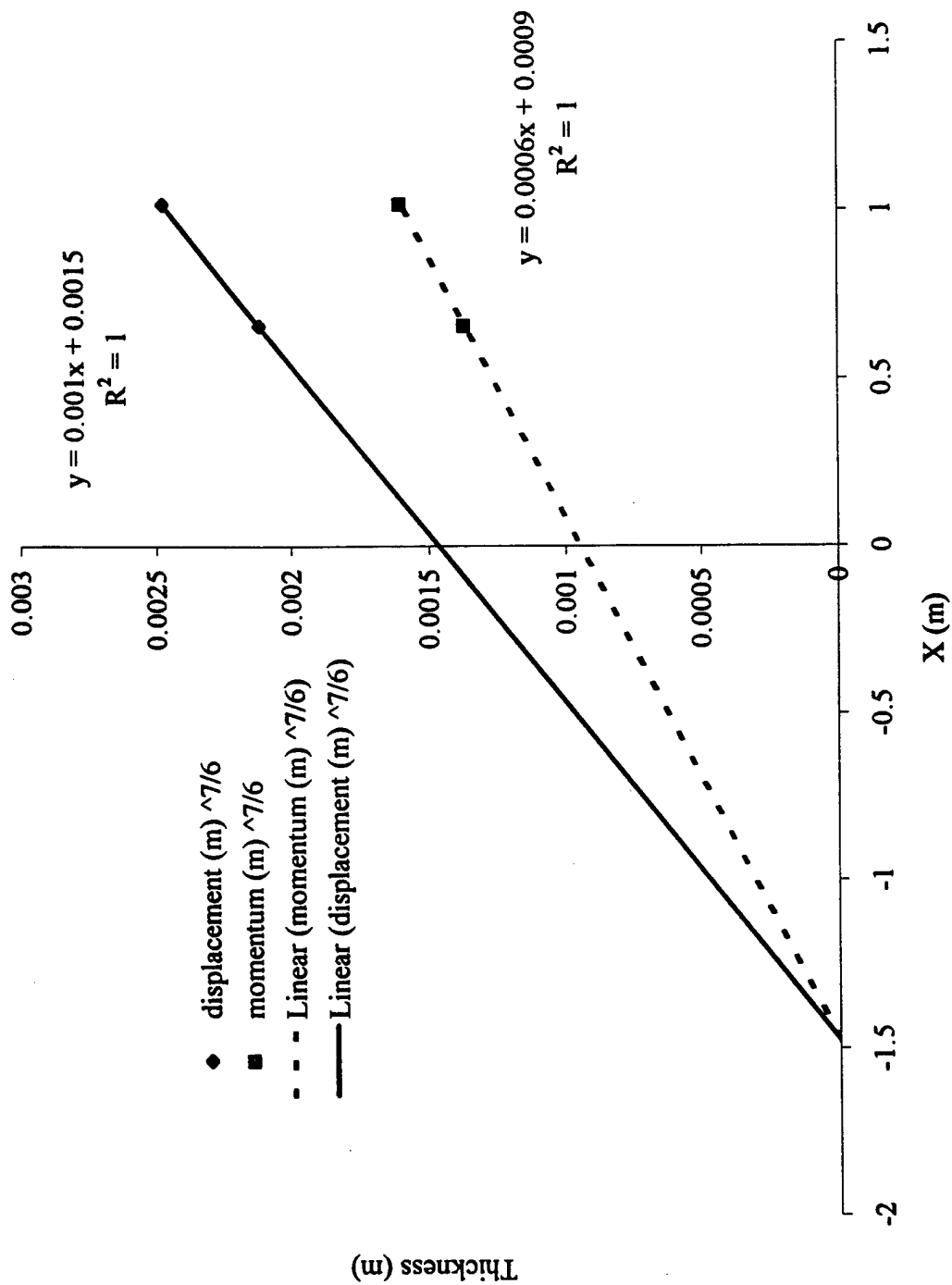


Figure 3.3 Virtual origin as a function of axial location $X^{6/7}$ for the rough test surface.

displacement thickness and momentum thickness calculated as above and those listed in

Table 3.2 calculated using the virtual origin and the empirical formulas of flat plate theory in equation 3.11.

Table 3.2 Comparison of the displacement and momentum thicknesses and shape factors using measured data and flat plate theory for the smooth test surface.

Meas. Loc.	Axial Loc. w/ virtual origin	Measured Data (mm)			Flat Plate Theory (mm)		
X (m)	X _{vo} (m)	δ^*	θ	H	δ^*	θ	H
0.41	0.575	1.5	1.1	1.36	1.6	1.2	1.42
0.66	0.835	2.1	1.5	1.4	2.2	1.7	1.41
1.02	1.195	3	2.3	1.3	3	2.3	1.39
1.37	1.545	3.6	2.6	1.39	3.7	2.9	1.37

Table 3.3 Comparison of the displacement and momentum thicknesses and shape factors using measured data and flat plate theory for the rough test surface.

Meas. Loc.	Axial Loc. w/ virtual origin	Measured Data (mm)			Flat Plate Theory (mm)		
X (m)	X _{vo} (m)	δ^*	θ	H	δ^*	θ	H
0.66	2.16	0.0051	0.0035	1.45	0.0049	0.0038	1.29
1.02	2.52	0.0058	0.0040	1.45	0.0057	0.0044	1.29

Chapter 4 Results

In this chapter, we present the mean velocity profiles, turbulence intensities and Reynolds shear stresses for the corner flows with the smooth and rough test surfaces. The axial velocity is the X coordinate, the wall-normal velocity is the Y coordinate and the cross-stream velocity is the Z coordinate. Recall that the test section has a zero pressure gradient and that the free stream velocity was 13.1 m/s. In Figure 4.1, the axial turbulence intensity measured with the LDV compares well with the measured results from the boundary layer hot wire probe. The measurements are from the centerline of the smooth test surface at $X = 0.66$ m. The velocity profiles were measured normal to the test surface.

The test matrix, Table 4.1, lists the locations where data are collected for the smooth and rough test surfaces. The range of the momentum based Reynolds number

Table 4.1 Experiment test matrix.

Axial Location (m)	Distance from Corner (mm)	
	Smooth Test Surface	Rough Test Surface
0.41	LDV: 101.6	
0.66	Hot Wire: CL LDV: 6.4, 19, 57, 102	LDV: 6.4, 12.7, 14, 19, 25.4, 38.1, 50.8, 102
1.02	LDV: 6.4, 19, 57, 102	LDV: 6.4, 12.7, 14, 19, 25.4, 38.1, 50.8, 102
1.37	LDV: 102	

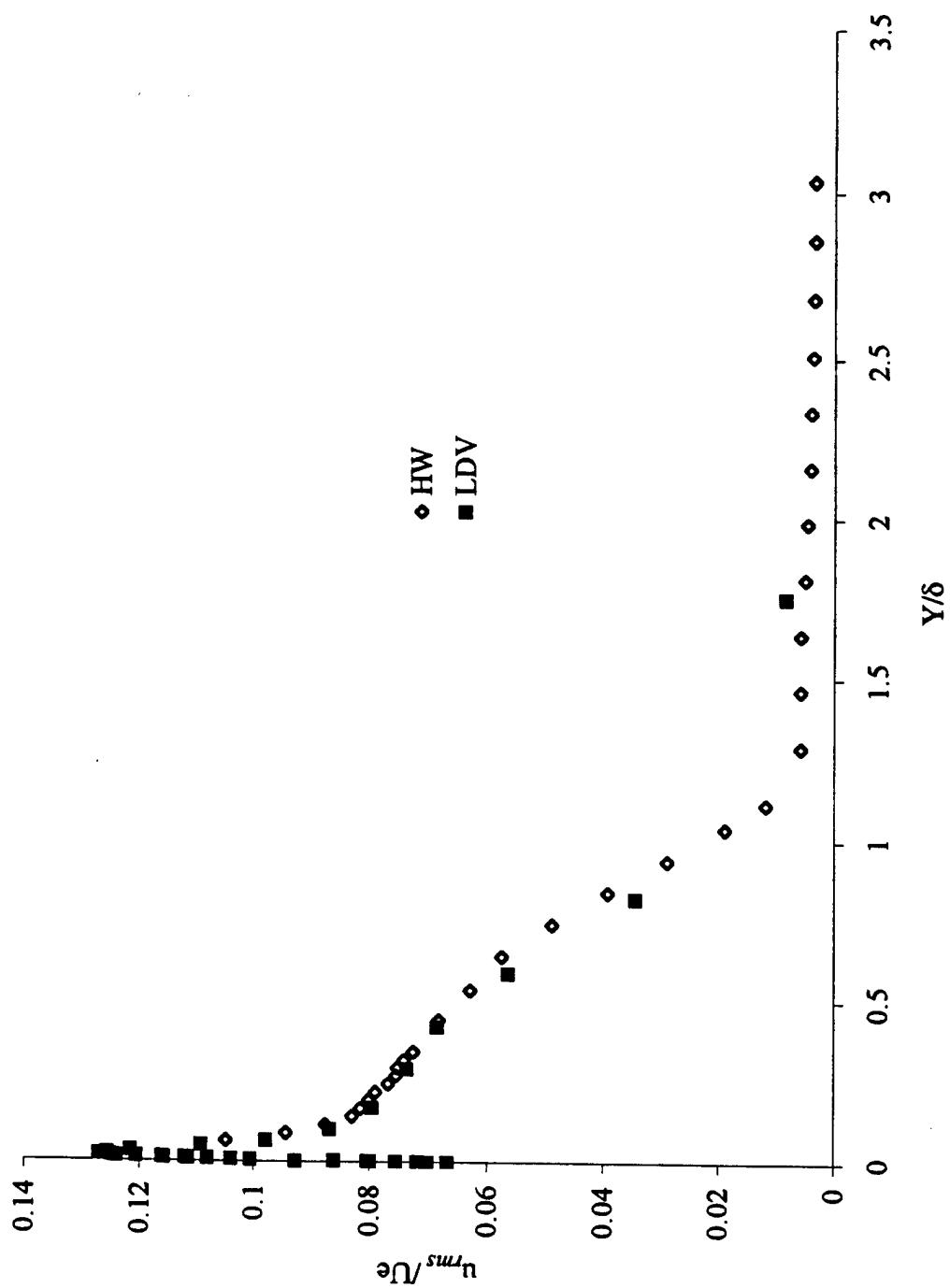


Figure 4.1 Comparison of the axial turbulence intensity measured with the LDV and hot wire probes along the centerline of the smooth test surface at $X = 0.66$ m.

through the smooth surface test section is $1070 < Re_\theta < 2500$. The data are collected at four locations along the test section centerline and at two of the axial locations from the centerline to 6.4 mm from the corner.

4.1. Two-dimensional turbulent boundary layer with smooth test surface

Away from the corner, a two-dimensional boundary layer exists above the smooth test surface. The mean axial velocity profiles normalized by inner variables in Figure 4.2 were in good agreement with the turbulent boundary layer profile of Spalding (1961) through the logarithmic region. Measured wall-normal and cross-stream velocity components were found to be zero. Figure 4.3 shows the mean velocity profiles normalized by the free stream velocity and plotted versus y/δ^* where δ^* is the displacement thickness. Experimental results from Petrie, Fontaine, Sommer and Brungart (1990) at the momentum based Reynolds number, $Re_\theta = 13,540$, are also plotted. The trend is the same between the profiles; the outer region of the measured profiles departs from the profile of Petrie et al. with decreasing Reynolds number. As a test of boundary layer development, the velocity defect is plotted in Figure 4.4; in addition, the direct numerical simulation (DNS) result from Spalart (1988) at $Re_\theta = 1410$ is plotted. Similar trends between the profiles are apparent. The profiles for $Re_\theta = 1070$ and 1475 are in agreement with the DNS results.

The axial turbulence intensity normalized by inner variables is plotted in Figure 4.5. For comparison, the boundary layer data at $Re_\theta = 1750$ of Karlsson and Johansson (1988) is also shown. The measured data is corrected for velocity bias and the profiles

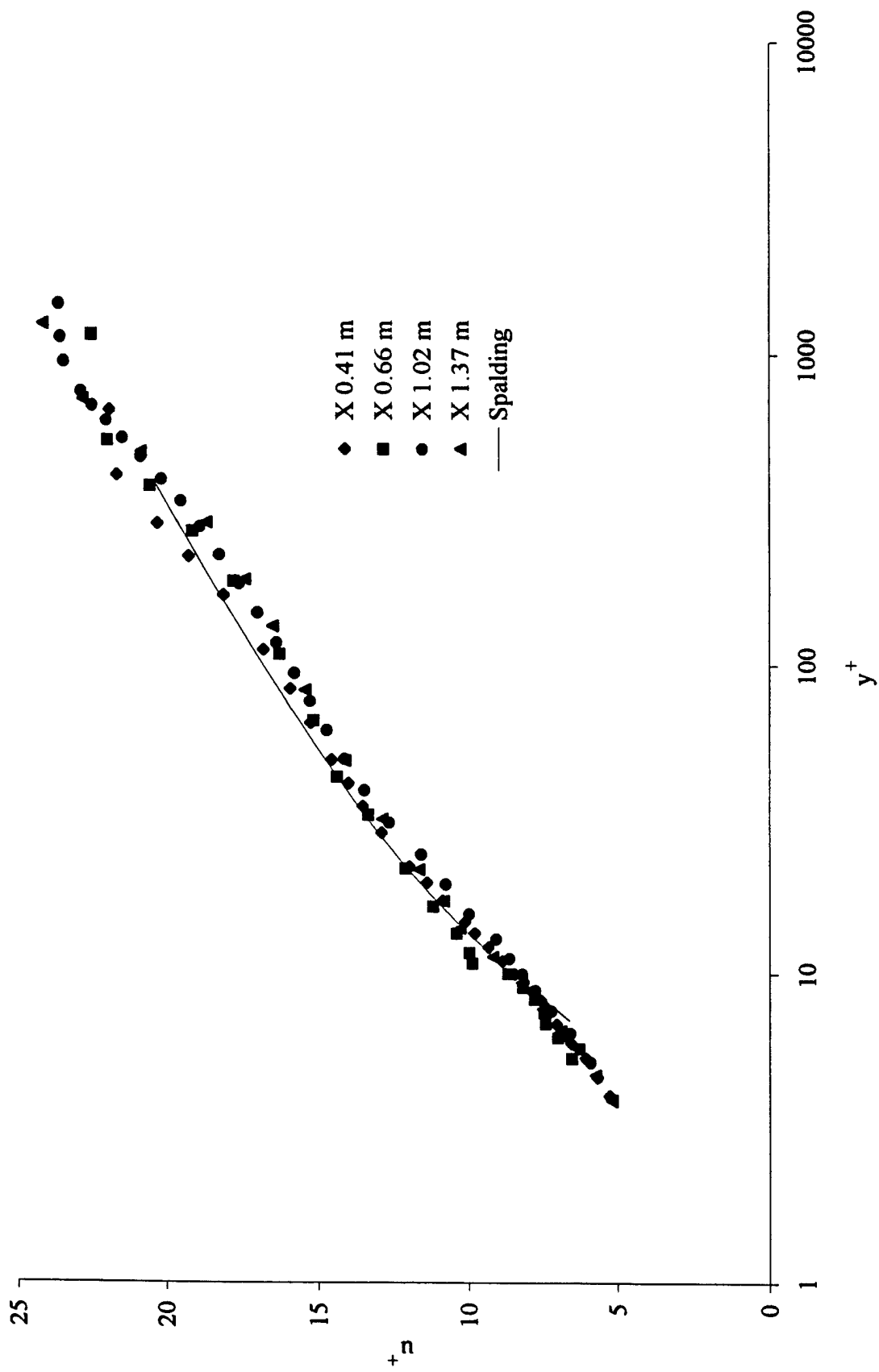


Figure 4.2 Mean axial velocity profiles in inner variables along the centerline of the smooth test surface.

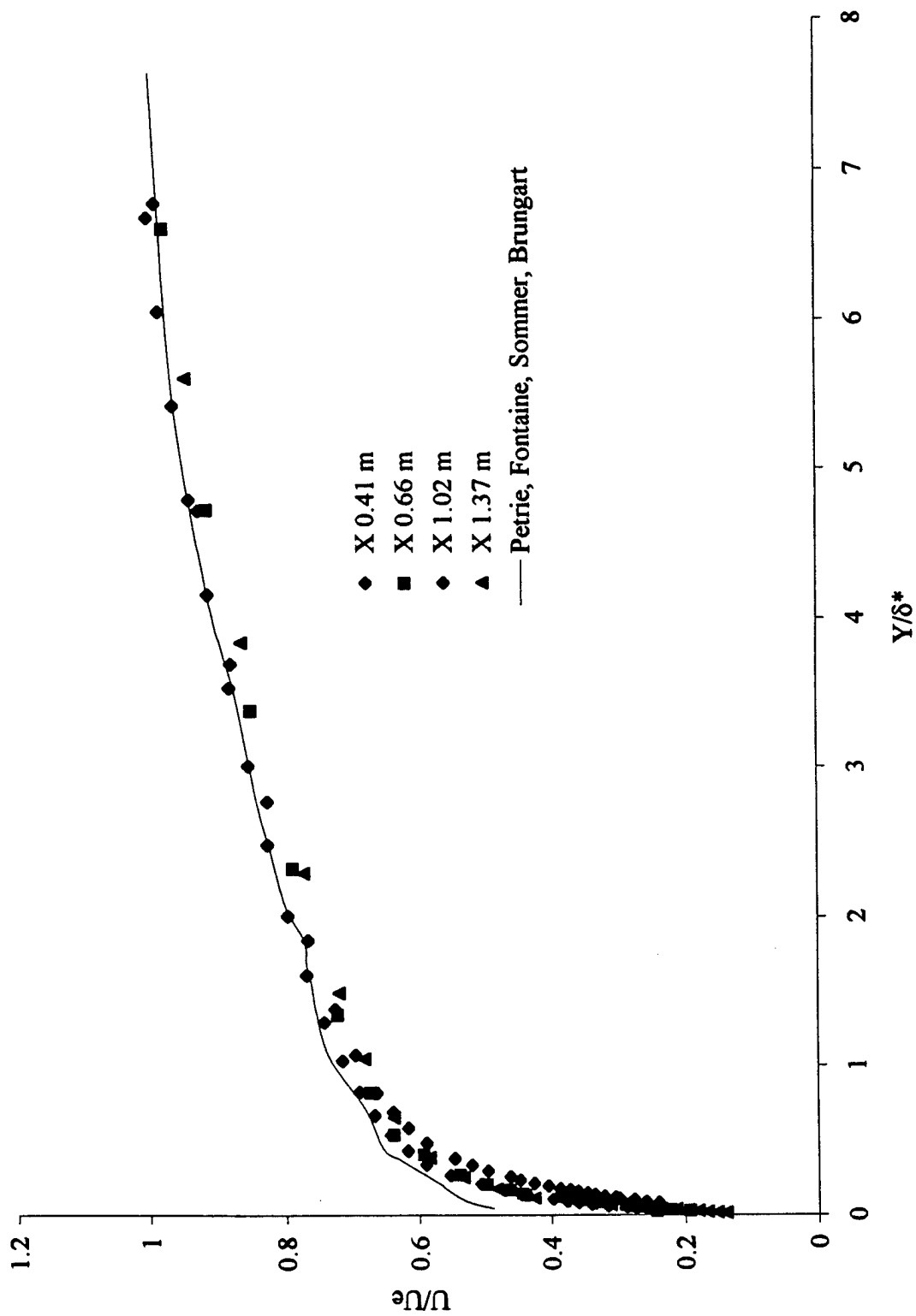


Figure 4.3 A comparison of the mean axial velocity profiles along the centerline of the smooth test surface.

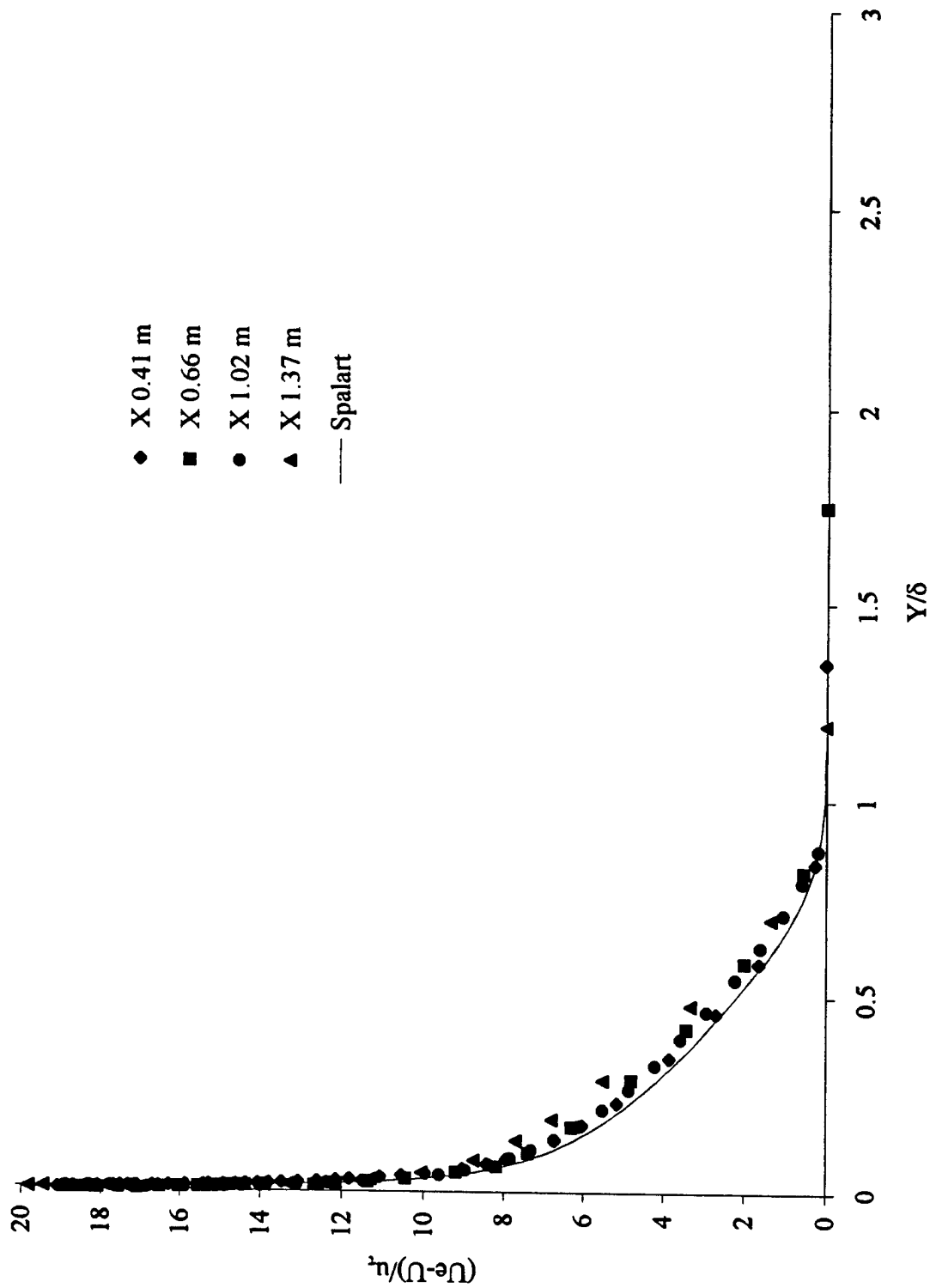


Figure 4.4 The mean axial velocity profiles in the outer part of the turbulent boundary layer along the centerline of the smooth test surface.

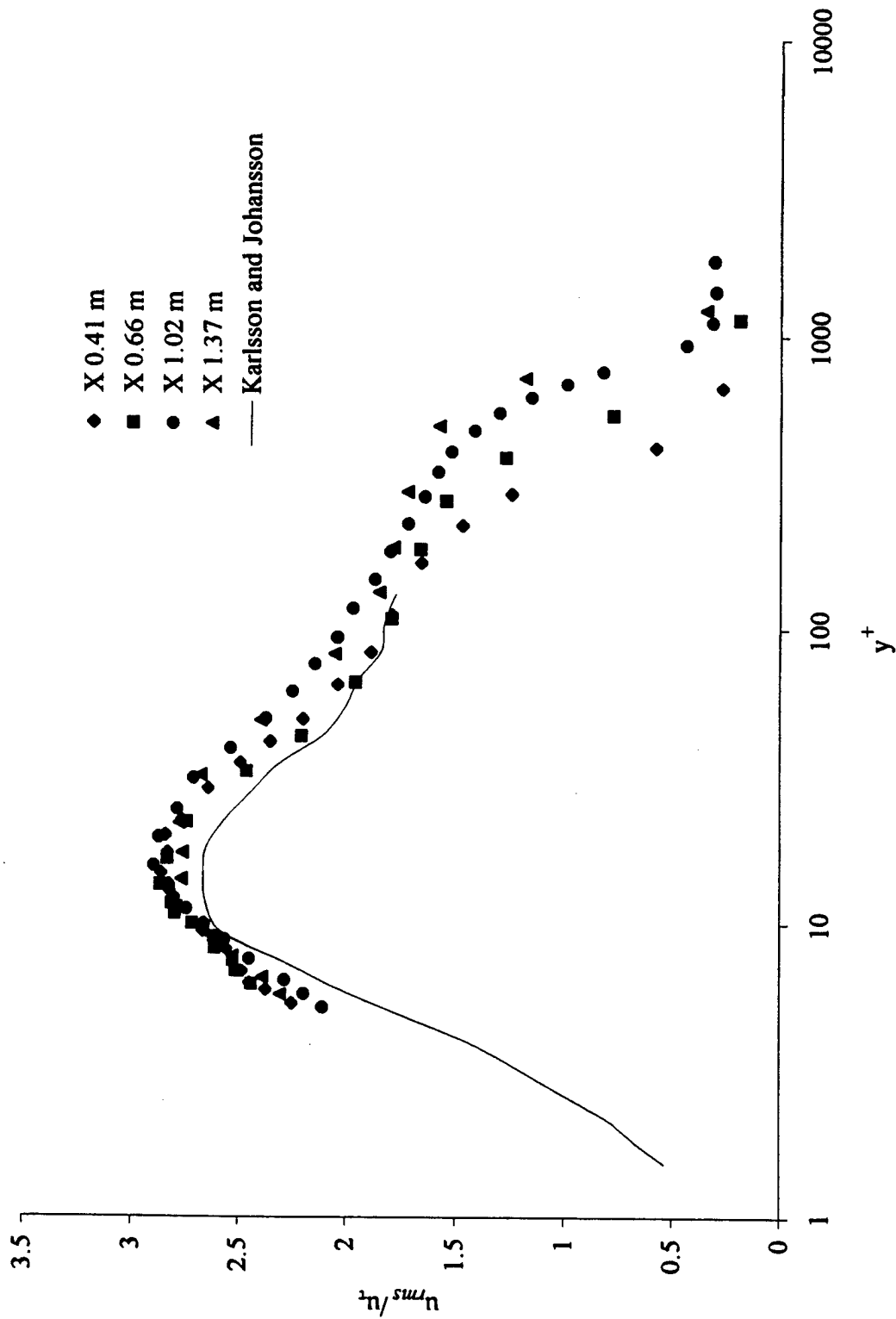


Figure 4.5 The axial turbulence intensity in inner variables along the centerline of the smooth test surface.

follow similar trends. For the inner region of the low Reynolds number flow, the normalized axial turbulence intensity increases with Reynolds number. This agrees with the conclusions of Andreopoulos, Durst, Zaric and Jovanovic (1984) and Ching, Djenidi, and Antonia (1995). The maximum axial turbulence intensities and corresponding y^+ locations are listed in Table 4.2. The peak values of turbulence intensity are slightly elevated compared to the peak value of 2.71 ± 0.14 reported in the survey results of Mochizuki and Nieuwstadt (1996). The corresponding y^+ locations are in good agreement with their average $y^+ = 14.9 \pm 1.31$. Figure 4.6 shows the axial turbulence intensity profiles normalized by the free stream velocity and plotted versus y/δ^* . Through the boundary layer, the measured results follow the trend of the profile at $Re_\theta = 13,540$ from Petrie, Fontaine, Sommer and Brungart (1990).

Table 4.2 Maximum axial turbulence intensity and corresponding y^+ locations.

X (m)	Re_θ	U_{rms}/u_τ	y^+
0.41	1070	2.86	14.8
0.66	1475	2.86	13.6
1.02	2000	2.89	15.7
1.37	2500	2.79	11.4

Profiles of the \overline{uv} Reynolds stress normalized by inner variables are shown in Figure 4.7 along with the results of Karlsson and Johansson at $Re_\theta = 1750$. Good agreement between the trends of the measured data and those of the other researchers is apparent. Again, a Reynolds number effect is evident and the measured data is elevated compared to the profile from Karlsson and Johansson. As the Reynolds number increases,

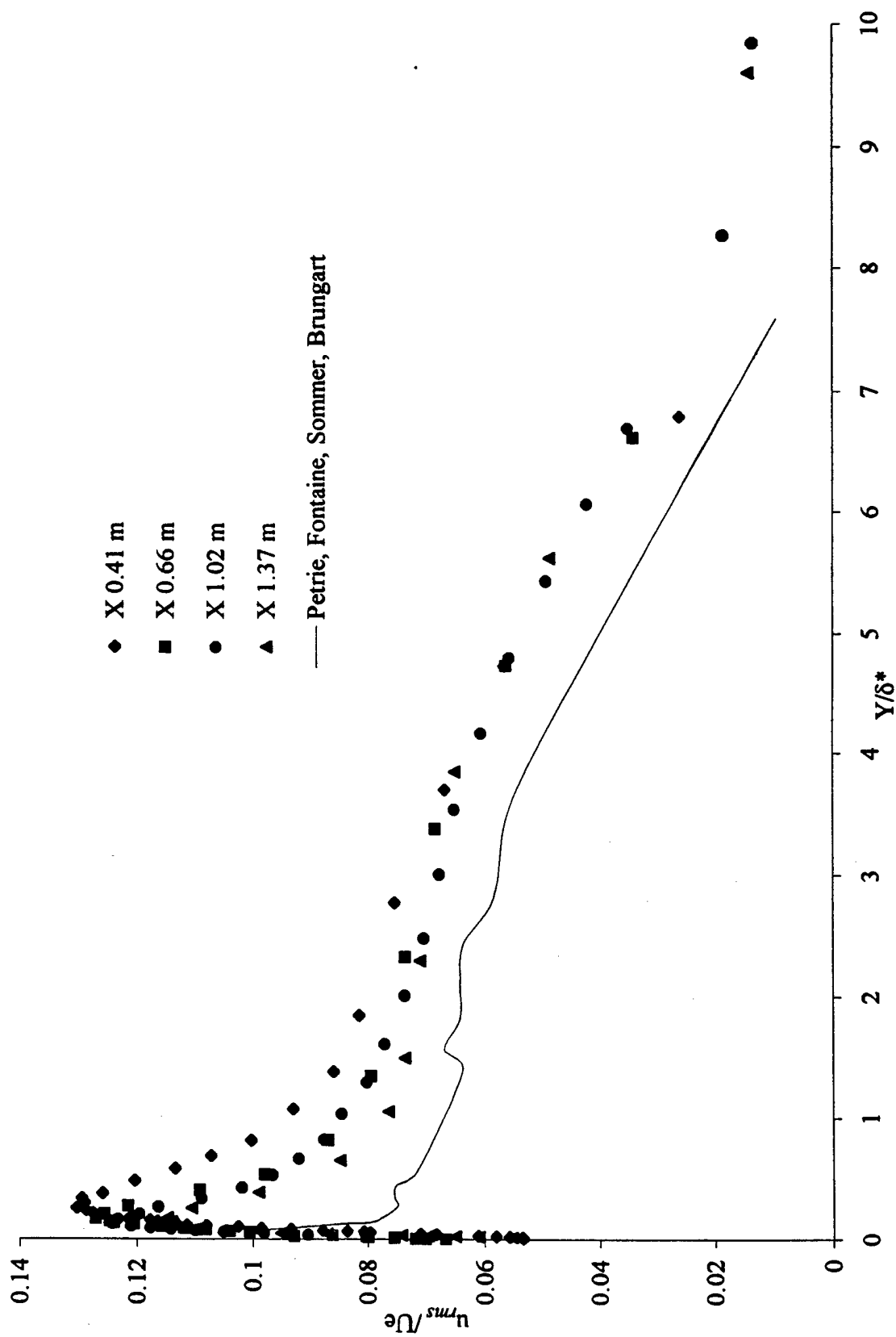


Figure 4.6 The axial turbulence intensity along the centerline of the smooth test surface.

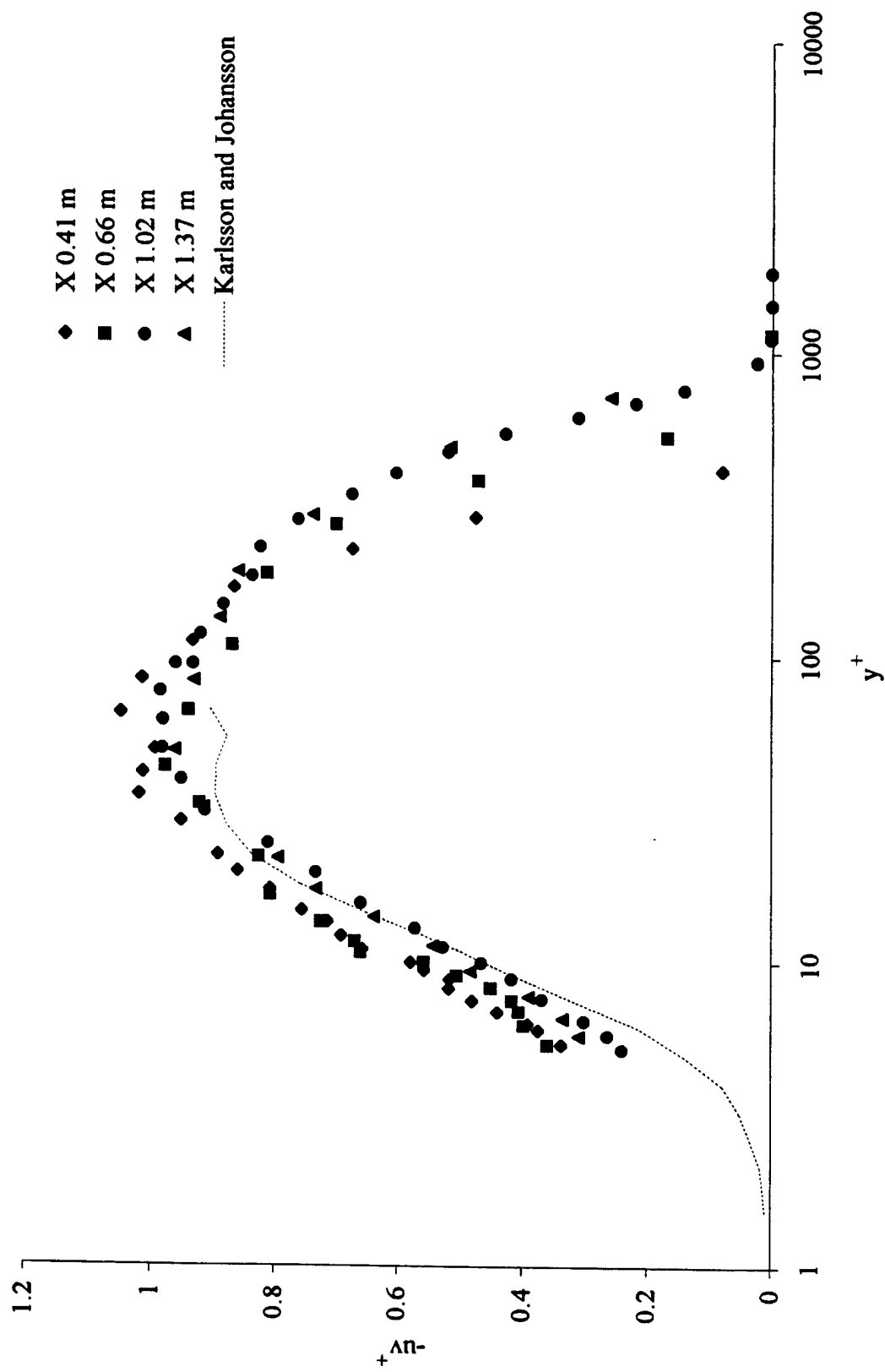


Figure 4.7 The $-uv$ Reynolds shear stress in inner variables along the smooth test surface centerline.

the maximum value of the $-\overline{uv}$ Reynolds shear stress component near the wall decreases. Figure 4.8 presents the $-\overline{uv}$ Reynolds shear stress normalized by the free stream velocity squared and plotted versus y/δ^* . For comparison the experimental results at $Re_\theta = 1003$ and 2788 of Erm and Joubert are shown. As in the previous figures there is a Reynolds number effect for $0.5 < y/\delta^* < 4$.

In summary, the mean velocity, axial turbulence intensity and Reynolds shear stress profiles along the centerline of the smooth test surface compare favorably with previous experimental and computational two-dimensional turbulent boundary layers.

4.2. Three-dimensional turbulent boundary layer with smooth test surface

As the corner is approached, the turbulent boundary layer becomes three-dimensional. Normalizing the measured results with length and velocity scales becomes a problem, since the scales for the inner and outer regions of a two-dimensional boundary layer do not apply to a three-dimensional corner boundary layer.

According to Fleming, Simpson, Cowling, and Devenport (1993), the suggested length scale for the axial velocity component is the smooth test surface thickness. For the test surface wall-normal component, it is the boundary layer thickness just upstream of the junction or leading edge. However, neither length scale collapses their data. In this study, the boundary layer on both the flat plate and the test surface was tripped downstream of the junction. Therefore, for the wall-normal location in the corner flow, we normalized by the local displacement thickness. Except where noted, the velocity components are normalized by the free stream velocity. Profiles of the mean axial velocity, relative secondary velocities, axial turbulence intensity and $-\overline{uv}$ Reynolds shear

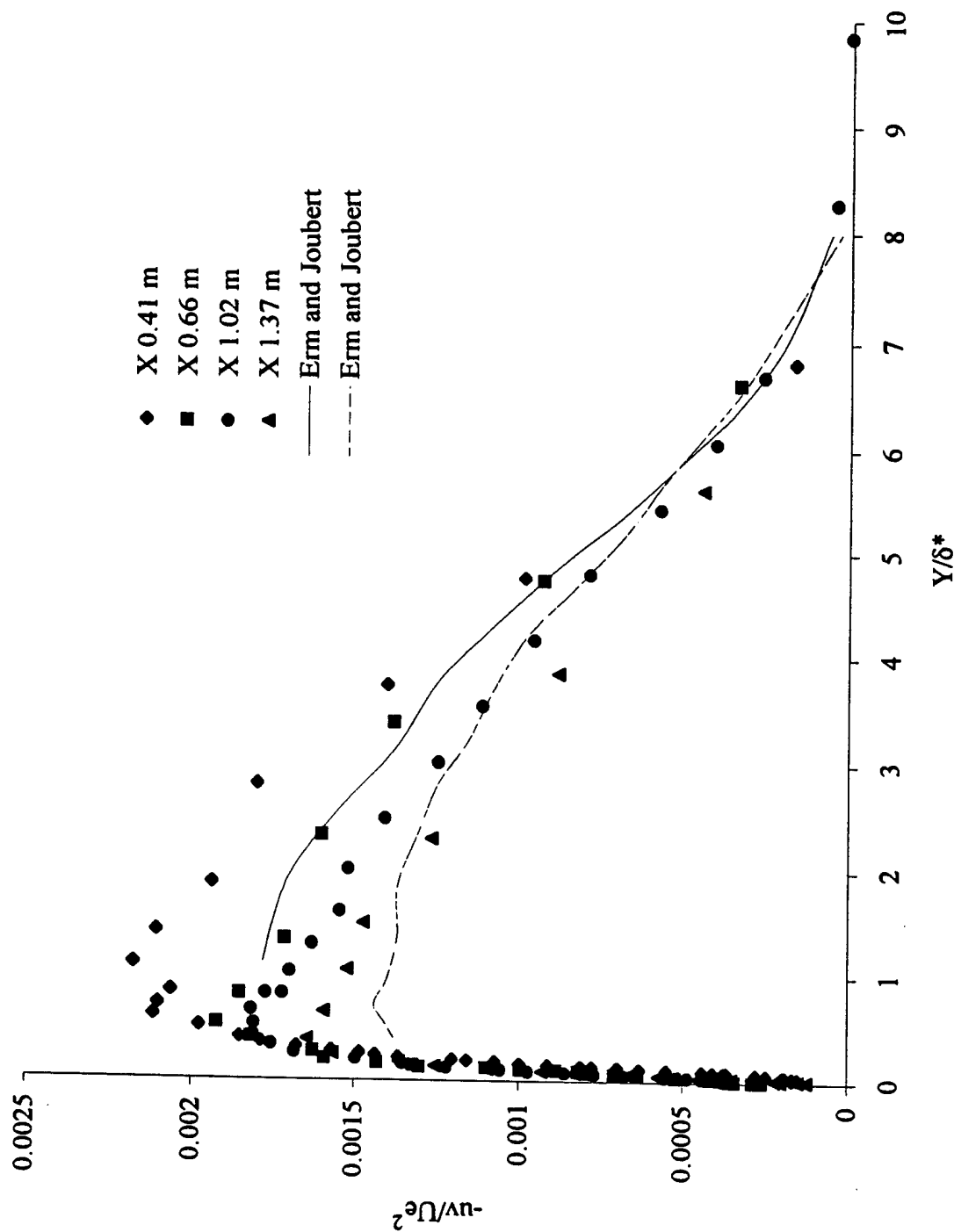


Figure 4.8 The $-uv$ Reynolds shear stress along the centerline of the smooth test surface. For Erm and Joubert data, solid line is $R_\theta = 1003$ and dashed line is $R_\theta = 2788$.

stress are presented. The relative secondary velocity is the absolute value of the local wall-normal or cross-stream velocity to the local axial velocity.

In Figure 4.9, the mean axial velocity profiles at $X = 0.66$ m are shown. As the corner is approached, the profiles depart from the centerline profile at $y/\delta^* \approx 0.3$. The most significant change is observed at $Z = 6.4$ mm; for $y/\delta^* > 2.5$, the mean axial velocity is nearly constant at 0.84 across the measured three-dimensional boundary layer. The mean axial velocity profiles at $X = 1.02$ m are shown in Figure 4.10. As in Figure 4.9, a similar trend occurs; the profiles near the corner depart from the centerline profile at $y/\delta^* \approx 0.2$. Again, the profile with the most significant change is at $Z = 6.4$ mm; it has a more gradual increase and $U/U_e \approx 0.7$ for $y/\delta^* > 2$.

It is interesting to compare the relative secondary velocities in the corner as a function of distance downstream. At $Z = 6.4$ mm and $X = 0.66$ m, the maximum relative wall-normal secondary velocity is 2.5 % at $y/\delta^* \approx 0.1$ and is less than 1% for $y/\delta^* > 6.5$. Further downstream at $X = 1.02$ m, the ratio has increased to 3.8 % at $y/\delta^* \approx 0.2$. At $Z = 6.4$ mm and $X = 0.66$ m, the relative cross-stream secondary velocity is a maximum of 11 % at $y/\delta^* \approx 0.25$. The maximum ratio at $Z = 6.4$ mm and $X = 1.02$ m is 12 % at $y/\delta^* \approx 0.12$, which is the nearest measured cross-stream velocity at this Z location.

Using similar geometries, Shabaka (1979) and McMahon, Hubbartt, and Kubendran (1982) identified a vortex in their corner flow experiments. They also suggested that a second vortex may develop downstream between the earlier vortex and the test surface. Its cause was possibly due to further separation of the flow.

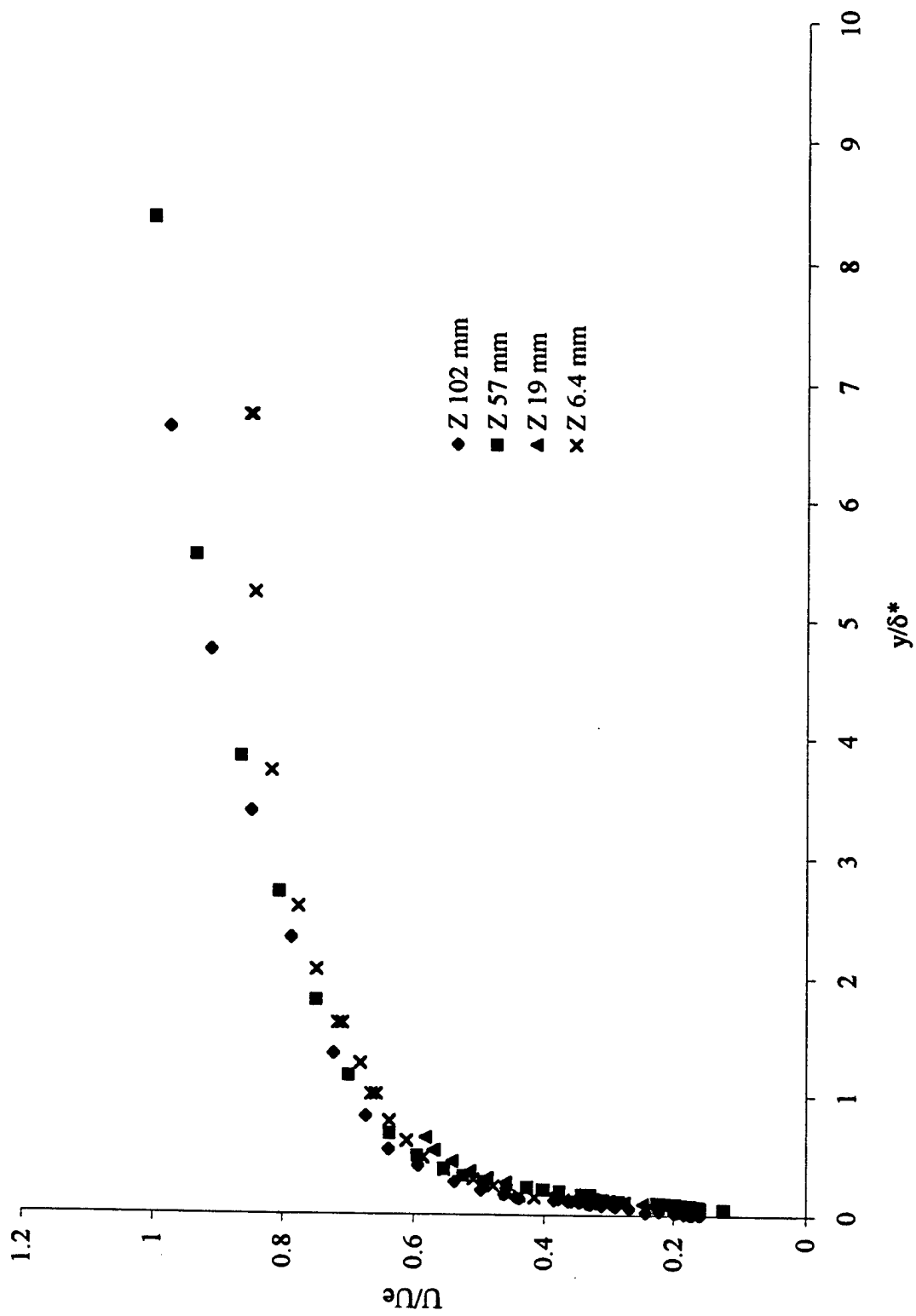


Figure 4.9 Mean axial velocity for the smooth test surface ranging into the corner at $X = 0.66$ m.

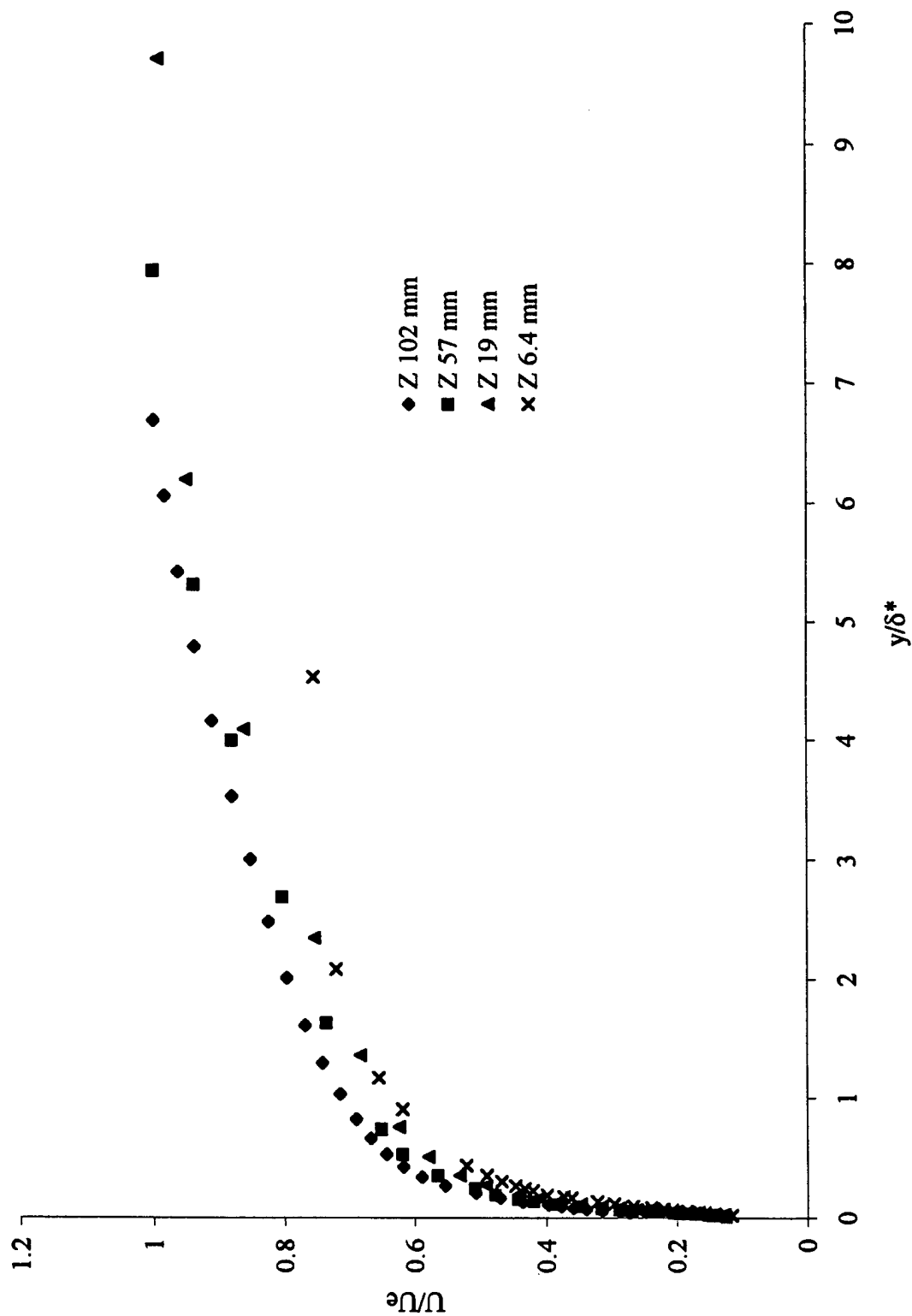


Figure 4.10 Mean axial velocity for the smooth test surface ranging into the corner at $X = 1.02$ m.

The axial turbulence intensities for $X = 0.66$ m and 1.02 m in Figures 4.11 and 4.12 include the two-dimensional profiles at the centerline. For $y/\delta^* > 4$ at $Z = 6.4$ mm, the turbulence intensity departs from the trends of the other profiles and begins to increase. The intensity increases from 0.066 to 0.077, maintaining this with increasing distance from the smooth test surface. Further downstream, the axial turbulence intensities at $X = 1.02$ m in Figure 4.12 depart from the centerline profile at both $Z = 19$ and 6.4 mm. At 6.4 mm, the profile follows a similar trend to the one upstream at this Z location. However, a minimum occurs closer to the test surface.

Profiles of the $-\overline{uv}$ Reynolds shear stress at $X = 0.66$ m are shown in Figure 4.13. The profiles at $Z = 57$ and 19 mm follow the same trend as at the centerline, increasing to a maximum and decreasing to zero as the distance from the test surface increases. At $Z = 6.4$ mm, the stress profile is similar to the centerline profile for $y/\delta^* < 1$. For $1 < y/\delta^*$, the stress decreases at a greater rate than the centerline profile. Similar profiles near the corner were found by Shabaka (1979). At $X = 1.02$ m, the $-\overline{uv}$ Reynolds shear stress profiles for $y/\delta^* < 0.4$ in Figure 4.14 are comparable to those in Figure 4.13. At the centerline and $Z = 57$ mm, the profiles are similar to those upstream at the same Z location. At $Z = 19$ mm, however, the profile reaches a maximum furthest from the test surface and decreases at the slowest rate. The shear stress at $Z = 6.4$ mm decreases at a faster rate than the other profiles. The other Reynolds shear stress components also follow the trends in Shabaka (1979).

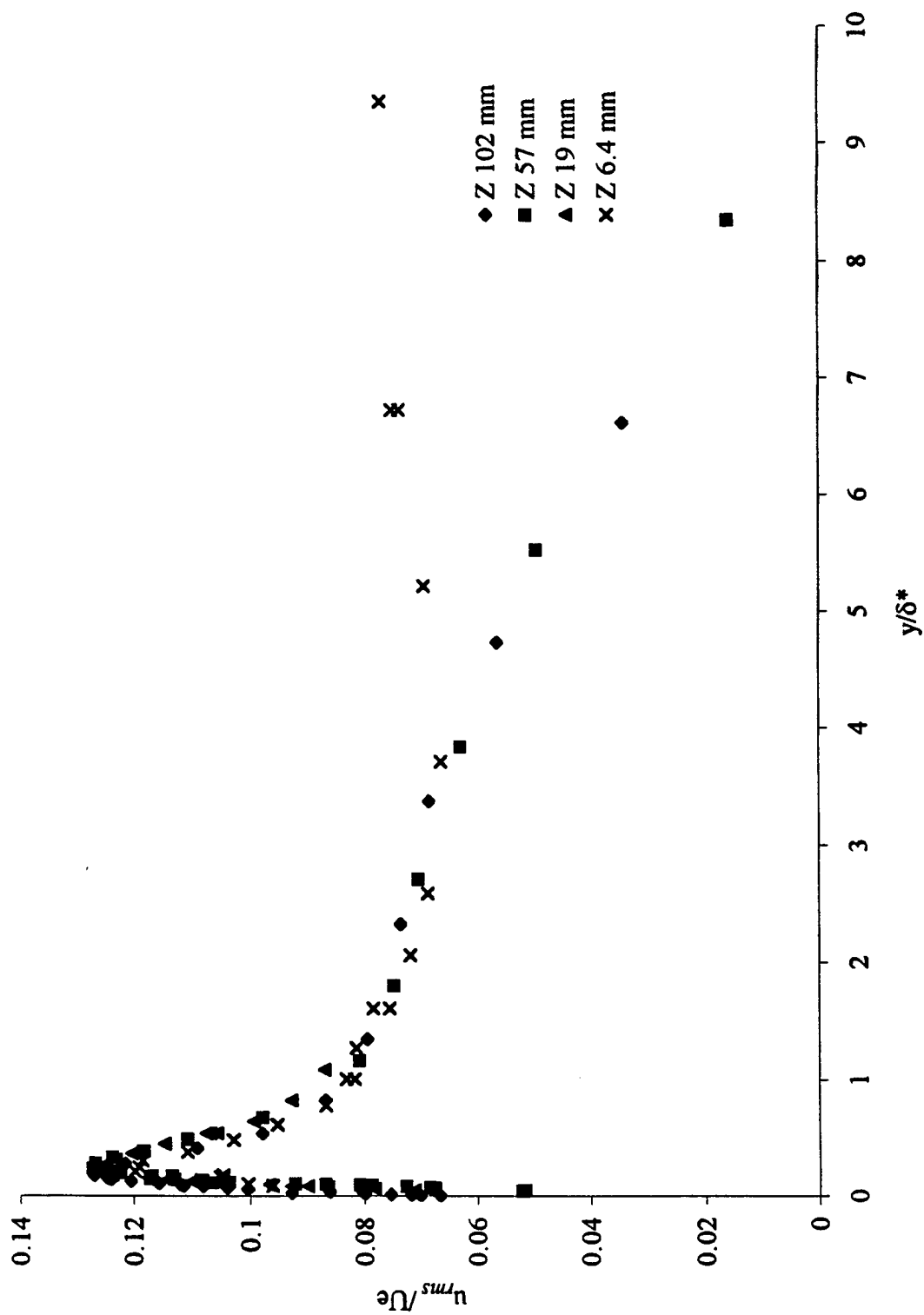


Figure 4.11 Axial turbulence intensity for the smooth test surface ranging into the corner at $X = 0.66$ m.

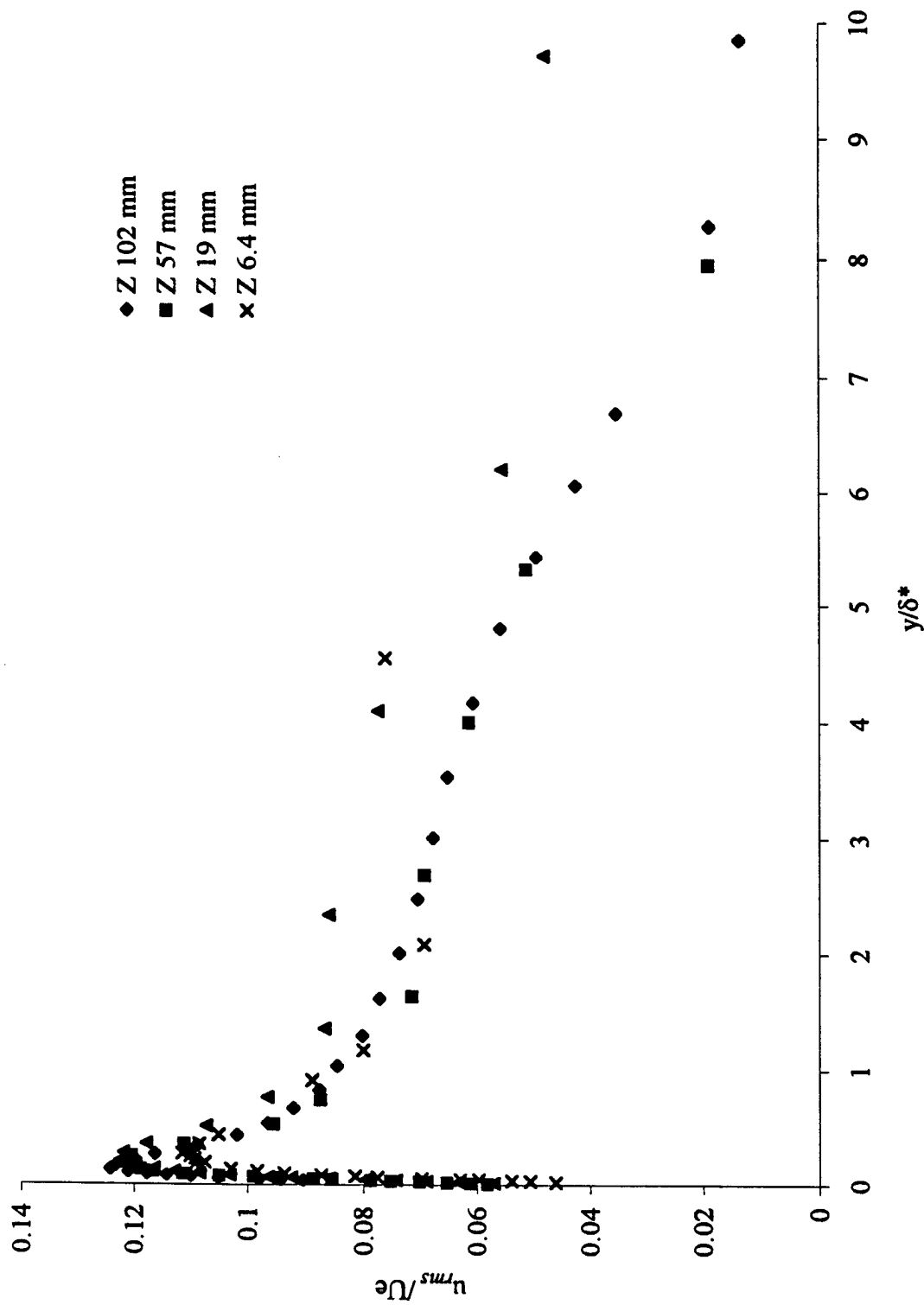


Figure 4.12 Axial turbulence intensity for the smooth test surface ranging into the corner at $X = 1.02$ m.

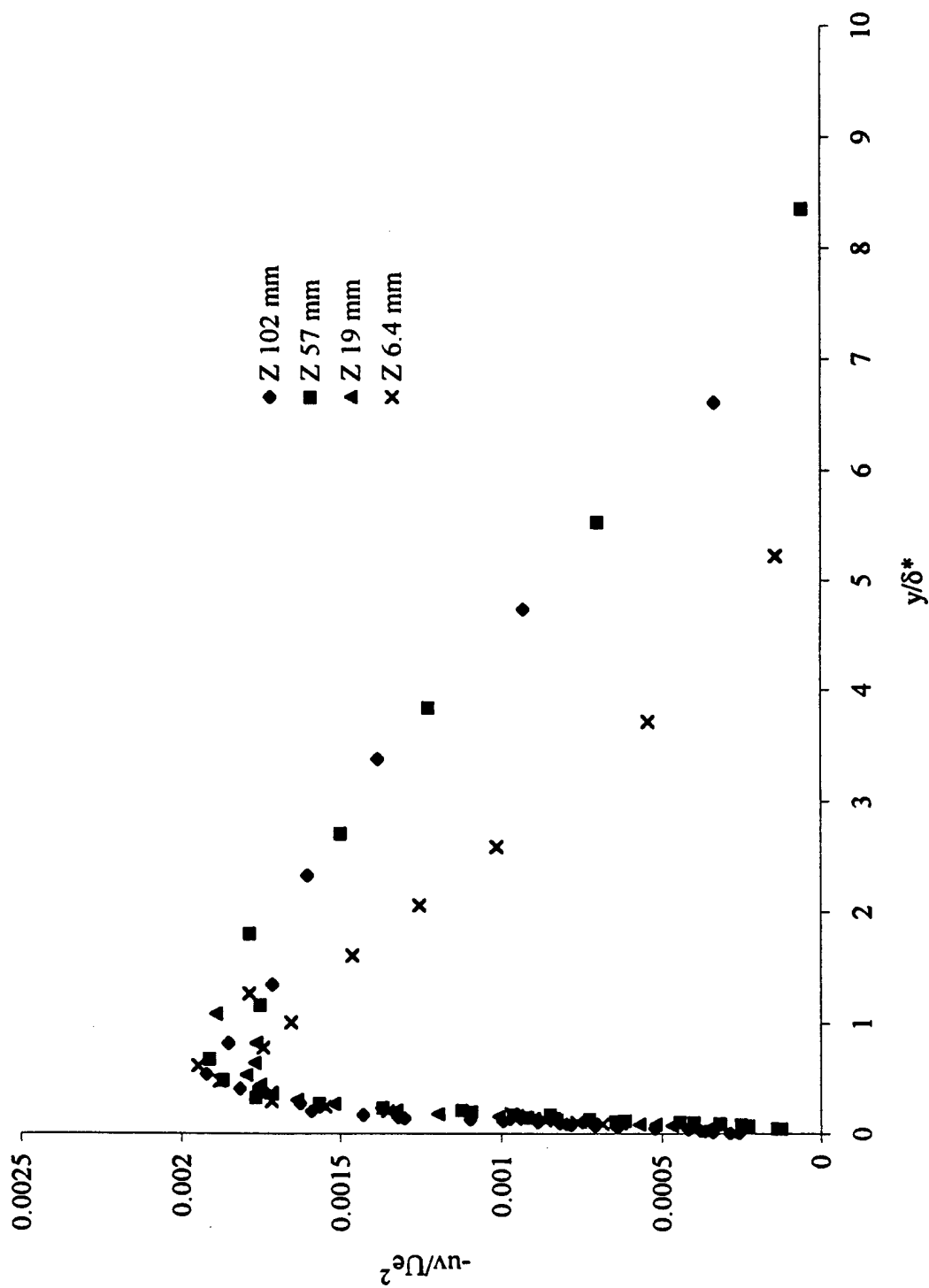


Figure 4.13 The $-uv$ Reynolds shear stress for the smooth test surface ranging into the corner at $X = 0.66$ m.

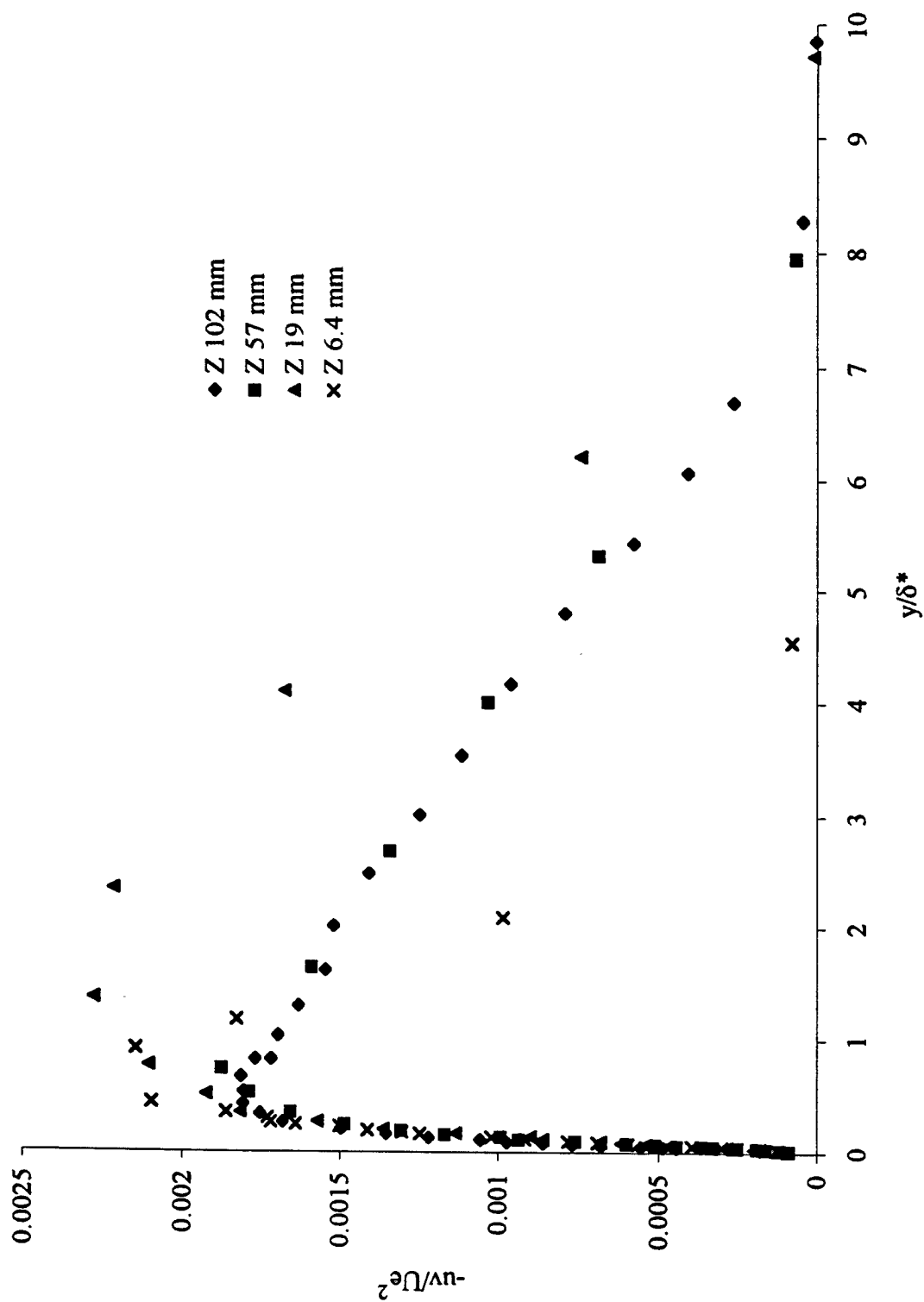


Figure 4.14 The $-uv$ Reynolds shear stress for the smooth test surface ranging into the corner at $X \approx 1.02$ m.

In summary, the mean axial velocity, relative secondary velocity and axial turbulence intensity profiles suggest the presence of a structure. As the structure travels downstream, the cross-sectional area in the YZ plane increases. In the $-\overline{uv}$ Reynolds shear stress profiles, we see that the area where the stress acts to diffuse the vortex strength moves away from the flat plate as the vortex moves downstream.

4.3. Comparison of two-dimensional turbulent boundary layer with various test surfaces

The objective of this research is to evaluate the three-dimensional corner flow with one rough surface. Having shown that the centerline of the smooth test surface is two-dimensional and that the corner flow with two smooth surfaces is comparable to prior skew induced research, we will now present the profiles comparing the flow along the centerline of the smooth and rough test surfaces.

In Figure 4.15, the mean axial velocity profiles in inner variables for smooth and rough surfaces shows the expected shift from the smooth wall log law. Data for both the smooth and rough test surfaces at $X = 1.02$ m and $Z = 102$ mm are plotted. A two-dimensional turbulent boundary layer exists above the smooth test surface. It has a shape factor of, $H = 1.3 \sim 1.4$, and a momentum based Reynolds number, $Re_\theta = 2000$ while the rough surface has $H \approx 1.45$ and $Re_\theta = 3450$. For comparison, experimental results from Schultz and Swain (1999) are also plotted. These profiles are above various biofilms with k^+ of 61, 65, and 81 and Re_θ of 14,000, 14,000 and 19,000. Although two of their data sets have the same Reynolds number, increasing k^+ shifts the profile upward. Figure 4.16

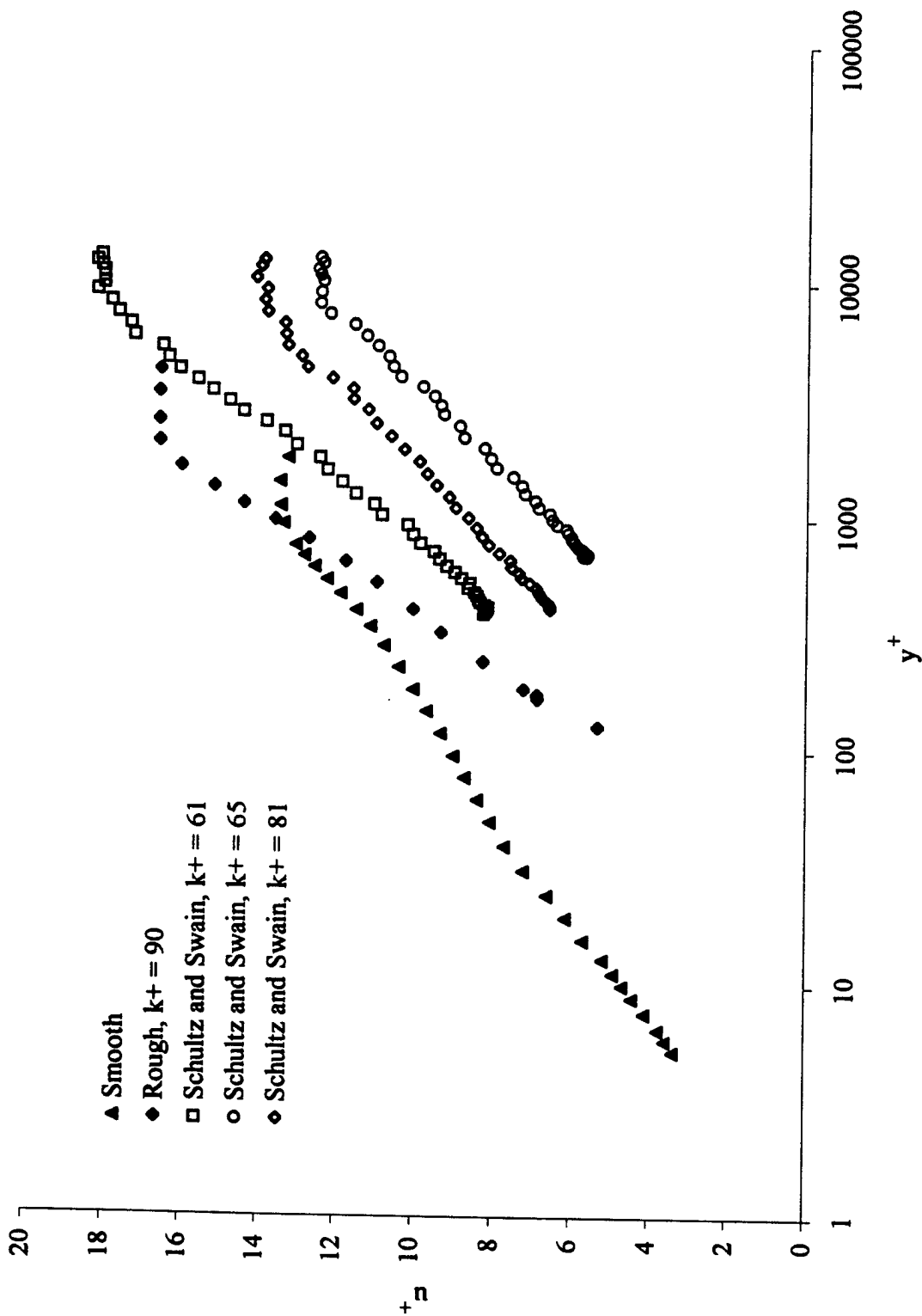


Figure 4.15 Comparison of the mean axial velocity in inner variables for the smooth and rough test surfaces at $X = 1.02$ m and $Z = 102$ mm.

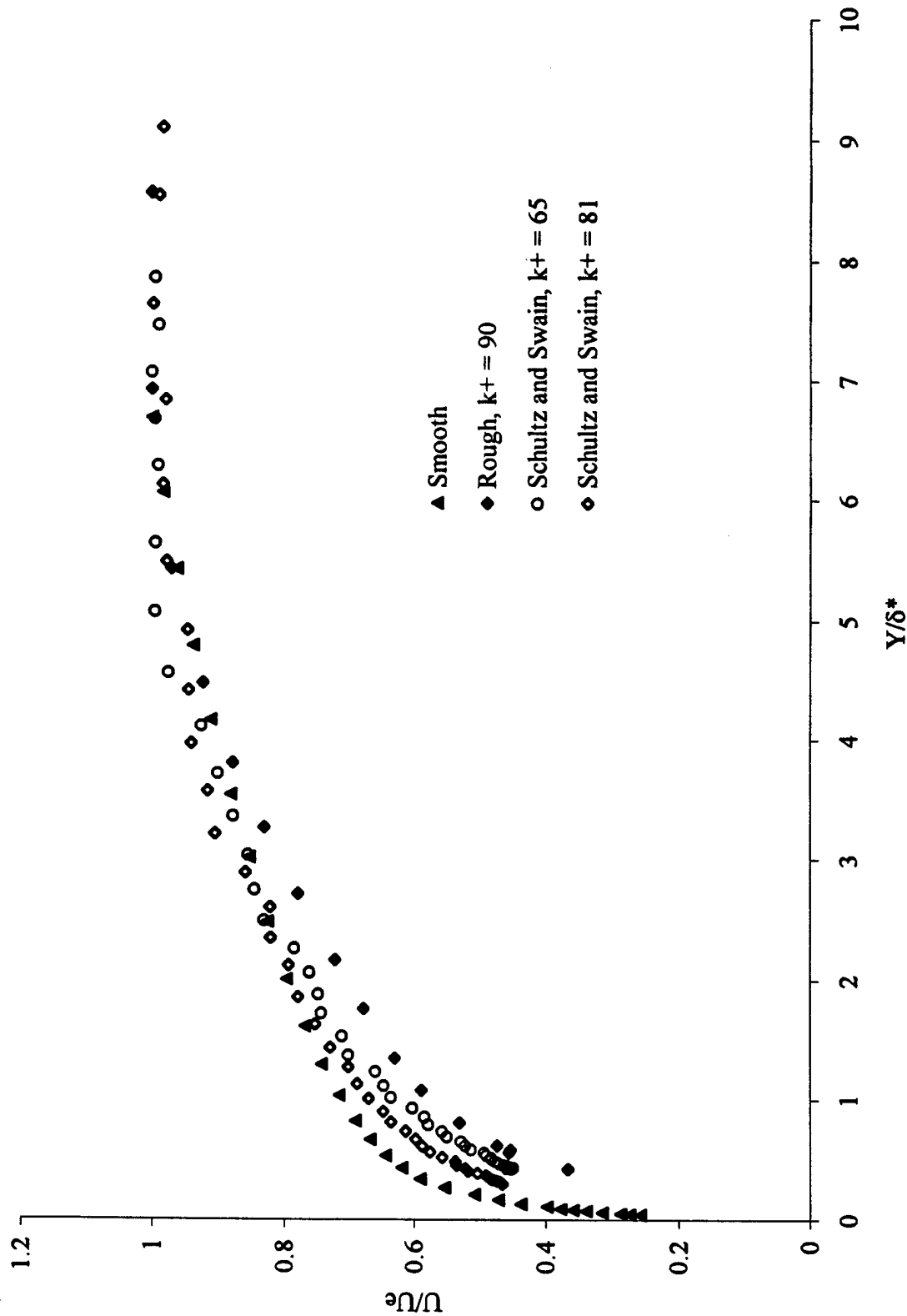


Figure 4.16 Mean axial velocity profiles for the smooth and rough test surfaces at $X = 1.02$ m and $Z = 102$ mm.

shows that the mean axial velocity profiles normalized by the free stream velocity and plotted versus y/δ^* appear to be very different. To examine the outer region of the boundary layer, the velocity defect is plotted in Figure 4.17. The profiles for the smooth and rough surfaces follow similar trends. The profile for the rough surface decreases at a greater rate than the smooth surface.

The axial turbulence intensity normalized by the free stream velocity is plotted in Figure 4.18. Above the rough test surface, the maximum normalized turbulence intensity is 0.0134, greater than the maximum of 0.0124 above the smooth surface. The profile for the smooth test surface decreases at a faster rate than the profile for the rough surface.

Profiles of the $-\overline{uv}$ Reynolds shear stress normalized by the free stream velocity squared are plotted in Figure 4.19. The Reynolds shear stress magnitude above the rough test surface is 0.0043 near the wall compared to 0.0018 above the smooth test surface. While the stress in the outer region of the smooth surface boundary layer decreases at the rate for a two-dimensional profile, the higher stress of the rough surface decreases at a faster rate until $y/\delta^* \approx 5$. The profile for the rough surface goes to zero at $y/\delta^* \approx 7$ while the smooth occurs at $y/\delta^* \approx 8$.

In summary, the rough test surface with its three-dimensional elements thickens the boundary layer compared to the boundary layer for the smooth test surface. As expected, there is a shift in the mean axial velocity. Above the rough surface, the axial turbulence intensity behaves very differently than that above the smooth surface. The intensity achieves a minimum further from the wall for the rough case. Comparing the $-\overline{uv}$ Reynolds shear stress, the magnitude for the rough surface profile is three times greater than the smooth surface profile.

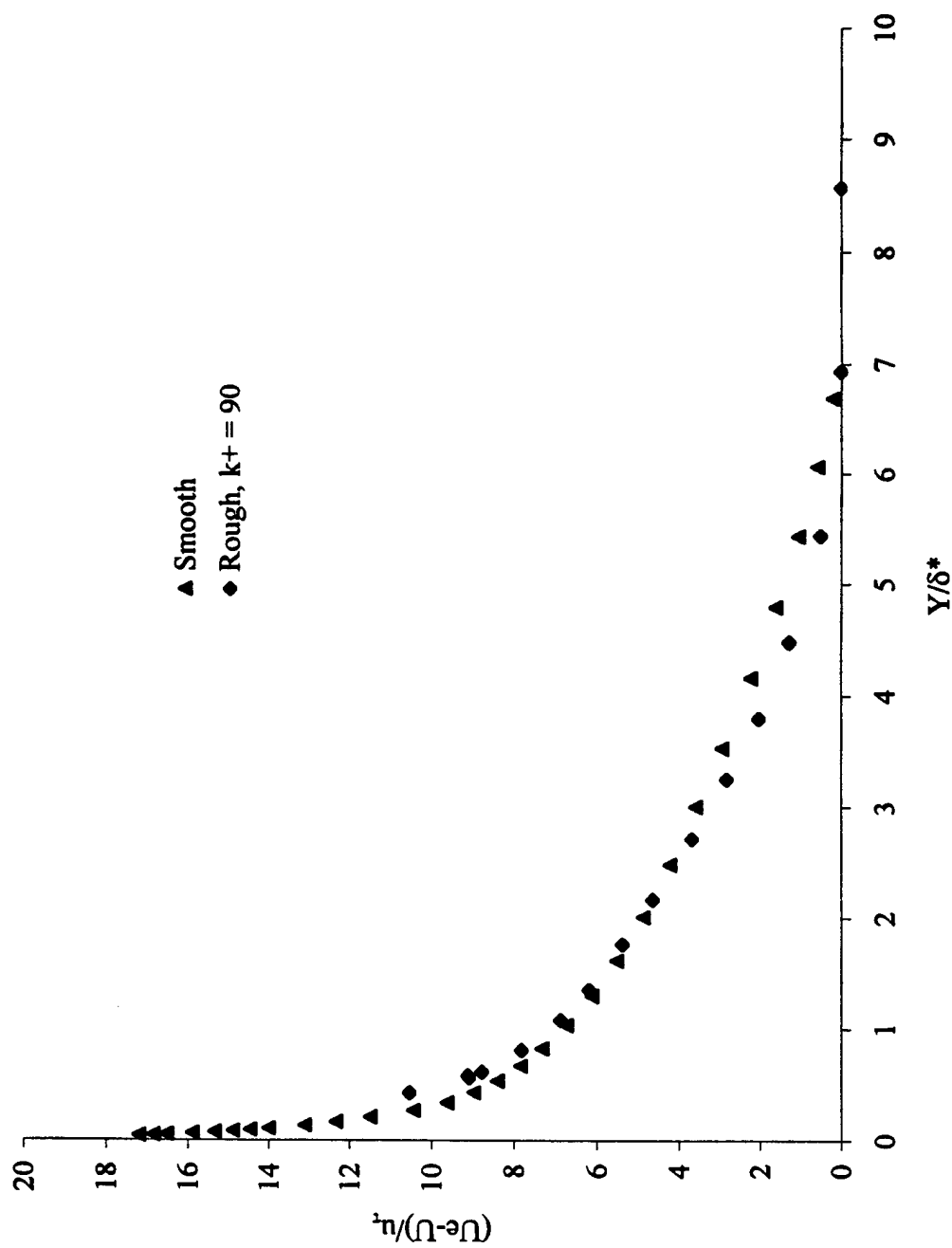


Figure 4.17 Mean axial velocity profiles plotted as a velocity defect for smooth and rough test surfaces at $X = 1.02$ m and $Z = 102$ mm.

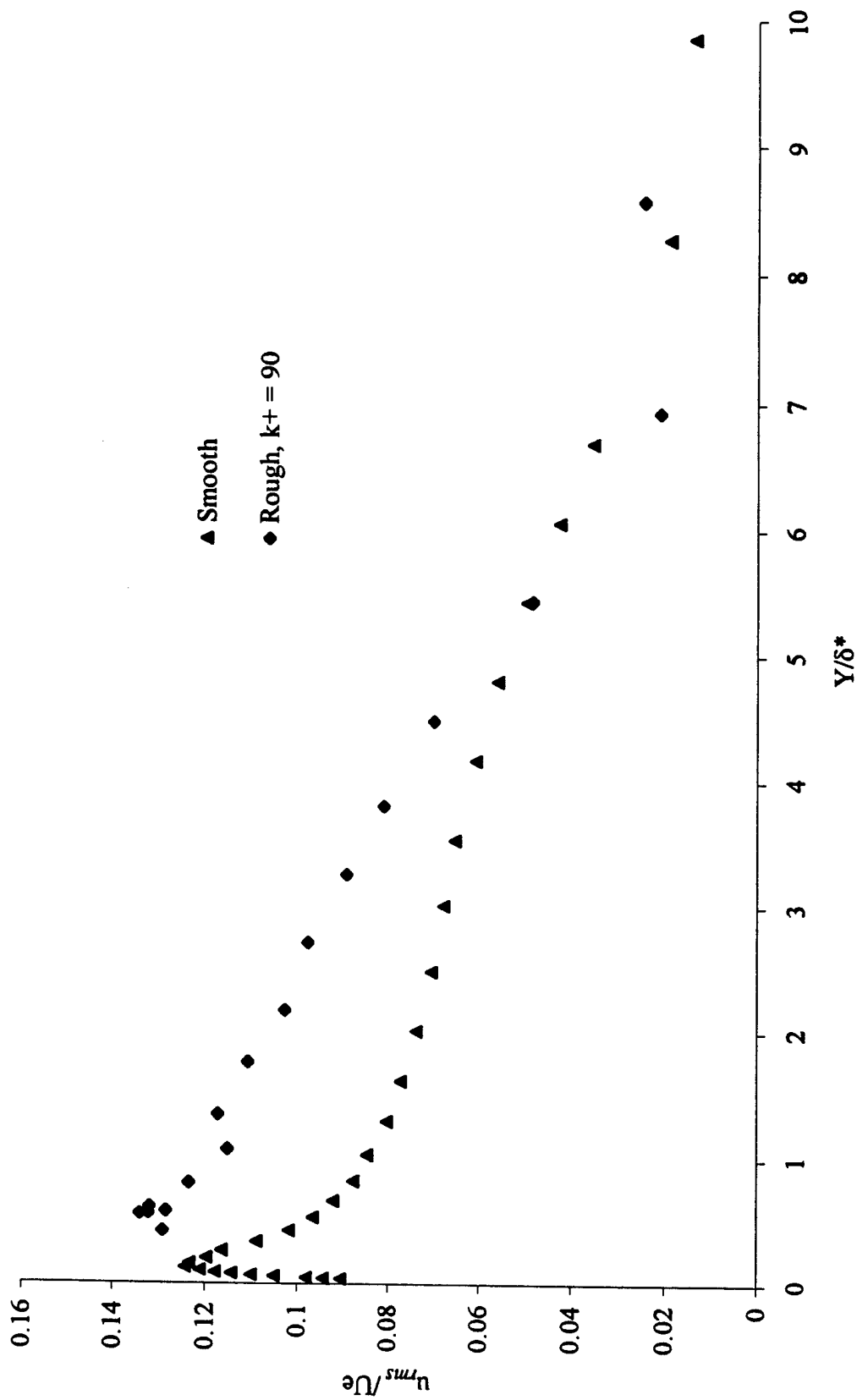


Figure 4.18 The axial turbulence intensity for the smooth and rough test surfaces at $X = 1.02$ m and $Z = 102$ mm.

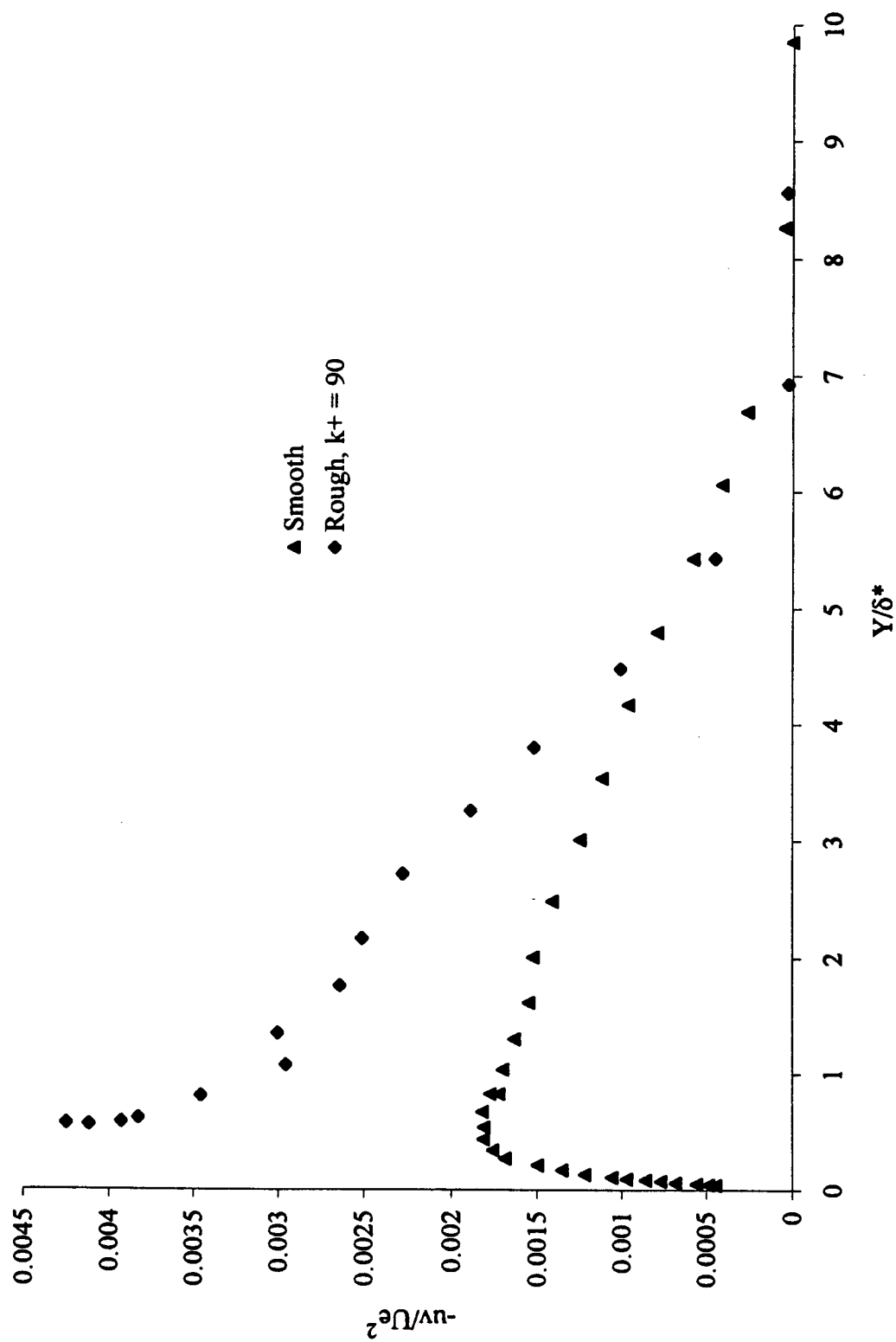


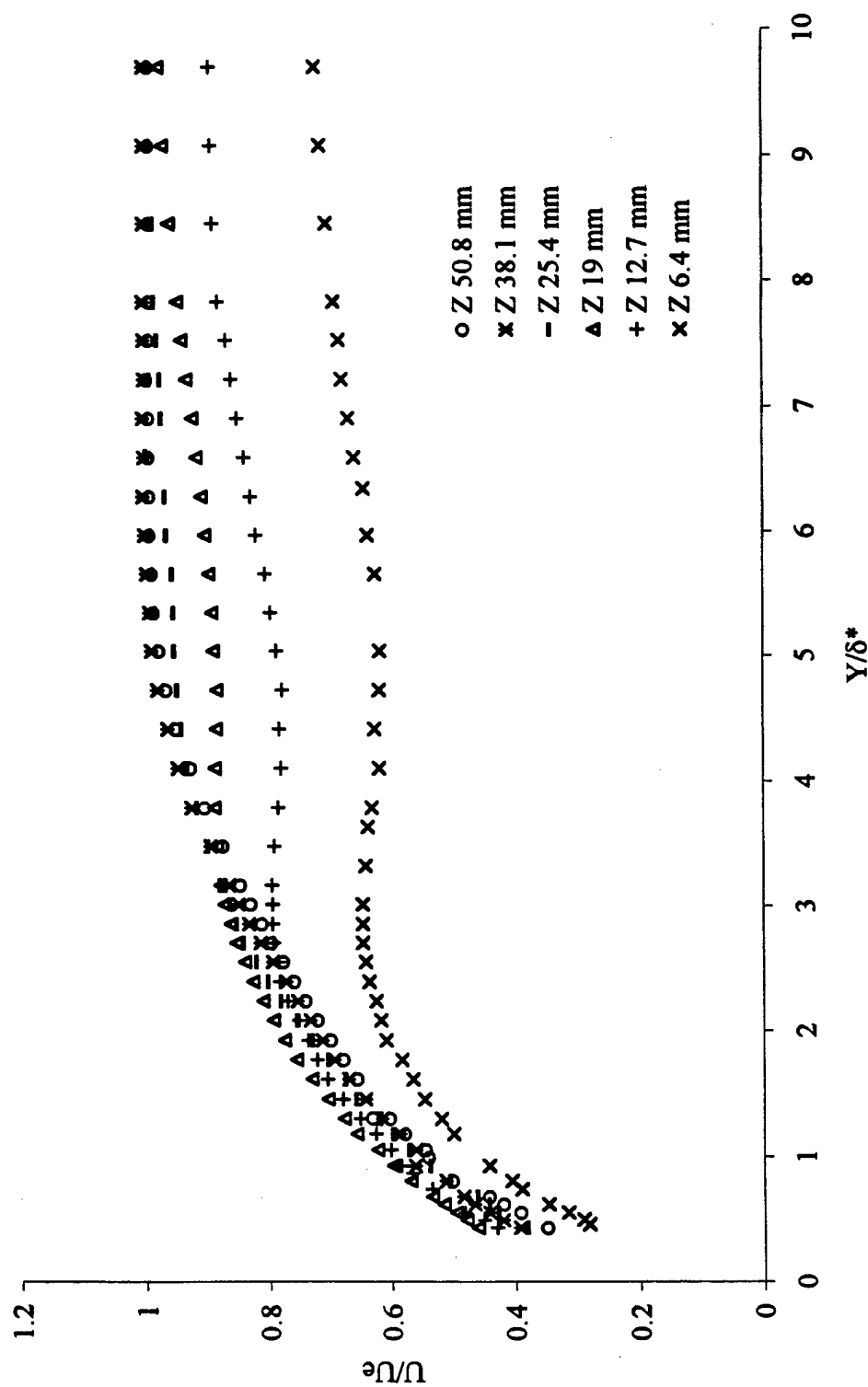
Figure 4.19 The $-uv$ Reynolds shear stress for the smooth and rough test surfaces at $X = 1.02$ m and $Z = 102$ mm.

4.4 Three-dimensional turbulent boundary layer with rough test surface

As the corner is approached, the presence of the rough test surface acts to thicken the boundary layer. The velocity and length scales are the free stream velocity and the displacement thickness away from the corner. Profiles of the mean axial velocity, relative secondary velocities, axial turbulence intensity and Reynolds shear stress are presented.

In Figure 4.20, the mean axial profiles at $X = 0.66$ m are shown. As the corner is approached, the profiles depart from the profile at $Z = 50.8$ mm. At $Z = 25.4$ mm, the profile changes about $y/\delta^* \approx 3.5$. For $y/\delta^* < 3.5$, the profile at this location is fuller while for $y/\delta^* > 3.5$, the profile decreases. This decrease exists for $4 < y/\delta^* < 8$. The profile at $Z = 19$ mm follows a similar trend. However, nearer the corner at $Z = 12.7$ mm, the location of the change decreases. Finally, at $Z = 6.4$ mm, the profile does not approach the others. It decreases away from the wall for $3 < y/\delta^* < 7$ and beyond this becomes constant. As y/δ^* increases and Z decreases, the boundary layer along the vertical corner surface is entered and the maximum axial velocity ratio decreases.

The mean axial velocity profiles at $X = 1.02$ m are shown in Figure 4.21. Similar trends are seen in these profiles as Z decreases. For $Z = 38.1$ mm, the change in the nature of the velocity profile begins at $y/\delta^* \approx 3.3$, further than at $X = 0.66$ m. Nearer the corner at $Z = 25.4$ mm, the change occurs at $y/\delta^* \approx 4.2$. At $Z = 14$ mm, the change occurs at $y/\delta^* \approx 2.8$ while at $Z = 6.4$ mm the profile does not approach the others. Again, in the outer region of the boundary layer, the profiles decrease and increase to 1 at $Z = 25.4$, 38.1, and 50.8 mm. The profiles at $Z = 14$ and 6.4 mm do not exit the vertical wall boundary layer and the maximum velocity ratio decreases.

Figure 4.20 The mean axial velocity for the rough test surface ranging into the corner at $X = 0.66$ m.

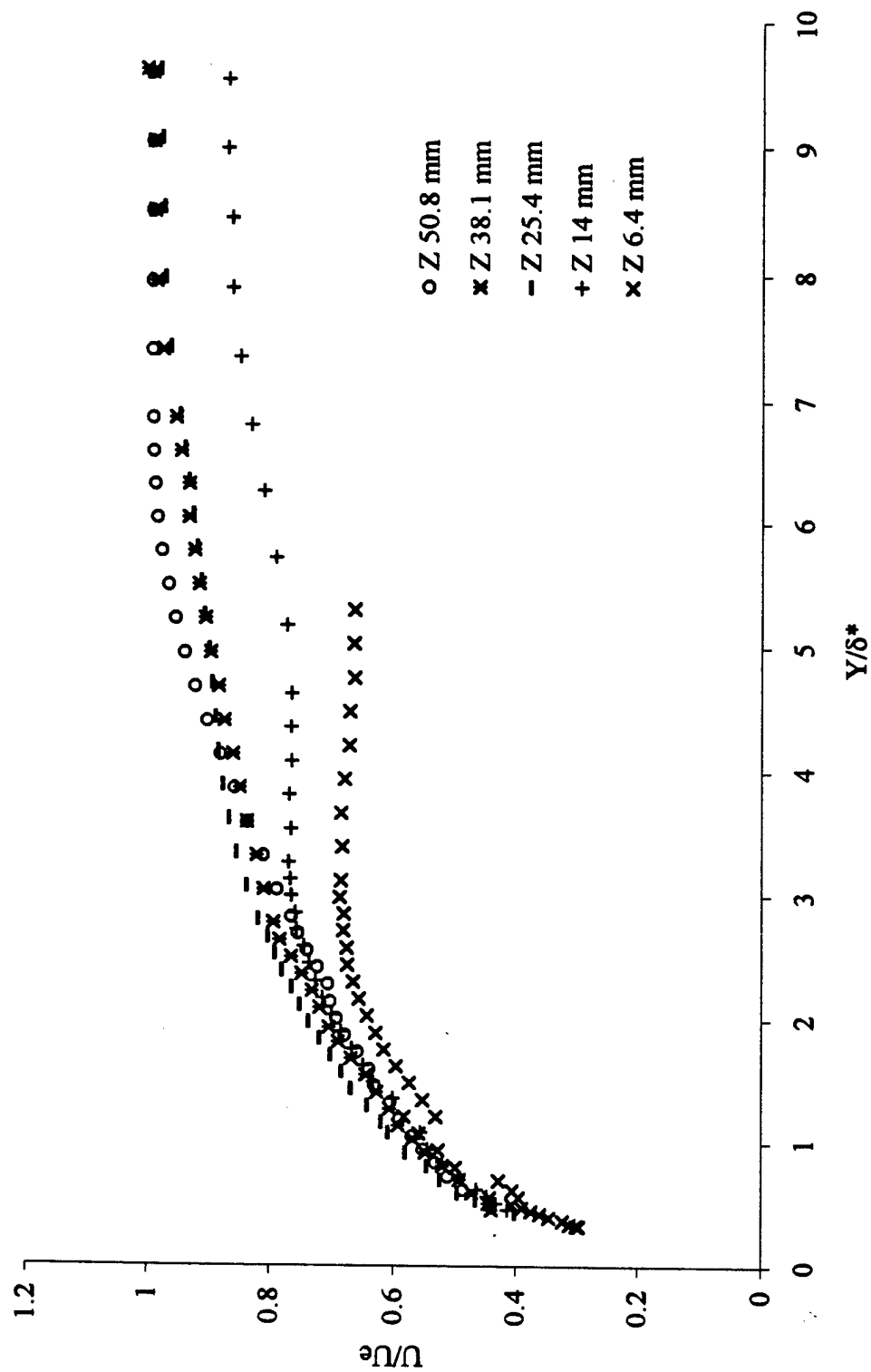


Figure 4.21 The mean axial velocity for the rough test surface ranging into the corner at $X = 1.02$ m.

At $X = 0.66$ m, the maximum wall-normal secondary velocity occurs in the profile at $Z = 25.4$ mm and $y/\delta^* \approx 0.4$. The ratios are all less than 1% for $y/\delta^* > 1$. Further downstream at $X = 1.02$ m, the maximum ratio has increased to 4.4 % at $Z = 6.4$ and 25.4 mm for $y/\delta^* < 1$.

At $X = 0.66$ m, the relative cross-stream secondary velocity ratios at $Z = 6.4, 38.1$, and 50.8 mm are greater than 12 % for $y/\delta^* < 1$. The ratios decrease and become constant at 6 % for $y/\delta^* > 1$. The maximum ratio at $X = 1.02$ m is 11 % and occurs at $Z = 50.8$ mm, which is furthest from the corner. Because of seeding limitations, no cross-stream velocity measurements were made at $Z = 6.4$ mm for $y/\delta^* < 1.2$.

The primary velocity contours are plotted in Figure 4.22 for measurements ranging into the corner at $X = 0.66$ m. The numbers on the contours represent the velocities normalized by the free stream velocity. For $Z > 0.03$ m, the contours are nearly parallel along the rough surface. Contours along the flat plate are distorted. Figure 4.23 shows the secondary velocity vectors at the same axial location. In the Y-Z plane, no large vortex is apparent. Near the rough surface, the vectors display the edge of structures. Figure 4.24 is a snapshot of the corner region above the rough surface. In the range $0 < Y < 0.005$ m, the secondary velocity vectors suggest that multiple smaller structures are present near the rough surface.

The axial turbulence intensity at $X = 0.66$ m and 1.02 m in Figures 4.25 and 4.26 include the profiles away from the corner. At $X = 0.66$ m, the turbulence intensity at $Z = 38.1$ and 50.8 mm is greatest near the wall, decreasing with increasing y/δ^* . At $Z = 19$ and 25.4 mm, the profiles follow similar trends as the profiles at $Z = 38.1$ mm for $y/\delta^* < 1.3$. For $y/\delta^* > 1.3$, the profile at $Z = 19$ mm decreases to a constant intensity. This

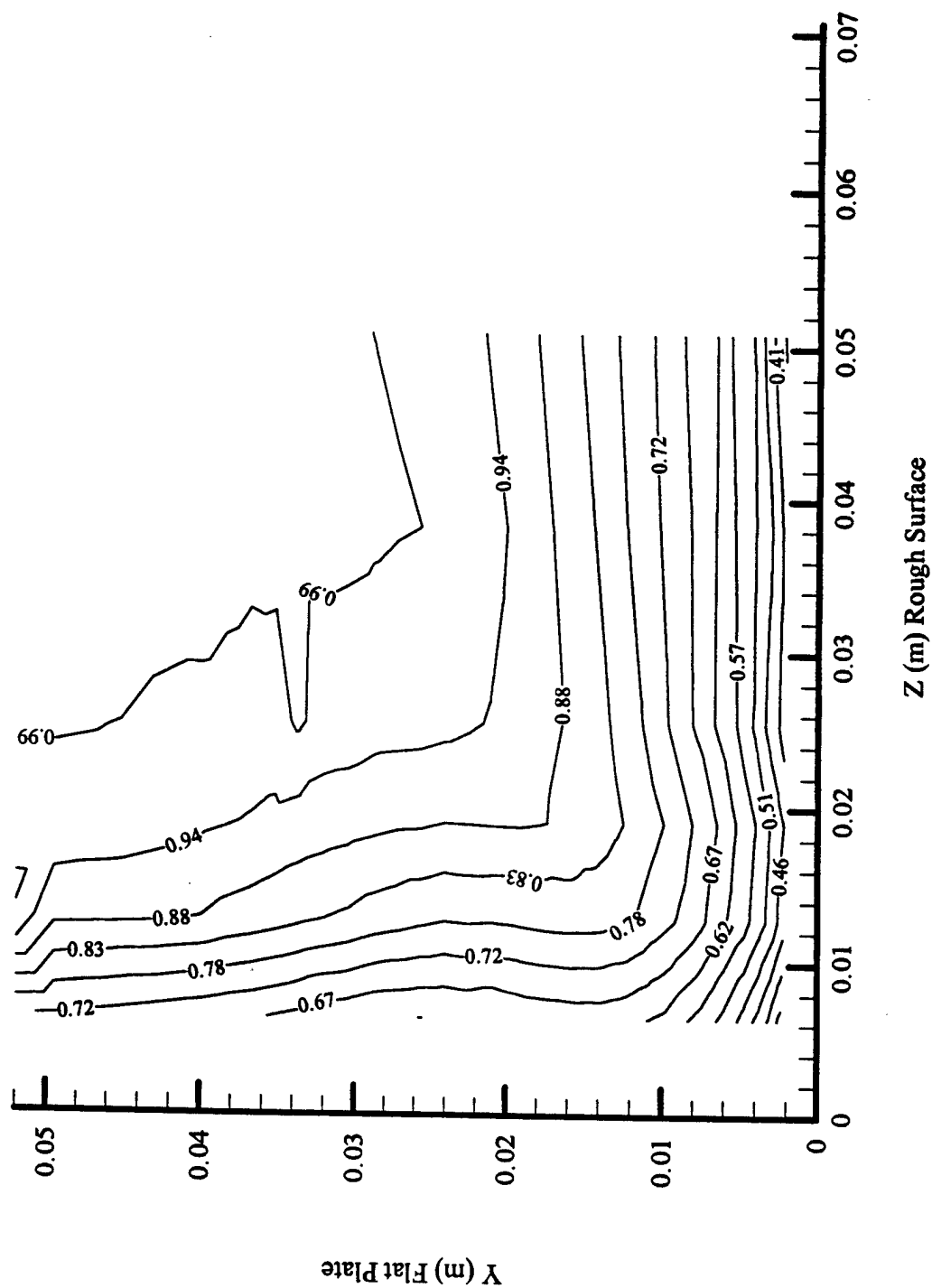


Figure 4.22 The primary velocity contours for the rough test surface ranging into the corner at $X = 0.66$ m.

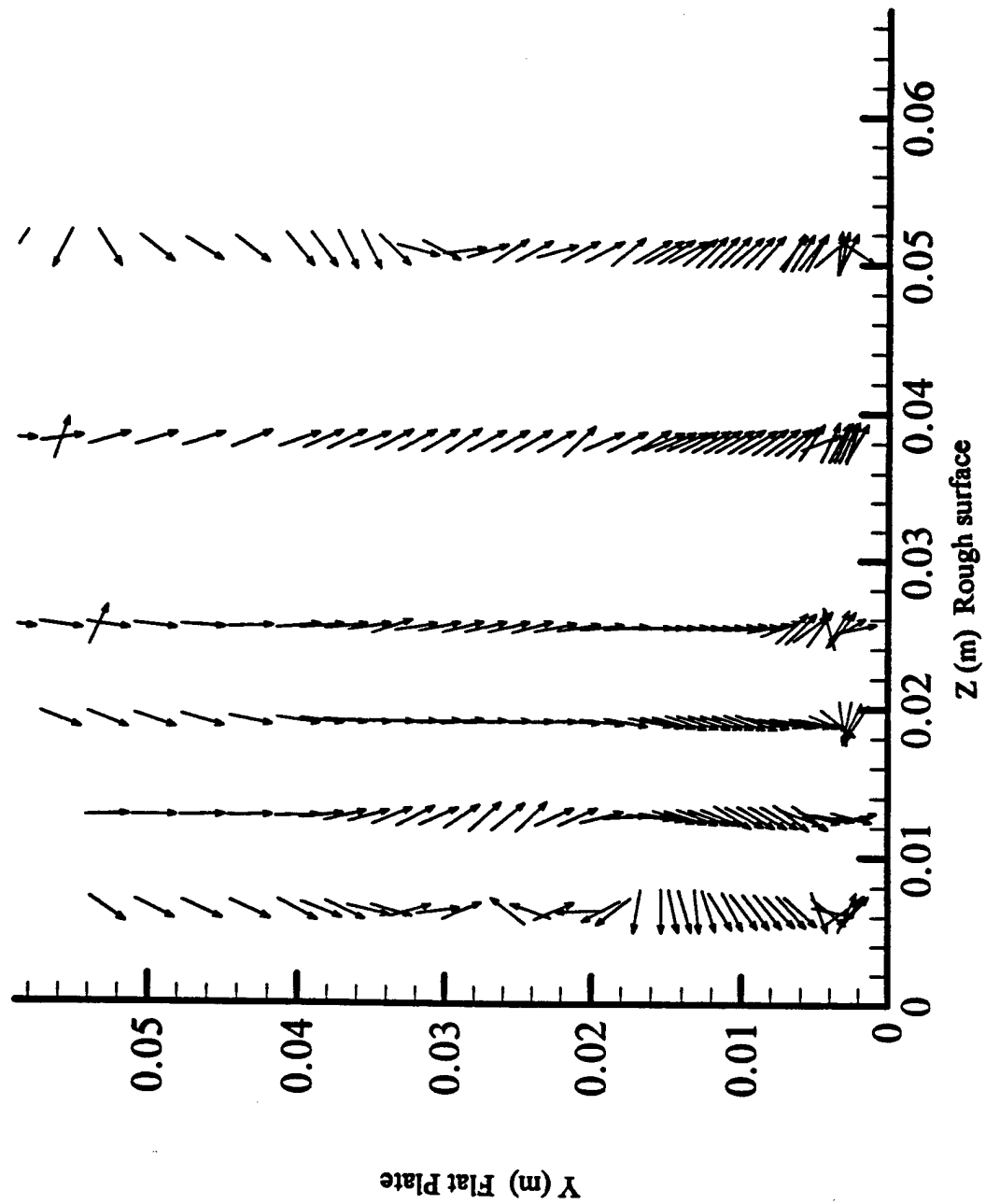


Figure 4.23 The secondary velocity vectors for the rough test surface ranging into the corner at $X = 0.66$ m.

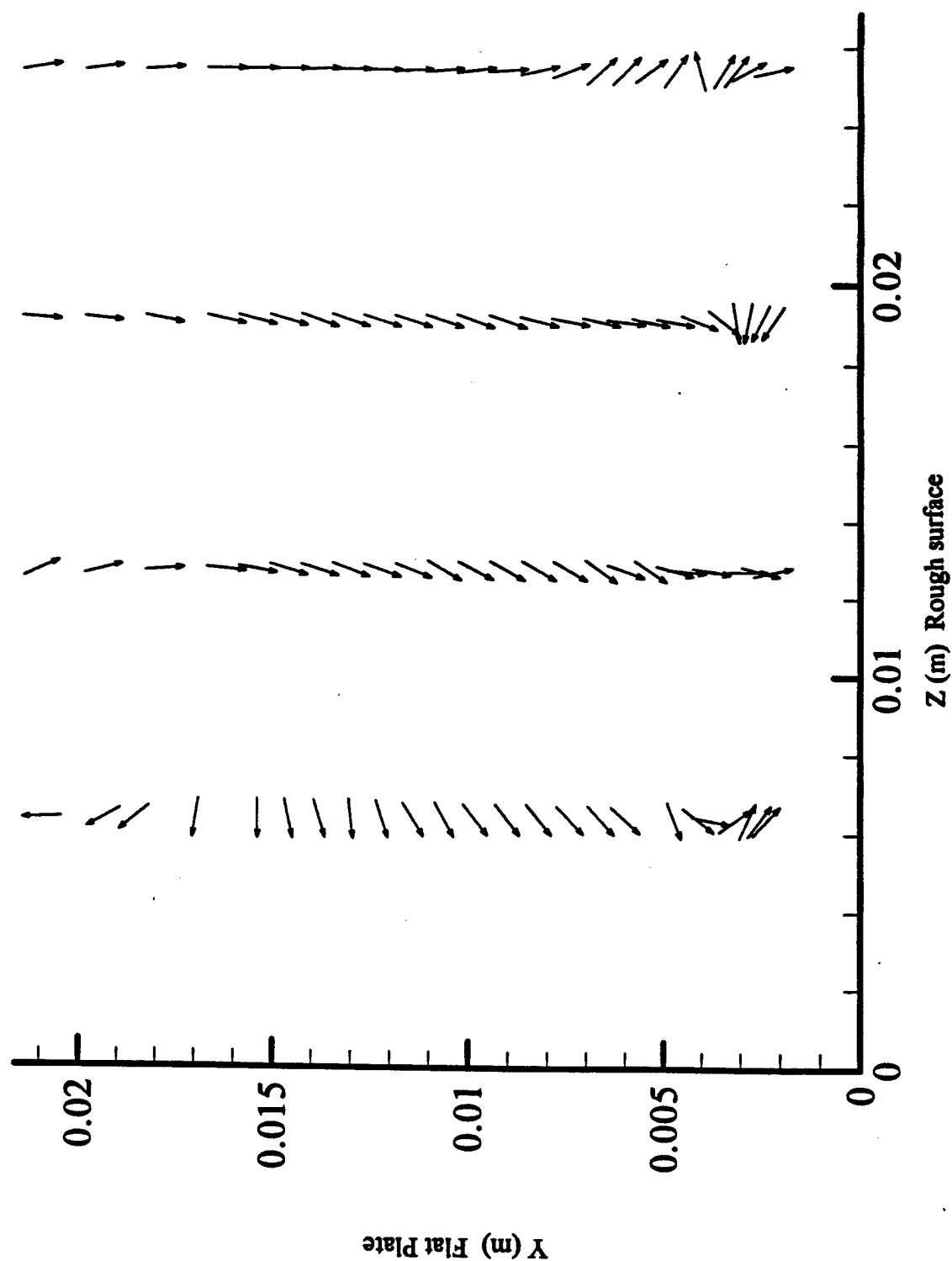


Figure 4.24 The secondary velocity vectors for the rough test surface from $Z = 0.03$ m ranging into the corner at $X = 0.66$ m.

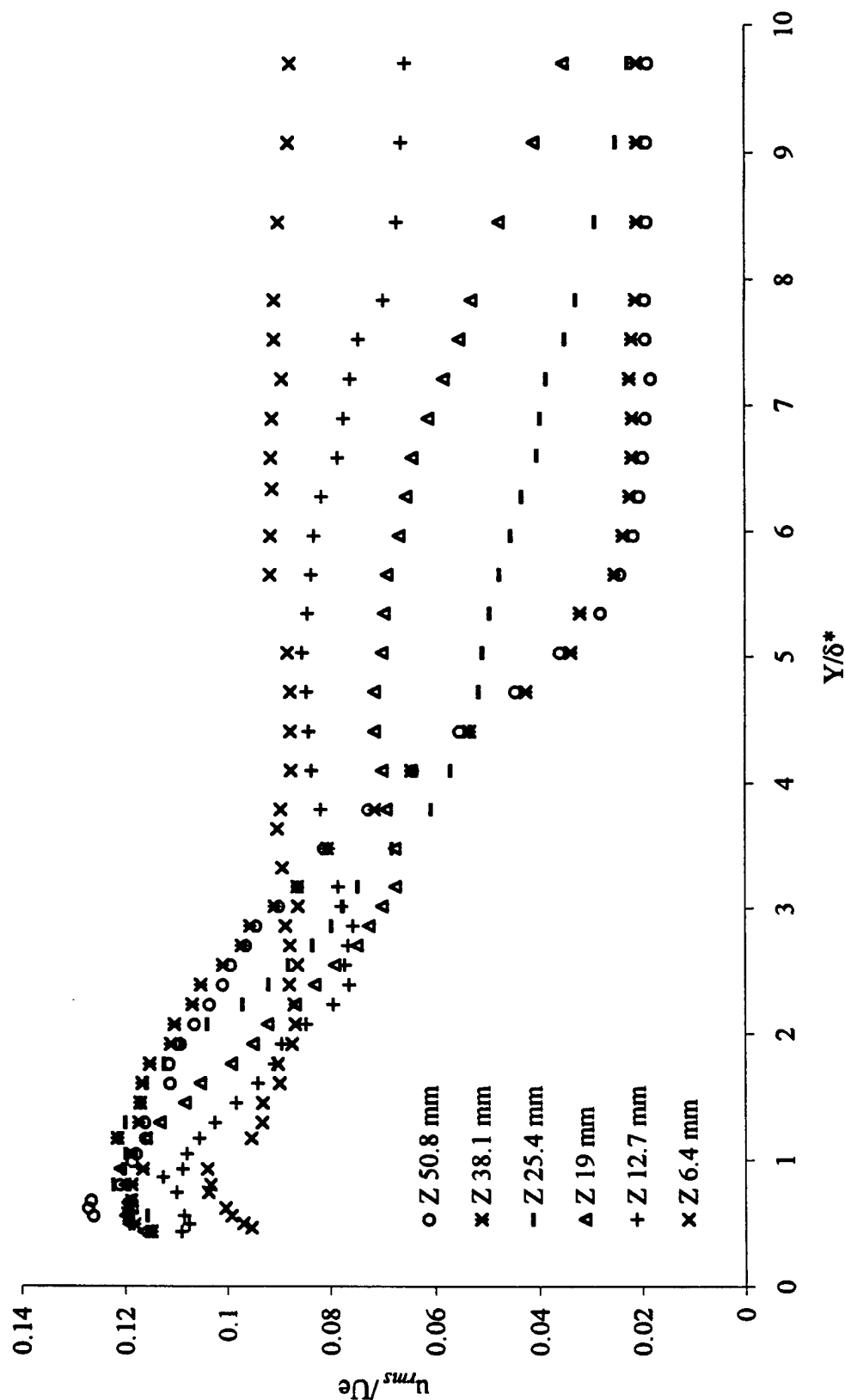


Figure 4.25 The axial turbulence intensity for the rough test surface ranging into the corner at $X = 0.66$ m.

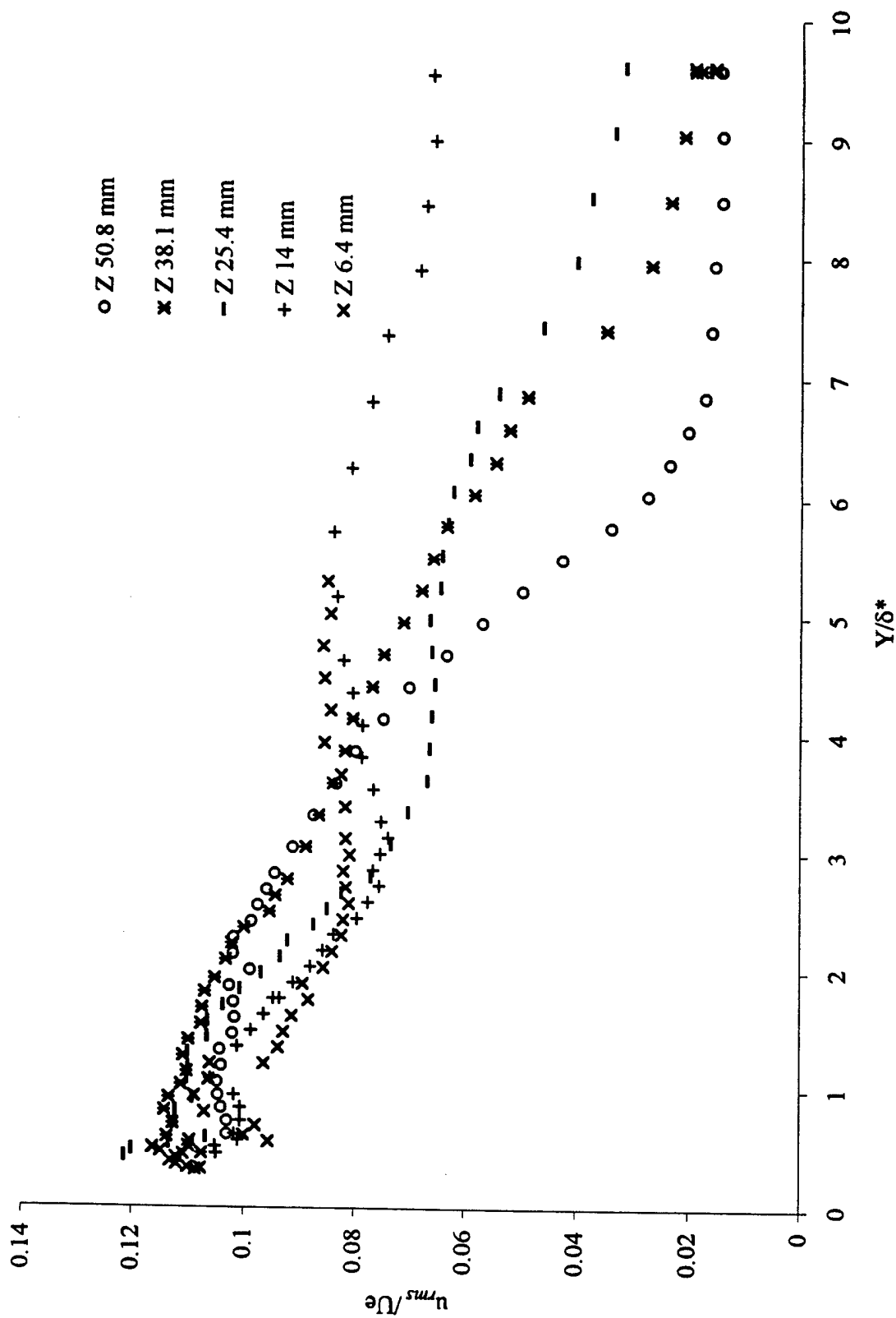


Figure 4.26 The axial turbulence intensity for the rough test surface ranging into the corner at $X = 1.02$ m.

constant value is 0.035, greater than the profiles at $Z = 25.4, 38.1,$ and 50.8 mm. At $Z = 6.4$ mm, the intensity is 0.10 for $y/\delta^* < 1.3$ and decreases to 0.09 for $y/\delta^* > 1.3$. The axial turbulence intensity profiles at $X = 1.02$ m change compared to those at $X = 0.66$ m. At $Z = 50.8$ mm in Figure 4.26, the intensity is lower than that upstream at the same cross-stream location. At $Z = 6.4$ and 14 mm, the intensity is 11 and 10 % for $y/\delta^* \approx 1.3$. Beyond this, these profiles gradually decrease to 0.085 for $y/\delta^* \approx 5$.

Profiles of the $-\overline{uv}$ Reynolds shear stress at $X = 0.66$ m are shown in Figure 4.27. The profiles at $Z = 38.1$ and 50.8 mm increase to a maximum near the rough surface and decrease as the distance from the test surface increases. At $Z = 6.4$ mm, the stress profile increases to a maximum of 0.0008 and approaches zero at $y/\delta^* \approx 3.5$. For $y/\delta^* > 3.5$, the stress increases to 0.0004 and decreases as y/δ^* increases. At $X = 1.02$ m, the Reynolds shear stress profiles in Figure 4.28 change compared to those in Figure 4.27. The profile at $Z = 50.8$ increases to a maximum of 0.001 and decreases as distance from the test surface increases. However, the profile at $Z = 38.1$ mm increases to .0014 before decreasing. The rate of decrease also differs for $4 < y/\delta^* < 10$. At $Z = 14$ mm, the profile increases near the test surface and then decreases for $y/\delta^* < 4$. Then, the stress increases to 0.0004 and decreases with increasing y/δ^* .

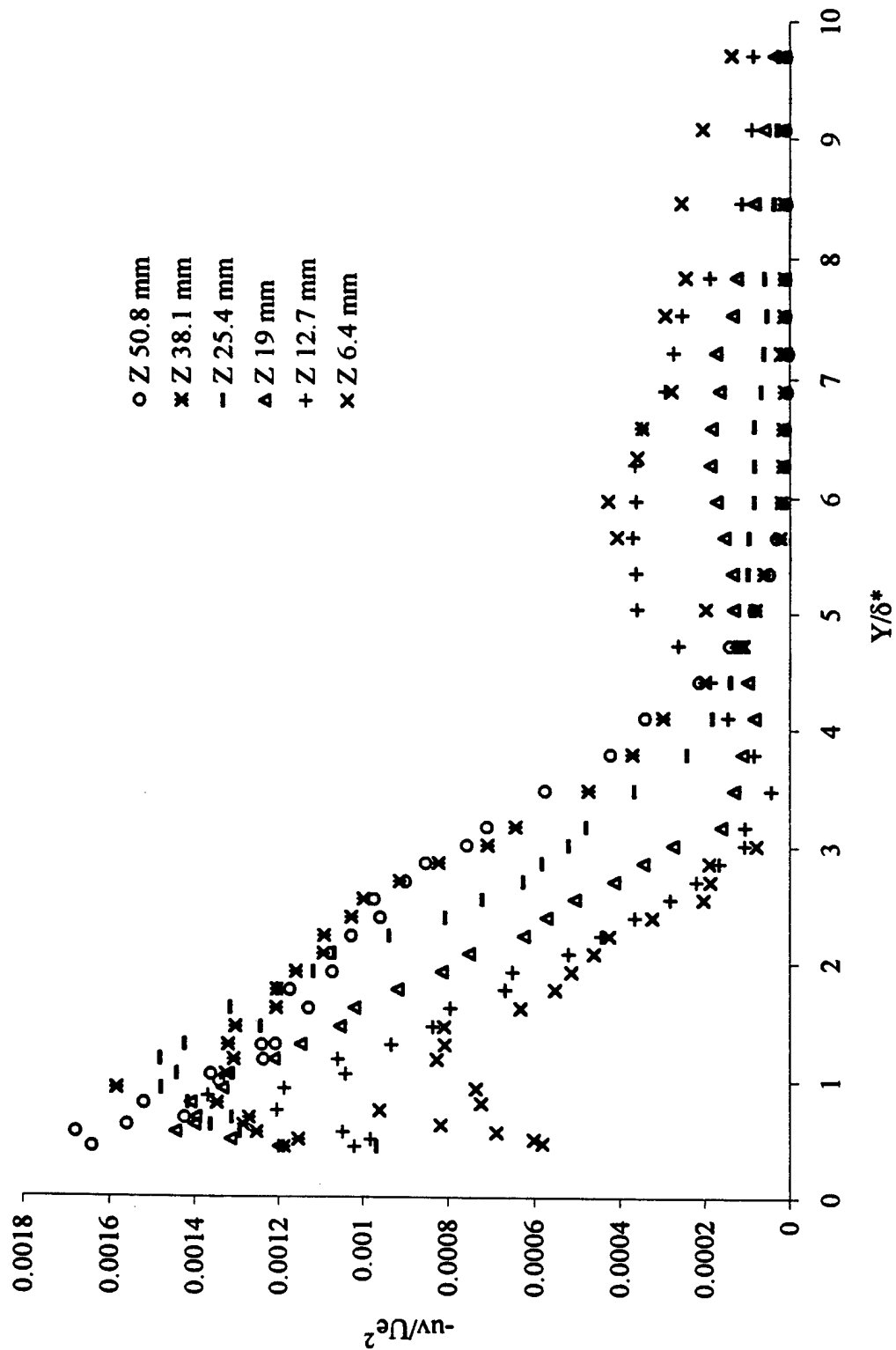


Figure 4.27 The -uv Reynolds shear stress for the rough test surface ranging into the corner at X = 0.66 m.

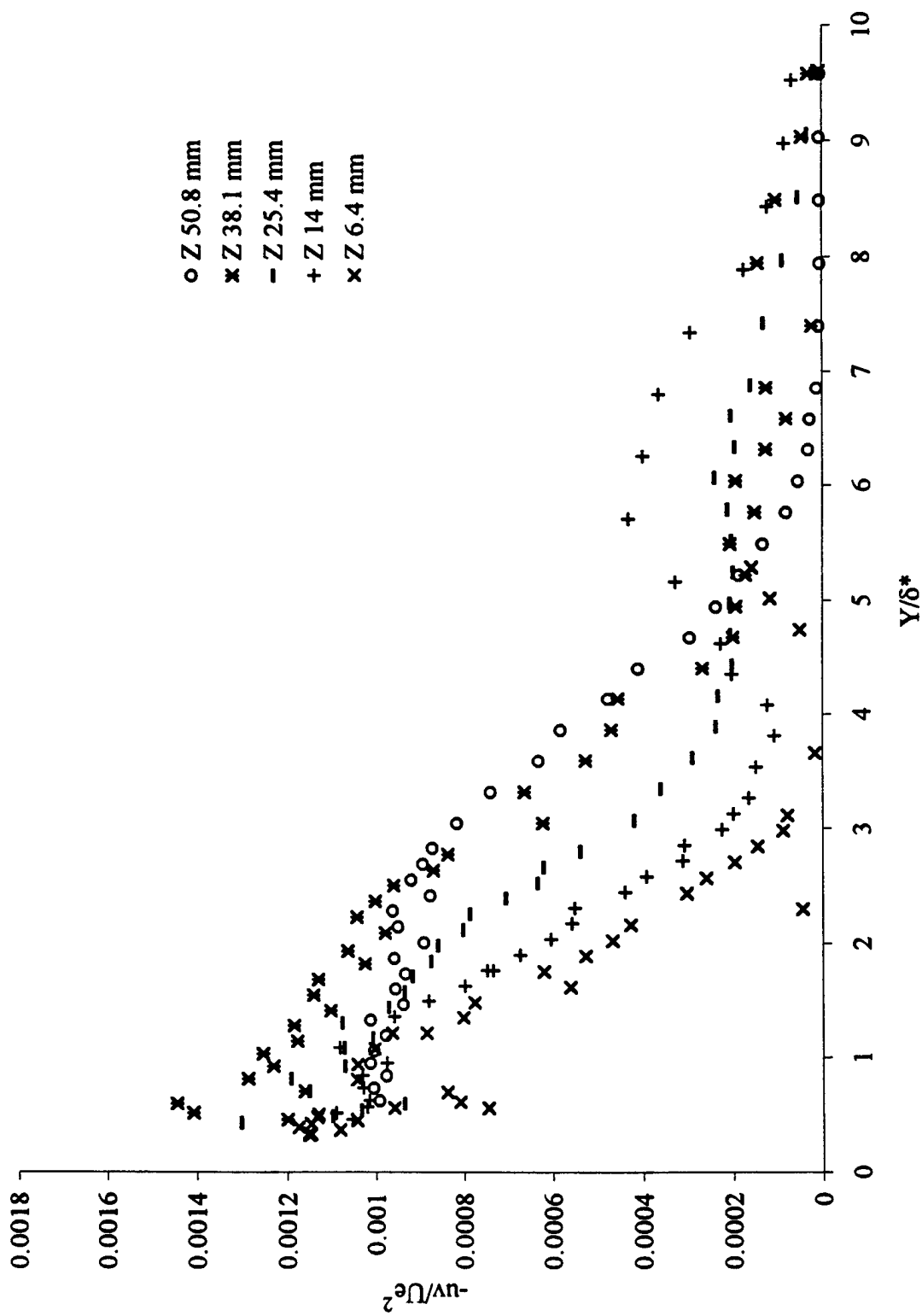


Figure 4.28 The $-uv$ Reynolds shear stress for the rough test surface ranging into the corner at $X = 1.02$ m.

Chapter 5

Conclusions

Using the test section and the instrumentation described in Chapter 2, a database for incompressible, three-dimensional asymmetric corner flow with zero pressure gradient is under development. Computational fluid dynamic modeling of a three-dimensional flow such as one along a corner formed by a rough surface and smooth wall requires an accurate database for comparison. This condition occurs on man-made structures and vehicles, particularly in a marine environment. With this in mind, we developed a database for incompressible, three-dimensional skew induced corner flow with one rough wall. Mean velocity, relative secondary velocity, turbulence intensity and Reynolds shear stress profiles were measured.

The effect of the geometry on the flow was presented. Along the centerline of the smooth test surface, there is a two-dimensional boundary layer. The flow in the corner above this surface is comparable to that presented by Shabaka (1979) and McMahon, Hubbartt, and Kubendran (1982).

When the smooth test surface was replaced with a rough one, the boundary layer thickness increased above the test surface. The relative secondary cross-stream velocity ratio is high near the surface at $X = 0.66$ m near the corner at $Z = 6.4$ mm and further out at 38.1 and 50.8 mm. Between these locations, the ratios are lower. Downstream at $X = 1.02$ m, the relative secondary cross-stream velocity ratio decreases except at $Z = 50.8$ mm. Plots of the secondary velocity vectors suggest that the presence of the roughness has disrupted the flow structure.

Additional results such as higher order moments of velocity will be available in the Ph D dissertation by James Roche.

BIBLIOGRAPHY

- Adrian, R. J., 1983. "Laser Velocimetry," in Fluid Mechanics Measurements, ed. R. J. Goldstein, Hemisphere Pub., pp. 155-244.
- Andreopoulos, J., F. Durst, Z. Zaric, and J. Jovanovic, 1984. "Influence of Reynolds number on characteristics of turbulent wall boundary layers." *Experiments in Fluids*, vol. 2, pp. 7-16.
- Bandyopadhyay, P. R. and R. D. Watson, 1988. "Structure of rough-wall turbulent boundary layers." *Physics of Fluids*, vol. 31, no. 7, pp. 1877-1883.
- Benedict, L. H. and R. D. Gould, 1996. "Towards better uncertainty estimates for turbulence statistics." *Experiments in Fluids*, vol. 22, pp. 129-136.
- Bradshaw, P., 1987. "Turbulent Secondary Flows." *Annual Review of Fluid Mech.* Vol. 19, pp. 53-74.
- Bragg, G. M., 1969. "The turbulent boundary layer in a corner." *J. Fluid Mech.*, vol. 36, pp. 485-503.
- Bruun, H. H., 1995. Hot-Wire Anemometry, Principles and Signal Analysis. Oxford Science Publications, NY.

- Ching, C. Y., L. Djenidi, R. A. Antonia, 1995. "Low Reynolds number effects on the inner region of a turbulent boundary layer." *Experiments in Fluids*, vol. 19, no. 1, May, pp. 61-68.
- Clauser, F. H. "The Turbulent Boundary Layer." *Adv. Appl. Mech.*, vol. 4, pp. 1-51.
- Coleman, H. W. and W. G. Steele, Jr., 1989. Experimentation and Uncertainty Analysis for Engineers. John Wiley & Sons, NY.
- Devenport, W. J. and R. L. Simpson, 1992. "Flow past a wing-body junction – experimental evaluation of turbulence models." *AIAA*, vol. 30, no. 4, pp. 873-881.
- Doligalski, T. L. C. R. Smith and J. D. A. Walker, 1994. "Vortex interactions with walls." *Annual Review of Fluid Mech.*, vol. 26, pp. 573-616.
- Drain, L. E., 1988. The Laser Doppler Technique. John Wiley & Sons, NY.
- Durst, F., A. Melling and J. H. Whitelaw, 1981. Principles and Practice of Laser-Doppler Anemometry, 2nd edition. Academic Press, NY.
- Edwards, R. V., 1987. "Report of the special panel on statistical particle bias problems in laser anemometry." *J. Fluid Mech.*, vol. 109, pp. 89-93.
- Erm, L. P. and P. N. Joubert, 1991. "Low-Reynolds-number turbulent boundary layers." *J. Fluid Mech.*, vol. 230, pp. 1-44.

- Fleming, J. L., R. L. Simpson, J. E. Cowling and W. J. Devenport (1993), "An experimental study of a turbulent wing-body junction and wake flow," *Experiments in Fluids*, vol. 14, pp. 366-378.
- Fujita, H., H. Yokosawa, and M. Hirota, 1989. "Secondary Flow of the Second Kind in Rectangular Ducts with One Rough Wall." *Experimental Thermal and Fluid Science*, vol. 2, pp. 72-80.
- Gessner, F. B. and J. B. Jones, 1961. "A Preliminary Study of Turbulence Characteristics of Flow Along a Corner." *J. Basic Eng.*, Dec., pp. 657-662.
- Hecht. Optics, 2nd edition. Addison-Wesley, NY, 1990.
- Hinze, J. O., 1975. Turbulence. McGraw-Hill Book Company, Inc. NY.
- Humphrey, J. A. C. and J. H. Whitelaw, 1979. "Turbulent Flow in a Duct with Roughness." In Turbulent Shear Flows, J. S. Bradshaw, F. Durst, B. E. Launder, F. W. Schmidt and J. H. Whitelaw, editors. Springer-Verlag, Berlin, vol.2, pp. 174-188.
- Johnston, J. P. and K. A. Flack, 1996. "Review - Advances in Three-Dimensional Turbulent Boundary Layers With Emphasis on the Wall-Layer Regions." *J. Fluids Eng.*, vol. 118, pp. 219-232.
- Karlsson, R. I. and T. G. Johansson, 1988. "LDV measurements of higher order moments of velocity fluctuations in a turbulent boundary layer." Laser Anemometry in

Fluid Mechanics, Ladoan_Instituto Superior Tecnico, 1096 Lisbon Codex,
Portugal, pp. 273-289.

Kreyszig, Erwin, 1983. *Advanced Engineering Mathematics*, 5th edition. John Wiley &
Sons. NY.

Krogstad, P. A., R. A. Antonia, and L. W. B. Browne, 1992. "Comparison between
rough- and smooth-wall turbulent boundary layers." *J. Fluid Mech.*, vol. 245, pp.
599-617.

Krogstad, P. A. and R. A. Antonia, 1999. "Surface roughness effects in turbulent
boundary layers." *Experiments in Fluids*, vol. 27, pp. 450-460.

Kubendran, L. R. Study of Turbulent Flow in a Wing-Fuselage Type Junction. Ph D.
Thesis, Georgia Institute of Technology, Atlanta, 1983.

McLaughlin, D. K. and W. G. Tiedermann, Jr., 1973. "Biasing correction for individual
realization of laser anemometer measurements in turbulent flow." *Physics of
Fluids*, vol. 16, no. 12, pp. 2082-2088.

McMahon, H. J. Hubbartt, and L. Kubendran, 1982. "Mean Velocities and Reynolds
Stresses Upstream of a Simulated Wing Fuselage Juncture," NASA CR 3695,
June.

- Menon, R. and W. T. Lai, 1991. "Key considerations in the selection of seed particles for LDV measurements." ASME Laser Anemometry, A. Dybbs and B. Ghorashi editors, vol. 1, pp. 719-730.
- Milonni, P. W. and J. H. Eberly, 1988. LASERS. John Wiley & Sons, NY.
- Mochizuki, F. T. and Nieuwstadt, 1996. "Reynolds number dependence of the maximum in the streamwise velocity fluctuations in wall turbulence." Experiments in Fluids, vol. 21, pp. 218-226.
- Mojola, O. O., 1978. "The Viscous Sublayer in a Streamwise Corner." J. Appl. Mech., vol. 45, pp. 219-221.
- Nikuradse, J., 1930. "Untersuchungen Uber Turbulente Stromung in Nicht kreisformigen Rohren." Ing. Arch., vol. 1, pp. 306-332.
- Nikuradse, J., 1933. VDI-Forschungsheft No. 361.
- Olcmen, S. M. and R. L. Simpson, 1994. "Influence of wing shapes on surface pressure fluctuations at wing-body junctions." AIAA, vol. 32, no. 1, pp. 6-15.
- Perkins, H. J., 1970. "The formation of streamwise vorticity in turbulent flow." J. Fluid Mech., vol. 44, pp. 721-740. Petrie, H. L., A. A. Fontaine, S. T. Sommer, and T. A. Brungart, 1990. "Large flat plate turbulent boundary layer evaluation." Technical Memorandum No. 89-207, 18 May 1990. Applied Research Laboratory, Penn State University.

Philips, D. B., J. M. Cimbala, and A. L. Treaster, 1992. "Suppression of the Wing-Body Junction Vortex by Body Surface Suction." *J. Aircraft*, vol. 29, no. 1, pp. 118-122.

Pierce, F. J., 1968. "Three-dimensional turbulent boundary layers," from Proceedings Fluidics and Internal Flows, Part II. J. Brighton and A. Healey, editors. Penn State University.

Prandtl, L., 1927. Ergebniss der Aerodynamischen Versuchsanstalt zu Gottingen, Oldenburg, Munchen-Berlin, vol. 3.

Raupach, M. R., 1981. "Conditional statistics of Reynolds stress in rough-wall and smooth-wall turbulent boundary layers." *J. Fluid Mech.*, vol. 108, pp. 363-382.

Raupach, M. R., R. A. Antonia, and S. Rajagopalan, 1991. Rough-wall turbulent boundary layers." *Appl. Mech. Review*, vol. 44, no. 1, pp. 1-25.

Schlichting, H., 1987. Boundary - Layer Theory. 7th edition, McGraw-Hill, NY.

Schultz, M. P. and G. W. Swain, 1999. "The effect of biofilms on turbulent boundary layers." *J. Fluids Eng.*, vol. 121, pp. 44-51.

Shabaka, I., 1979. Turbulent Flow in an Idealized Wing-Body Junction. Ph.D. Thesis, Department of Aeronautics, University of London, London, UK.

Spalart, Philippe R., 1988. "Direct simulation of a turbulent boundary layer up to $Re = 1410$." *Journal of Fluid Mechanics*, vol. 187, pp. 61-98.

- Spalding, D. B., 1961. "A single formula for the law of the wall." *Journal Applied Mechanics*, vol. 28, pp. 455-458.
- Taylor, R. P., H. W. Coleman and B. K. Hodge, 1985. "Prediction of turbulent rough-wall skin friction using a discrete element approach." *J. Fluids Eng.*, vol. 107, pp. 251-257.
- Taylor, R. P., W. F. Scaggs and H. W. Coleman, 1988. "Measurement and prediction of the effects of nonuniform surface roughness on turbulent flow friction coefficients." *J. Fluids Eng.*, vol. 110, pp. 380-384.
- Waigh, D. R. and R. J. Kind, 1998. "Improved aerodynamic characterization of regular three-dimensional roughness." *AIAA*, vol. 36, no. 6, pp. 1117-1119.
- White, F. M., 1974. Viscous Fluid Flow. McGraw-Hill Book Company, Inc., NY.